

# **Interfacial Mechanics and Liquid Crystal Structure of Liquid Gallium**

Von dem Stuttgarter Zentrum für Simulationswissenschaften  
(SC SimTech) der Universität Stuttgart zur Erlangung der  
Würde eines Doktor-Ingenieurs (Dr.-Ing.) genehmigte  
Abhandlung

Vorgelegt von  
**Muhammad Yunusa**  
aus Yobe, Nigeria

Hauptberichter: Prof. Dr. Metin Sitti

Mitberichter: Prof. Dr.-Ing. Holger Steeb

Mitberichter: Prof. Dr. Antal Jákli

Tag der mündlichen Prüfung: 06. Oktober 2021

Max-Planck-Institut für Intelligente Systeme

2021



*Dedicated to my beloved parents*



## Acknowledgements

I am thankful to Professor Metin Sitti for giving the opportunity to work in the Physical Intelligence Department at the Max Planck Institute for Intelligent Systems. Being my PhD supervisor, he gave me space to grow as a scientist amongst the exemplary colleagues in the department. I appreciate the freedom I had during these amazing years of my studies. Additionally, I am indebted to Professor Antal Jakli for the guidance he gave me through my last year of PhD study. I would like to thank Professor Holger Steeb for serving as a co-examiner of my thesis.

This work would not have been possible without the support of many people. I am very thankful to the past and present members of the Physical Intelligence Department for all their fruitful academic discussion and personal advices. I would like to thank Guo Zhan Lum, Ceren Garip Yasa, Hakan Ceylan, Nihal Ölcay Doğan, Oncay Yasa, Sukho Song, Ajay Vikram Singh, Abdon Pena-Francesch, Matthew Woodward, Kirstin Petersen, Chantal Goethler, Massimo Mastrangeli, Metin Muradoğlu, Umut Sanli, Senol Mutlu, Vimal Kishore, Byung-wook Park, Alp Karacakol, Xiaoguang Dong, Mukrime Birgul Akolpoglu, Devin Sheehan, Hyung Gyu Kim, Martin Phelan, Utku Culha, Sinan Demir, Gaurav Gardi, Xinghao Hu, Yunwoo Lee, Cem Balda Dayan, and Ziyu Ren, for the great discussions. Special thanks to Donghoon Son, Berk Yiğit, Madu Batuwangala, Ville Liimatainen, and Varun Sridhar for always being around and supportive. They were always around to listen to all my happy and sad moments. Many thanks to Nagaraj Krishna-Subbaiah, Maritta Dudek, Anitha Shiva, Jack Saud, Gerd Hoerner, Gerd Maier, Hilda David, and Peter Schützendübe for the technical support. I appreciate many hours of the insightful discussions with Gunther Richter.

I would like to thank my research collaborators: Guillermo Amador, Dirk-M Drotlef, Aliénor Lahlou, Morteza Amjadi, Uğur Bözüyük, Yunus Alapan, Amirreza Aghakhani, Hamed Shahsavan, Yubing Guo, and Wendong Wang for their help and great scientific discussions.

I would sincerely like to thank Patricia Martinez, Janina Sieber, Ildikó Papp-Wiedmann, and Eugenia Komnik for their tireless administrative support.

My foremost and deepest gratitude is to my family, especially my parents for their love, support, and constant encouragements during tough and cheerful times. They lift my spirit up and always believe in me undoubtedly. My father, who never see the day to witness the end of my PhD

endeavor, always gave me strength and courage to strive when nothing seems to work. May his soul rest in perfect peace.

Finally, I acknowledge funding supports from Max Planck Society.

Stuttgart, October 2021

Muhammad Yunusa

## **Abstract**

Gallium is a strange metallic material with many features that can benefit our society. Its crystal melts at a few degrees above room temperature ( $\sim 30^\circ\text{C}$ ). Gallium can readily alloy with other metals such as indium and tin to form a stable room temperature liquid metal. The common gallium based liquid metals are eutectic gallium-indium (EGaIn) and gallium-indium-tin (GaInSn) alloys with melting point of 15 and  $-19^\circ\text{C}$ , respectively. Recently, research activities in the utilization of gallium-based liquid metal for flexible soft electronics such as soft robots and sensors have gained many attentions. However, understanding of the liquid state of gallium and its alloy is lacking. For instance, the structure property of liquid gallium is one of the most fundamental aspects that evaded scientists for decades. Elemental gallium is also capable of remaining in liquid state at room temperature due to its supercooling effect. Supercooling is the process of cooling a liquid below its freezing point without becoming a solid or crystal. Moreover, at ambient conditions, liquid gallium forms a nanometer-thick oxide skin that provides mechanical stability to the core liquid.

This dissertation aims to shed light on the fundamental aspects of supercooled liquid gallium. First, the mechanical properties of the oxide skin encapsulating the supercooled liquid gallium droplet is investigated. By leveraging the supercooling behavior of gallium and the formation of its oxide skin, we characterized the emergence of wrinkling at the interface and adhesion energy between the liquid gallium and rigid substrate. An interfacial energy of  $0.238 \pm 0.008 \text{ J m}^{-2}$  was measured between gallium droplet and flat glass.

Secondly, seed induced crystallization of supercooled liquid gallium on the different substrate materials revealed the dependence of the kinetics of crystallization on thermal behavior of the substrate. Such approach further elucidates on the importance of interface temperature during crystallization with a preferred orientation. This result is especially crucial in casting technology for high quality crystal formation on flat surfaces. The characteristic interface adhesion is significant in choosing the right materials for liquid metal manipulation. The design principle

used in ensuring control on the phase transition demonstrate a large switching force between the liquid and crystalline state. Through thermal analysis, we have determined glass transition in elemental metallic gallium.

The third part of the dissertation reports an unprecedented liquid crystal structure in supercooled liquid gallium. By the use of techniques applied in liquid crystal (LC) research, observation of LC texture in supercooled liquid gallium was realized. Reflective polarized optical microscopy (R-POM) on liquid gallium sandwiched between glasses treated with rubbed polymers reveals the onset of an anisotropic reflection of possible dimer molecules or clusters at 120°C that increases on cooling and persists down to room temperature or below. On the other hand, when gallium is sandwiched between substrates that align conventional liquid crystal molecules normal to the surface, the reflection is isotropic. The R-POM and scanning electron microscope textures reveal the existence of a lamellar structure corresponding to smectic liquid crystal phase. The LC phase is very stable even below room temperature. Thermal and electrical response justify the switching behavior of liquid gallium. This observation of LC structure of a highly electrically conductive supercooled liquid gallium provides an unexpected new field of materials science and liquid crystal research.

## **Zusammenfassung**

Gallium ist ein eigentümliches metallisches Material mit vielen Eigenschaften, die sich für die Menschheit als nutzbringend erweisen könnten. Sein Kristall schmilzt bei wenigen Grad über Raumtemperatur ( $\sim 30^\circ\text{C}$ ). Gallium lässt sich leicht mit anderen Metallen wie Indium und Zinn legieren, um bei Raumtemperatur ein stabiles Flüssigmetall zu bilden. Die gebräuchlichsten Flüssigmetalle auf Galliumbasis sind eine eutektische Gallium-Indium- (EGaIn) und eine Gallium-Indium-Zinn- (GaInSn) Legierung mit einem Schmelzpunkt von  $15$  bzw.  $-19$   $^\circ\text{C}$ . Forschungsaktivitäten zum Einsatz von Gallium-basiertem Flüssigmetall für flexible Softelektronik wie Soft-Roboter und Sensoren haben unlängst viel Aufmerksamkeit auf sich gezogen. Das gegenwärtige Verständnis des flüssigen Zustands von Gallium und seinen Legierungen ist jedoch noch unvollständig. Zum Beispiel gehören die Struktureigenschaften von flüssigem Gallium zu den grundlegendsten Fragen, mit denen sich Wissenschaftler seit Jahrzehnten beschäftigen. Elementares Gallium ist aufgrund des Unterkühlungseffekts auch bei Raumtemperatur in der Lage, im flüssigen Zustand zu bleiben. Unterkühlung ist der Prozess der Abkühlung einer Flüssigkeit unter ihren Gefrierpunkt, ohne dass sie zu einem Festkörper oder Kristall wird. Darüber hinaus bildet das flüssige Gallium bei Umgebungsbedingungen eine nanometerdicke Oxidhaut, die der Kernflüssigkeit mechanische Stabilität verleiht.

Ziel der vorliegenden Arbeit ist es, die grundlegenden Eigenschaften des unterkühlten flüssigen Galliums zu beleuchten. Zunächst werden die mechanischen Eigenschaften der Oxidhaut untersucht, welche das unterkühlte flüssige Galliumtröpfchen einkapselt. Um die Entstehung von Falten an der Grenzfläche und die Adhäsionsenergie zwischen flüssigem Gallium und starrem Substrat charakterisieren zu können, haben wir uns das Unterkühlungsverhalten von Gallium und die Bildung seiner Oxidhaut zunutze gemacht. So wurde zwischen Galliumtropfen und Flachglas eine Grenzflächenenergie von  $0,238 \pm 0,008 \text{ J m}^{-2}$  gemessen.

Im zweiten Teil zeigte die keiminduzierte Kristallisation von unterkühltem flüssigem Gallium auf den verschiedenen Substratmaterialien die Abhängigkeit der Kristallisationskinetik vom

thermischen Verhalten des Substrats. Ein solcher Ansatz gibt weitere Aufschlüsse über die Bedeutung der Grenzflächentemperatur während der Kristallisation mit bevorzugter Wuchsausrichtung. Dieses Ergebnis ist besonders in der Gießereitechnik für eine qualitativ hochwertige Kristallbildung auf ebenen Oberflächen entscheidend. Die charakteristische Grenzflächenhaftung ist bei der Auswahl der richtigen Materialien für die Flüssigmetallmanipulation von Bedeutung. Das Konstruktionsprinzip, mit dem die Kontrolle über den Phasenübergang sichergestellt wird, zeigt eine große Umwandlungskraft zwischen dem flüssigen und dem kristallinen Zustand. Durch thermische Analyse haben wir den Glasübergang in elementarem metallischem Gallium bestimmt.

Der dritte Teil der Dissertation berichtet über eine noch nie dagewesene Flüssigkristallstruktur in unterkühltem flüssigen Gallium. Durch den Einsatz von Techniken, die in der Flüssigkristallforschung angewendet werden, wurde die Flüssigkristalltextur in unterkühltem flüssigem Gallium beobachtet. Dazu wurde das Material zwischen Glasplättchen eingefügt, welche mit polierten Polymeren behandelt wurden. Unter dem Polarisationsmikroskop im Reflexionsmodus (engl. R-POM) zeigt sich der Beginn einer anisotropen Reflexion möglicher Dimermoleküle bei 120°C, die beim Abkühlen zunimmt und bis zu Raumtemperatur oder darunter bestehen bleibt. Wird Gallium dagegen zwischen Substrate gepresst, die herkömmliche Flüssigkristallmoleküle normal zur Oberfläche ausrichten, ist die Reflexion isotrop. Die Texturen unter dem R-POM- und Rasterelektronenmikroskop zeigen die Existenz einer lamellaren Struktur, die einer smektischen Flüssigkristallphase entspricht. Die Flüssigkristallphase ist auch unterhalb der Raumtemperatur sehr stabil. Das thermische und elektrische Verhalten rechtfertigt das Umwandlungsverhalten von flüssigem Gallium. Diese Beobachtung der Flüssigkristallstruktur eines hoch elektrisch leitfähigen unterkühlten flüssigen Galliums eröffnet ein unerwartetes neues Feld der Material- und Flüssigkristallforschung.

## Content

<b>1 Introduction</b> .....	<b>15</b>
1.1 Surface Tension and Wetting Properties .....	16
1.2 Wrinkling Phenomena .....	19
1.3 Crystallization Kinetics.....	23
1.4 Size-Temperature Effect on Gallium Polymorphism .....	27
1.5 Anomalous Structure Order in Liquid Gallium .....	28
1.6 Liquid-Liquid phase Transition in Gallium .....	29
1.7 Gallium Clusters “Magic Melters” .....	29
1.8 Methodology .....	31
1.8.1 Investigation of the Supercooling Effect.....	31
1.8.2 Fabrication of a PDMS Post .....	32
1.8.3 Attachment of Liquid Gallium Droplet to PDMS Post.....	34
1.8.4 Adhesion Setup .....	34
1.8.5 Microscopy Technique .....	36
1.8.6 Atomic Force Microscope (AFM) .....	38
1.8.7 X-ray Diffraction (XRD) Technique.....	39
1.8.8 Optical Characterization and Device Fabrication.....	40
1.9 Objectives of the Thesis .....	43
1.10 Thesis Contributions .....	43
1.11 Thesis Outline .....	44
1.12 List of Publications.....	47
<b>2 Wrinkling Instability and Adhesion of Liquid Gallium Droplet</b> .....	<b>49</b>
2.1 Introduction .....	50
2.2 Experimental Section .....	52
2.2.1 Adhesion Setup .....	52
2.2.2 Microscopic Characterization .....	52
2.3 Results .....	52
2.3.1 Uniaxial Compression of Gallium.....	52

2.3.2 Droplet Deformation and Residue Analysis .....	59
2.4 Summary .....	64
<b>3 Crystallization Kinetics and Interfacial Properties of Gallium .....</b>	<b>65</b>
3.1 Introduction .....	66
3.2 Experimental Section .....	67
3.2.1 Supercooling Effect and Recalescence Point.....	70
3.2.2 Analysis of Crystal Fraction During Crystallization Process.....	71
3.3 Results and Discussion .....	73
3.3.1 Crystallization Kinetics .....	73
3.3.2 Interfacial Heat Dissipation Mechanism .....	77
3.3.3 Solidification and Interfacial Adhesion of Supercooled Ga Droplet .....	80
3.3.4 Single Crystal Formation and X-ray and Thermal Analysis.....	86
3.4 Summary .....	90
<b>4 Liquid Crystal Structure in Supercooled Liquid Gallium and Eutectic Gallium-Indium.....</b>	<b>91</b>
4.1 Introduction .....	92
4.2 Experimental Section .....	93
4.2.1 Microscope and Light Spectroscopy Technique .....	93
4.2.2 Liquid Crystal (LC) Cell Preparation and Electrical Characterization .....	94
4.3 Results and Discussion .....	95
4.3.1 Thermal Analysis and Hidden Optical Activity in Supercooled Ga .....	95
4.3.2 Polarization Optical Microscopy (POM) Investigation .....	97
4.3.3 Thermotropic Behavior, Order Parameter, and Microstructure .....	101
4.3.4 Electro-Optics .....	107
4.4 Summary .....	111
<b>5 Conclusion and Future Work .....</b>	<b>113</b>
5.1 Conclusion.....	113
5.1.1 Winkling instability and adhesion of the oxide nanofilm skin of liquid metals..	113
5.1.2 Thermal effect and crystallization kinetics of supercooled liquid Ga .....	114
5.1.3 Liquid crystal structure of the supercooled liquid Ga .....	114
5.2 Future Work .....	114
<b>Bibliography .....</b>	<b>116</b>

<b>Appendix A</b>	<b>137</b>
<b>Appendix B</b>	<b>145</b>
<b>Appendix C</b>	<b>149</b>



# 1 Introduction

Following its prediction in 1871 by Dmitri Mendeleev, who named it "eka-aluminium", gallium (Ga) was discovered and extracted in 1875 by Paul Emile Lecoq de Boisbaudran [1,2]. The discovery of gallium ushered the semiconductor industry through the development of gallium arsenide as a direct bandgap semiconductor in the 1960s [3]. The ability of gallium to alloy with other elements such as indium, arsenic, and nitrogen makes it one of the most important materials for semiconductor and optoelectronic devices. This led to an unprecedented paradigm shift in electronic industry that transformed our modern society. Over 100 years after its discovery, the unusual anomalies of gallium are yet to be understood. Recently, intense research activities have been resumed in both fundamental level and application area of gallium metal [4–13].

Despite being one of the most valuable materials in modern semiconductor industry, gallium has a lot to offer our society in terms of its outstanding electrical and thermal conductivity in the liquid state [14–16]. The properties of its liquid state is not well understood. With its intrinsic low melting point ( $\sim 30^\circ\text{C}$ ), gallium can readily alloy with indium and tin to form a eutectic liquid metals at room temperature.

The common room temperature eutectic alloys of gallium are gallium-indium (EGaIn) and gallium-indium-tin (GaInSn), which are both liquid at room temperature with melting point of 15 and  $-19^\circ\text{C}$ , respectively. Typical EGaIn composition is 75.5 wt% Ga and 24.5 wt%, whereas the eutectic composition of GaInSn is 68 wt% Ga, 22 wt% In and 10 wt% Sn [10]. Thus, liquid gallium and its alloys have been the precursors and centerpiece of research activity in flexible and stretchable interconnects for soft robotics [17,18,27–30,19–26], and 3D printing of liquid metal [31,32]. Gallium and its alloys can readily form an oxide crust when exposed to ambient conditions. The oxide skin that forms on gallium-based liquid metals consist  $\text{Ga}_2\text{O}_3$  with a thickness ranging from 1 to 3 nm. The oxide layer provides a mechanical support to the inner liquid metal by preventing the flow of the liquid metal [33–36]. However, the consequences of this oxide skin on these liquid metals in contact with other surfaces is poorly understood.

The ability to phase-change at room temperature [37] and form a supercooled liquid state [38–40] are among the other fundamental properties of elemental gallium. Gallium can be

supercooled to a wide temperature range below its melting point like other technological liquids such as water, Si, Ge, and Bi. The supercooling behavior of gallium ensured a long period of metastability of the liquid state at ambient conditions. Therefore, the phase-change and supercooling of gallium make it a good candidate to serve as a platform to explore some fundamental properties of matter such as phase-change memory state [41], structural order [44–46], and crystallization behavior [47]. By principle, the fundamentals of surface wetting, adhesion, rheology, liquid-liquid transition and crystallization of liquid metals can be studied, owing to their liquid state stability.

## 1.1 Surface Tension and Wetting Properties

Surface interaction between two substances is governed by the surface tension across their interface. Most of the physical and chemical activities occur at the interfaces. Surface tension is defined as force (F) per unit length (x) acting across a surface. It can be expressed as;  $\gamma = dF/dx$ , in energy expression as free energy (W) per unit area (A) of surface,  $\gamma = dW/dA$ . The unit of surface tension  $N/m$  or  $J/m^2$ . For instance, the surface tension of water is  $72 \text{ mN m}^{-1}$ .

There are several methods to measure the surface tension of a liquid. The Wilhelmy plate or pendant drop techniques are the common methods of measuring the surface tension of a liquid. Liquid metals possess one of the highest surface tension in the literature with value as high as  $700 \text{ mN m}^{-1}$  [48,49].

Unlike surface tension, which speaks of liquid-vapor interface, interfacial tension is based on the surface free energy per unit area between two different liquids that are immiscible. In this case, the difference between the liquid-vapor surface tension of two different liquids ( $\gamma_a$  and  $\gamma_b$ ) and the interfacial tension between them ( $\gamma_{ab}$ ) is expressed as work of adhesion;

$$w_{ab} = \gamma_a + \gamma_b - \gamma_{ab} \quad (1.1)$$

where a and b represent the two different liquids. For pure liquids pulled apart, the work of cohesion can be written as;

$$w_{aa} = 2\gamma_a \quad (1.2)$$

If one liquid and other solid surface constitute the interface, then;

$$w_{sl} = \gamma_{lv} + (\gamma_{sv} - \gamma_{sl}) \quad (1.3)$$

According to Young [50], the trigonometric relations between contact angle and the forces acting on a liquid droplet in equilibrium can be expressed as  $\gamma_{sv} - \gamma_{sl} = \gamma_{lv} \cos \theta$ . Substituting Young's equation of wetting in to the work of adhesion expression yields the Young-Dupre' equation:

$$w_{sl} = \gamma_{lv} (1 + \cos \theta) \quad (1.4)$$

taking  $\theta = 0^\circ$ ,  $w_{sl} = 2\gamma_{lv}$ ; for  $90^\circ$ ,  $w_{sl} = \gamma_{lv}$ ; and for  $180^\circ$ ,  $w_{sl} = 0$ . This expression correlates the wetting angle ( $\theta$ ) and the work of adhesion of a liquid on solid surface.

Further, the force of adhesion between a flat substrate, a, and an elastic sphere, b, with radius  $R$  in a medium c was postulated by Johnson, Kendall, and Roberts theory, (Johnson, Kendall, & Roberts, 1971) [51]. The JKR theory is expressed as;

$$F_{ad} = -\frac{3}{2}\pi R w_{abc} \quad (1.5)$$

where  $w_{abc}$  is the work of adhesion between material a and b in a medium c.

In an ideal elastic sphere adhesion based on the JKR mode, the force of adhesion depends on the energy required to separate the interface between two different materials. Understanding the oxide skin effect on gallium and its alloys droplet is rather complex. The droplet naturally encapsulated with the nanofilm of oxide layers can be ruptured through shear yielding. The shear force required to yield the oxide skin is close to the interfacial surface tension estimate when the droplet is squeezed in contact with a rigid substrate. The droplet shows viscous-like behavior with a precondition of yield according to rheological studies [52,53]. Therefore, JKR model fall short in capturing the dynamics of liquid metal droplets. By the assumption of Newtonian behavior of liquid metal droplet, it is possible to model its surface energy with surface characteristic of fluid such as water. Besides, the viscosity of the pure liquid metals is nearly twice that of water [54]. Irrespective of the  $\sim 3$  nm oxide skin, the overall liquid-like property of the droplet is not affected.

Through the shape of droplet formed by a fluid, surface tension can be measured alternatively. By the pendant technique, as aforementioned, a motionless droplet hanging from a

pipette or syringe tip is imaged. In this scenario, there are two acting forces on the droplet: gravity and surface tension force. Balancing these forces will enable to determine the droplet shape as stated by the Young-Laplace equation:

$$\Delta P = \gamma \left( \frac{1}{R_1} + \frac{1}{R_2} \right) \quad (1.6)$$

where  $\Delta P$  is the pressure difference across a liquid sphere which represent the change in pressure between inside and outside of the droplet, and  $R_1$  and  $R_2$  are the two radii of curvature of the interface.

To modify the surface tension of liquid metals, electrochemical and electro-wetting methods has been widely applied to tune the electrical double layer (EDL) across liquid metal [55,56]. The EDL formation is usually achieved in the presence of an electrolyte solution or when a liquid metal droplet is submerged in electrolyte solution. The surface tension between the liquid metal and electrolyte depends on the potential difference across the EDL. The voltage drop across the EDL is described by Lippman's equation:

$$\gamma_{(V)} = \gamma_0 - \frac{1}{2}CV^2 \quad (1.7)$$

where  $\gamma$ ,  $C$ , and  $V$  are surface tension, the capacitance, the potential difference across the electrical double layer; and  $\gamma_0$  is the surface tension at maximum when  $V = 0$ . The EDL is uniformly charged in the absence of externally applied field. However, with the application of field, a potential gradient is generated along the EDL due to a finite conductivity. In the initial condition, where the EDL is uniformly distributed, the change in Laplace pressure  $\Delta P$  can be assumed for a uniform spherical droplet as:  $\Delta P = 2\gamma/R$ . For instance, Khan et al. [57] demonstrated how to reduce the surface tension of liquid metal from  $\sim 500 \text{ mJ/m}^2$  to near zero in sodium hydroxide electrolyte with the application of 1V external potential. The ability to control the surface tension of liquid metal through surface oxidation is a good example on how versatile and important it is to harness the interfacial energy of liquid metal. Moreover, Hu et al. [58] manipulated liquid metal on a graphite surface immersed in an electrolyte to move the liquid uphill by controlling the pH of the environment.

## 1.2 Wrinkling Phenomena

Wrinkling is ubiquitous in nature. Until recently, wrinkling, buckling and mechanical instabilities have been considered a nuisance and their appearance deemed unwanted [59]. The manifestation of wrinkling and buckling effects are very important principle in mechanical deformation of elastic slender materials. Wrinkling can be observed in animal skin surface due the stiff epidermis layer attached to a soft dermis or when elastic material experiences buckling. Naturally, wrinkles appear on surfaces to accommodate stress such as when a sheet of plastic material is under the influence of external force (uniaxial tensile force) [60]. Other examples of wrinkle emergence are shown on thin sheets of plastic floating on water surface [61]. In addition, thin films coating with metal or plasma treatment on soft elastomer can generate wrinkles with a defined wavelength, which can provide insight into the hard to measure mechanical properties of the material [62]. As polymer thin films are increasingly being integral part of electronics as coatings, dielectric membranes [63], tunable grating [64], and smart surfaces [65], access to their elastic moduli is crucial in designing and choosing the right parameter for specific application. Therefore, characterization of periodic wrinkling generated on surfaces offers an alternative approach to measure the elastic properties of such films [66]. Wrinkling occurs over a wider length scale.

In biological systems, the field of wrinkle generated by a cell crawling on soft substrates have been used to quantify the forces generated during movement [67]. Similarly, vesicle, a thin soft bag formed by lipid bilayers with thickness of  $\sim 3$  nm wrinkles [68]. Recently, Oratis et al. [69] show that rupturing and collapsing of viscous bubbles generate wrinkling with features similar to those appear in elastic sheet. The quantification of wrinkling phenomena have been studied by stretching composite materials with different stiffness where the top stiffer layer film adhered to the bottom infinite elastic foundation. A uniaxial force applied to these composite materials generate wrinkling instability with a characteristic wavelength.

The critical wavelength that minimizes the total strain energy is material dependent and can be expressed as:

$$\lambda = 2\pi h \left[ \frac{(1-\nu_s^2)E_f}{3(1-\nu_f^2)E_s} \right]^{1/3} \quad (1.8)$$

where  $h$  is the thickness of the upper film,  $E$  and  $\nu$  are Young's modulus and Poisson's ratio (the subscripts  $f$  and  $s$  denote the film and elastic substrate). When monitored carefully and analyzed, wrinkling provides a powerful tool to characterize the mechanical properties of thin films such as elastic modulus. The wavelength denotes a sinusoidal deformation profile of the film along the direction of applied compressive force that act on the elastic substrate. This kind of deformation mechanism is brought about by the competing energy between bending of the film and stretching of the foundation material (Figure 1.1).

A landmark theory of wrinkling formulated by Cerda and Mahadevan [60], showed a generalized equations of wrinkling instability. They showed the optimal wrinkling wavelength by balancing the bending and stretching energy of a sheet that experiences uniaxial force. They derived a scaling law based on bending stiffness and effective elastic modulus. The scaling law of their finding can be summarized below as:

$$\lambda \sim \left( \frac{B}{K} \right)^{1/4} \quad (1.9)$$

$$A \sim \left( \frac{\Delta}{W} \right)^{1/2} \quad (1.10)$$

where  $B$  is the bending stiffness of a thin sheet,  $K$  is an effective elastic stiffness of foundation, and  $\Delta/W$  denotes the applied compressive strain. These expressions provide a powerful tool of characterizing all wrinkling phenomena. A thin elastic sheet when stretched will buckle/wrinkle due to energy minimization.

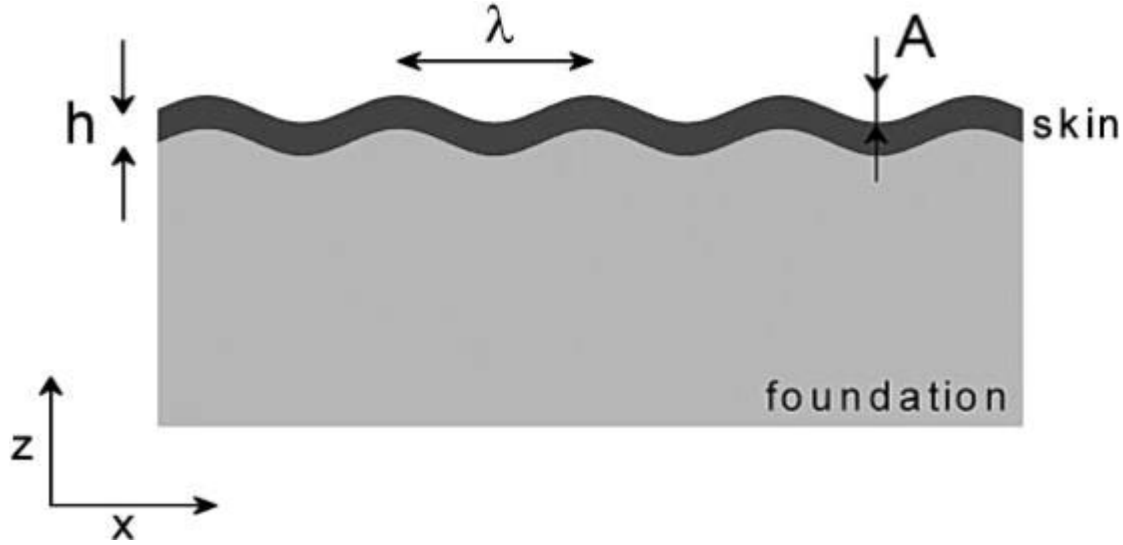


**Figure 1.1:** A schematic illustration of wrinkling geometry. A thin skin (film) with a thickness  $h$  is rested on top of a thick infinite elastic foundation. Wrinkle wavelength and amplitude are represented as  $\lambda$  and  $A$ , respectively. Reproduced from reference [70].

An extension of wrinkling instability has been realized in different conditions. For example, when a thin polymer is stretched at a liquid interface due to surface tension effect, a wrinkling transition can emerge where a compression force is imposed through Laplace pressure [71]. Therefore, understanding how wrinkle evolves is of great importance in drug manufacturing. Thin elastic sheet made of polymer can wrap a droplet optimally as a prime example of control over the mechanical buckling effect of thin sheets where symmetry-breaking phenomena may arise through stress minimization. In the early observation, King et al. [71] illustrated an elegant experiment to characterize the wrinkling instability and the transition regime from wrinkled to crumpled regime in a thin polymer sheets on water droplet under compression. They used a polystyrene sheet of thickness from 49 to 137 nm, carefully delivered on the free surface of water at the top of a tube which formed a spherical cap of radius,  $R = 2\gamma/P$ . Where in this case  $\gamma$  is the liquid-vapor surface tension that stretches the sheet radially at its perimeter.  $P$  is the Laplace pressure that acts normal to the surface of the sheet. In such scenario, the sheet responds to two different forces exerted on the sheet, the stretching and bending with moduli  $Y = Et$  and  $B = \left[ \frac{E}{12(1-\nu^2)} \right] t^3$ , where  $E$  is Young's modulus,  $\nu$  is Poisson's ratio, and  $t$  is thickness. The emerging morphological deformations were expressed through nondimensional parameters defined as

confinement ( $\alpha$ ) and bendability ( $\epsilon^{-1}$ ). In summary, the governing equations of such wrinkling transitions can be expressed as:

$$\alpha \equiv \frac{\gamma W^2}{2\gamma R^2}, \quad (1.11)$$

$$\epsilon^{-1} = \frac{\gamma W^2}{B}. \quad (1.12)$$

where  $W$  is the sheet radius. Because the stretching and compression are more energetically costly, the sheet experiences out-of-plane deformation to relieve stress. For optimal wrapping of liquid with a thin film material, a transition from wrinkling state is ensued by folding to the encapsulated final state. In this problem, the bending energies are negligible because of the dominating surface interfacial energies [72]. When a denser oil is dropped into a water bath where a thin sheet resides at the water-air interface, the surface tension force and the force of gravity compete to determine whether the impacting drop sink or float at the water interface. The critical size of the droplet depend on the capillary length, which is defined as  $l_c = \sqrt{\frac{\gamma}{\Delta\rho g}}$ , where  $\Delta\rho$  is the change in density between oil and water. The droplet size require to sink the droplet is related to capillary length in a given relationship,  $R_0 = \sqrt{\frac{3}{2}} l_c$ .

During liquid metal exposure to ambient condition, oxide skin (thin film) growth is inevitable due to passivation of gallium-oxide layer. The oxide skin on gallium-based liquid metal is analogous to a thin film of synthetic polymer wrapping a liquid droplet. The oxide growth start with a fractal geometry with the abundance of oxygen in the environment. This oxide layer growth reached an equilibrium state attaining a thickness of approximately 3 nm. As previously discussed, the oxide skin provides a mechanical stability and prevent the liquid metal from free flowing. Under certain experimental conditions, an exotic wrinkling transition emerges in the natural liquid metal droplet, which provide a platform to investigate wrinkling effect in inorganic material. With the application of the well-established theory of wrinkling, we characterized the deformation of the oxide skin wrapped around the inner liquid metal. The analogous characteristic wrinkling will be discussed in the next chapter.

### 1.3 Crystallization Kinetics

Crystallization process usually involves first order phase transition from amorphous to crystalline solid phase. Understanding crystallization process is vital in material design and development for many applications areas. For example, tailoring the crystallization kinetics in phase-change material application is a crucial aspect in selecting the right material candidate for the desired application. As information storage becomes an important issue of our digital era due to a sudden boost in the internet-of-things, the current information storage system faces challenge in high speed data processing [73]. According to a projection, the global digital data will continuous to double every year, and anticipated to have reached 44 zettabytes by 2020 (Figure 1.2). For many years, scientist have set out to look for an alternative architecture for memory device with fast speed, high density, and nonvolatile low power consumption memory devices [74]. Phase-change memory has attracted a great deal of attention as a nonvolatile data storage system for the next generation computing.

In phase-change memory application, chalcogenide materials that exhibit amorphous glassy behavior are used in memory cell. To store information, a transition from the amorphous (non-ordered) to ordered (crystalline) phase is triggered by electrical or optical stimulation. The basis for this kind of data storage device lies at the heart of how fast crystallization takes place to SET and RESET a bit of information. In addition, most of the materials used in phase-change application are alloys of binary and ternary compositions [75]. Recently, elemental phase-change material based on antimony has been reported to show phase-change behavior under fast cooling condition [76], which opens a new avenue of monotomic phase-change memory material research. Soares et al. [77] demonstrated an all-optical phase-change memory in a single gallium nanoparticle solely based on polymorphism of gallium. They used pulse laser to deliver energy in form of heat to realize phase transition in the nanoparticle. Through differences in optical properties during phase transition, the polymorphic phases of gallium can be identified at different state. The typical polymorphs of gallium are alpha, beta, gamma, and delta phases. Depending on the heating condition, a metastable phase of gallium can be induced which exhibit a distinguishable optical state.

In designing a memory cell, interfacial property is one of the fundamental criteria to consider. Interface plays an important role in tailoring the bulk property of a material.

Interface determines, and partly affects crystal growth velocity and acts as a site for heterogeneous nucleation.

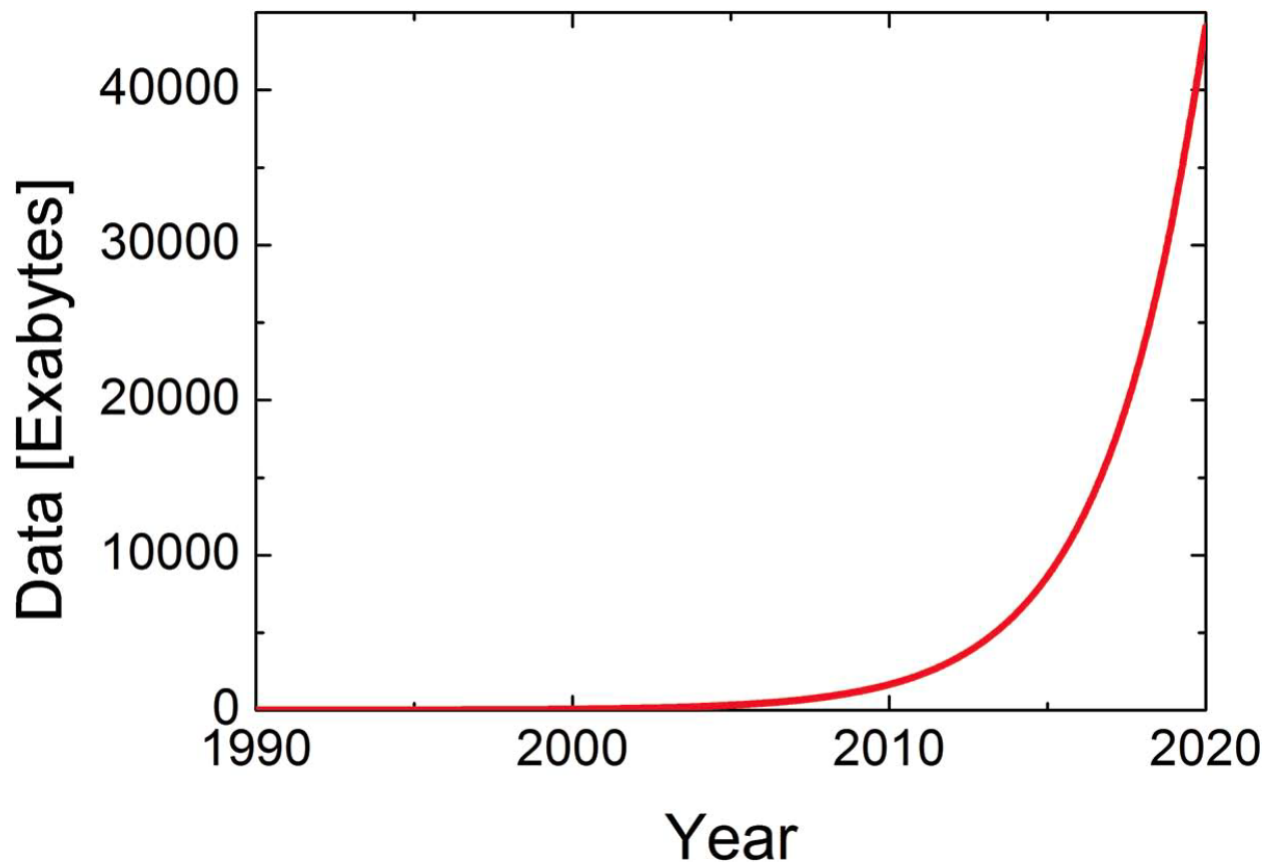


**Figure 1.2:** The growth tendency of digital data created or copied by automated machines and internet of things. Reproduced from reference [74].

In classical nucleation theory (CNT), the kinetics of heterogeneous nucleation is modelled based on energy minimization of a system. To favor crystallization, the free energy change of solid and liquid state is negative ( $\Delta G_{sl} < 0$ ). The CNT is a well-established theory and has been thoroughly investigated by Turnbull [78]. The Gibbs free energy change ( $\Delta G$ ) for the formation of crystallite is the summation of the volumetric and solid-liquid interfacial terms:

$$\Delta G = \Delta G_v + \Delta G_i \quad (1.13)$$

where  $\Delta G_v$  and  $\Delta G_i$  are the volume and interfacial terms, respectively. The expression maybe written as:

$$\Delta G = \frac{4}{3}\pi r^3 \Delta G_v + 4\pi r^2 \gamma \quad (1.14)$$

where  $r$  is the radius,  $\Delta G_v$  is volumetric free energy and  $\gamma$  is the interfacial energy. Due to competition between the volumetric and interfacial term in equation 1.14, for a stable nucleation to form a nuclei critical radius ( $r^*$ ) is required for a maximum  $\Delta G$ . The driven kinetics of attaining a critical nucleus is expressed as:

$$r^* = \frac{2\gamma T_m}{\Delta H \Delta T} \quad (1.15)$$

Therefore, the nucleation barrier for the formation of such critical radius is given as:

$$\Delta G^* = \frac{16\pi\gamma^3}{3\Delta G_v^2} \quad (1.16)$$

Here  $\Delta G^*$  indicates the initiation of solidification process. However, the tendency of metallic liquid to deeply supercooled usually result in high activation energy. The Gibbs free energy between the liquid and solid maybe expressed as:

$$\Delta G_v \approx \frac{\Delta H_m \Delta T}{T_m} \quad (1.17)$$

where  $\Delta H_m$  is the latent heat of melting,  $T_m$  is melting temperature, and  $\Delta T$  is the supercooling degree ( $T_m - T$ ).

In another term, the role of liquid surface in crystallization can be understood through nucleation frequency. The rate of homogeneous nucleation of liquid is defined as:

$$R = A \exp\left(-\frac{\Delta G^*}{K_B T}\right) \quad (1.18)$$

where  $A$  is a pre-factor proportional to free energy of activation ( $G_A$ ) for self-diffusion of atoms across the solid-liquid interface. The expression  $A = \frac{nKT}{h} \exp\left(-\frac{G_A}{KT}\right)$ . Here,  $n$  is the number of atoms per unit volume of liquid,  $k$  is the Boltzmann constant and  $h$  is the Planck constant. At the solidification temperature of most metals,  $\exp\left(-\frac{G_A}{KT}\right)$  is in the order of  $10^{-2}$ . Hence, it is expected to arrive at  $A \approx 10^{33} s^{-1} cm^{-3}$  [79]. In many cases, it is arguable that nucleation takes place homogeneously within because of stable nuclei formation in a melt. Therefore, nucleation mostly occur at a surface, interface, crevices, impurity, or boundaries. In such, the energy required for nucleation is favorably reduced by a factor related to contact angle of the nucleus on the foreign surfaces. Here, free energy expression is written as:

$$\Delta G^*_{het} = \Delta G^*_{homo} f(\theta) \quad (1.19)$$

$$f(\theta) = \frac{(2+\cos\theta)(1-\cos\theta)^2}{4} \quad (1.20)$$

Thus, the rate of heterogeneous nucleation can be written as:

$$R_{het} = A' \exp\left(-\frac{\Delta G^*[f(\theta)]}{K_B T}\right) \quad (1.21)$$

where  $A' \approx 10^{25} s^{-1} cm^{-3}$ . In a deep supercooled liquid metal, heterogeneous nucleation can be powerful tool to harness the crystallization behavior of a melt such as the room temperature low melting point metallic alloys. In principle, heterogeneous nucleation can be controlled by seeding to induce on-demand crystallization in supercooled liquids or facilitate the precipitation of rain droplets. In chapter 3, heterogeneous crystallization approach is used to enable the control of Ga crystal formation from a stable supercooled melt. By tuning the surface and interface in which crystallization occur, one can understand the influence of temperature on the crystallization kinetics. Furthermore, the initial surface temperature could determine the outcome of the crystal

morphology. Several material properties including thermal conductivity, diffusion coefficient, thickness, and density are crucial during crystallization process. For example, thermal gradient across two different materials during crystallization determines how faster heat dissipate at an interface. The solidification of metallic melt with high thermal conductivity is interesting in tailoring microstructure of solids for wide application areas. In crystal growth process, single crystal material can be obtained through seeding from a starting melt of the material. Due to immense boost in solar cell industry, alternative route for high quality crystal fabrication is being sought since materials with different chemistry and form are desirable for different applications.

#### **1.4 Size-Temperature Effect on Gallium Polymorphism**

The unusual melting and freezing of gallium across different size scales have been reported in numerous studies [80–86]. The influence of size-related effect on the crystallization and melting of gallium under confinement has remain a challenge for decades. Under ambient condition, gallium solidifies into different crystal modifications at different temperature regime. The stable room temperature bulk gallium is the alpha ( $\alpha - Ga$ ) phase with melting point of 29.9 °C, whereas several other metastable phases such as beta ( $\beta - Ga$ ), delta ( $\delta - Ga$ ), and gamma ( $\gamma - Ga$ ) polymorphs exist at much lower temperature with melting points -16.2 °C, -19.4 °C, and -35.6 °C, respectively [83]. The high-pressure phases of gallium are more complex where Ga-II exist as body-center cubic (bcc) and Ga-III as body-center tetragonal (bct) [87–89]. Most of the studies conducted on confined gallium droplets were in a polymer matrix, porous glass or at grain boundaries in a confined space. For instance, Di Cicco [82] embedded droplets of gallium in epoxy resin to probe the peculiar phase transition of gallium in a confined geometry. Soares et al. [90] show that gallium grown on the tip of optical fiber exhibit metastable phases even without the confinement effect. Liu et al. [80] attributed the metastability of gallium to surface interaction with carbon nanotubes. Although, myriad of research has been carried out on the physical properties of these polymorphs, there remain some aspects of these phases to be discovered. There is not tangible explanation to what extent confinement and surface effect contribute to the emergence of the different crystal phases in elemental gallium.

## 1.5 Anomalous Structure Order in Liquid Gallium

Like water, upon freezing to solid from the liquid state at ambient conditions, gallium exhibits 3% volume change [89]. Unlike other metals, the stable orthorhombic  $\alpha$ -Ga crystal consist of dimer molecules. In a first-principles theoretical work by Gong et al. [91],  $\alpha$ -Ga was identified as a metallic molecular crystal due to its strong  $\text{Ga}_2$  dimer covalent behavior. Arguably, the description of molecular nature of gallium metal may be related to its low melting point [92]. Upon melting from the solid phase, the dimeric character of gallium may remain in the molten state. Melting is an order-disorder phase transition by which numerous physical properties such as long-range order and shear modulus are altered drastically. Additionally, electronic property of a liquid phase can vary from the solid phase of the same material substantially. For example, semiconductor Si and Ge are metallic in the liquid phase [93,94].

An amorphous liquid phase is disordered system like glass. The like of such systems lack defined direction in terms of long-range order. However, the structure of liquid gallium differs from that of a simple liquid. There are speculation on the existence of dimers in the liquid phase, which are reminiscence of the dimeric bonding of the  $\alpha$ -Ga solid phase. For decades, the structure property of liquid gallium has been debated [44,92]. X-ray and neutron scattering experiments of liquid gallium are employed to characterize the structure order near the melting point and at higher temperatures. The maximum structure factor  $S(k)$  of liquid gallium is asymmetrical which centered around  $2.55 \text{ \AA}^{-1}$  with a shoulder [46,95,96]. Xiong et al. [45] have elaborated on the evolution of such structure in liquid gallium for a wide range of temperature. Drewitt et al. [4] have recently reported on the structure of liquid gallium under extreme pressure and temperature condition. In their results, even though the liquid resembles a hard-sphere structure close to the melting curve, they found increasing fractions of five-fold symmetric and crystalline motifs at high pressure and temperature. Based on the neutron and X-ray scattering data, Mokshin et al. [44] disclosed that no stable crystalline domains or molecular  $\text{Ga}_2$  dimers in equilibrium liquid phase. According to a theoretical study, the structure of liquid gallium has been attributed to the high-pressure gallium phases Ga-II and Ga-III [97] or  $\beta$ -Ga [95] instead of the dimer. Despite the extensive studies on the structural features of liquid gallium, discussion on the origin of such fascinating behavior has remained inconclusive and a consensus is still lacking.

## 1.6 Liquid-Liquid phase Transition in Gallium

Under strong supercooling of glassy liquid, liquid-liquid phase transition (LLPT) were observed in both molecular liquids and metallic melts [98,99]. LLPT is a liquid polymorphism attributed to structural transformation. This structural anomaly is temperature dependent and can affect thermophysical parameters of liquid such as viscosity. The viscosity ( $\eta$ ) of molten slag is temperature sensitive above the melting point as described by Frenkel's equation [100]:

$$\eta = A \exp\left(\frac{E}{K_B T}\right) \quad (1.22)$$

where  $A$  and  $E$  are temperature independent, and  $K_B$  is Boltzmann's constant.

In experimental studies, LLPT is shown to occur in elemental liquids such as phosphorous [101], and silicon [98]. In a recent study, LLPT has been observed in Sulphur [102] and gallium alloys under nanoconfinement [103]. Generally, LLPT is a hidden phenomenon overshadowed by fast crystallization process in materials. Theory and simulation studies show that elemental gallium exhibit LLPT [98,104,105]. In a study by Li et al. [85], they claimed that size-temperature driven polymorphism in gallium is accompanied by LLPT where metastable gallium phases could coexist with a liquid at a certain length scale after transition from one phase to another.

## 1.7 Gallium Clusters “Magic Melters”

It is a fundamental question to understand how the atomic and electronic properties change with size of matter [106]. Clusters are formed because of aggregation starting from a single atom to tens and hundreds of atoms and to bulk material. Thermodynamic property such as melting point of a small cluster differs from that of the bulk parent material [107]. The reduction of melting point as size decreases is known as ‘melting point depression’. Metals with low melting points like indium [108], gold [109], tin [110], and lead [111] are used for the investigation of the melting point depression. In a pioneering work, Schmidt et al. [112,113] have measured the melting point and heat capacity of 139 sodium atoms in a cluster where the cluster acted as its own nanocalorimetry.

Lai et al. [110] experimented with small tin particle by nanocalorimetric measurements using ultrafast calorimetric method. In light of recent studies, melting point depression is partly applicable for mesoscopic clusters containing thousands of particles [114]. For much smaller clusters with a few atoms, the melting point depression effect does not hold. Through ion mobility measurement, Shvartsburg et al. [114,115] examined the room temperature structure of tin cluster cations consisting of 68 atoms. They experimentally proved that clusters with  $15 < n < 35$  adopt prolate geometries (i.e., pointy ellipsoid similar to a rugby ball shape) with aspect ratio up to 3.

Following the work of Li et al. [106] on the dynamics of atomic clusters and the simulation on cluster formation, there was great interest in the structural dynamic of cluster formation. Molecular dynamic simulations on atomic clusters of  $\text{Ga}_{30}$  and  $\text{Ga}_{31}$  revealed a dramatic size sensitivity of heat capacity measurement [116]. This type of cluster of  $\text{Ga}_{31}$  ion with a well-defined heat capacity is called a “magic melter”. In an experimental study conducted by Gary et al. [117], they measured the internal energy of the cluster ions of  $\text{Ga}_{17}^+$ ,  $\text{Ga}_{39}^+$ , and  $\text{Ga}_{40}^+$ . The temperature dependency of specific heat capacity of gallium persist across wide range of clusters of 30-55 atoms [118]. The strong size dependent higher than bulk (29.8 °C) melting temperature of gallium cluster ion is well studied. At this length scale, the addition of one atom to a cluster can have a tremendous effect on the specific heat capacity of the cluster. In doing so, a subtle change in specific heat capacity can be detected based on the number of atoms in a cluster. For instance, nonmelter cluster ion is usually without a heat capacity peak or a broad peak, whereas the magic melter exhibit an identifiable peak of specific heat capacity.

## 1.8 Methodology

In this section, most of the important techniques and sample preparation procedures covered in this dissertation are discussed. Microstructure characterization techniques employed are explained in detail.

### 1.8.1 Investigation of the Supercooling Effect

To investigate the supercooling effect of gallium, we used differential scanning calorimetry (DSC). The principle of DSC is based on the energy changes that occur when material is heated. Any heat change in a material such as enthalpy of fusion and crystallization can be register as the material is heated, cooled, or held isothermally at a constant temperature. The temperature at which events occur is very important in understanding thermal behavior of the material. This method provides both quantitative and qualitative information about the physical and chemical changes pertaining energy changes in materials. DSC is one amongst other techniques used to study thermally dependent property of materials such as melting, crystallization, boiling, oxidation, reaction kinetics, glass transition and enthalpy recovery. The use of this technique spans from material understanding to pharmaceutical studies. The advantage of this technique is that the sample are easily prepared and encapsulated.

Ga samples of 5 - 7 mg were subjected to heating and cooling at  $5\text{ }^{\circ}\text{C min}^{-1}$  to detect the endothermic and exothermic peak for all phase transition. On heating to  $150\text{ }^{\circ}\text{C}$ , the sample melts at around  $30\text{ }^{\circ}\text{C}$ , which is the regular melting point of Ga. On the contrary, during cooling circle the liquid Ga does not crystallized at  $30\text{ }^{\circ}\text{C}$  due to the induced supercooling effect (Figure 1.3). The supercooling effect is induced by overheating the material beyond its melting point. Supercooling effect is a thermal related to the internal energy of a system. It is an intrinsic property of certain materials to exhibit supercooled state because of metastability. Typical example of such materials is liquid water. In Figure 1.3, the green line indicates the heating cycle, while the red line indicates cooling cycle, respectively.

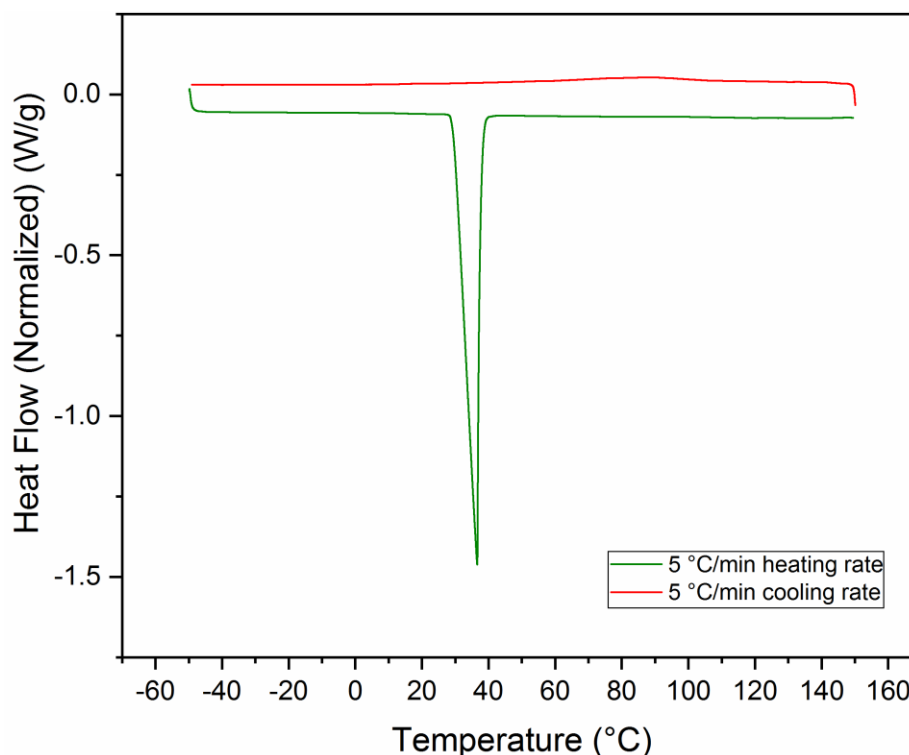


**Figure 1.3:** DSC curve of heating and cooling cycle demonstrating the supercooling behavior Ga

### 1.8.2 Fabrication of a PDMS Post

To prepare a platform in which we will carry out the experiment, a negative mold made up of PDMS was obtained by replicating a 3D-printed cylindrical post that was designed in a computer-aided design (CAD) software (SolidWorks). Before the molding process, a plastic version of the post, composed of VeroClear material was fabricated using 3D printer (Objet260 Connex, Stratasys Ltd.). The post has a diameter of 1.75 mm with a height of 5.25 mm, and base support of 5 mm diameter with 2.8 mm thickness (Figure 1.4, step 1). The printed post was thoroughly cleaned in 1 mol NaOH solution to remove the supporting materials. The post was then fixed upright in a small plastic petri dish using double-sided tape. A prepolymer (Sylgard 184, Dow Corning) siloxane base and curing agent were mixed in a 10:1 ratio, degassed, and casted into the Petri dish, which was then cured in a vacuum oven at 90 °C for 1 hour and carefully demolded. The fabricated negative mold of the soft cavity was treated in an oxygen plasma at 100 W for 3 minutes, then followed by surface modification using Trichloro(1*H*,1*H*,2*H*,2*H*-perfluorooctyl) silane (Sigma-Aldrich Chemie GMBH) for 1 hour in vacuum and cured at 90 °C for 30 minutes.

The perfluorosilane modification of the mold was very significant in preventing the adhesion of the casted materials in the following replication steps. To fabricate the sample, again, the siloxane base and curing agent were mixed in a 10:1 ratio, degassed, and casted on the PDMS mold of the cylindrical post cavity. The sample was cured in a vacuum oven at 90 °C for 1 hour and then demolded (Figure 1.4, steps 9 and 10). The post was attached to a threaded metallic holder to facilitate attachment onto a force sensor for adhesion measurement. A silicone adhesive (Sil-Poxy, Smooth-On Inc.) was applied between the metal and the base part of the PDMS post. After curing at room temperature for 30 min, strongly bonded component of the post and the metal holder was prepared.

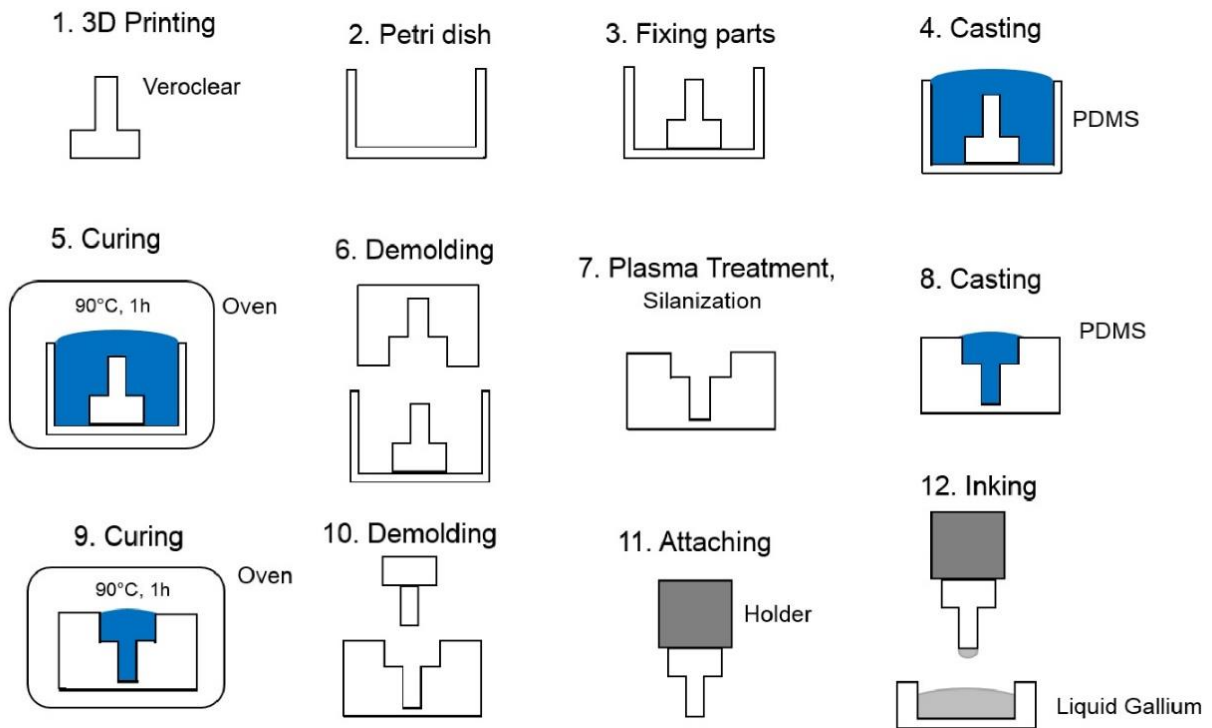


**Figure 1.4:** Fabrication procedure of a PDMS post with a Ga droplet. Individual steps of printing and molding are shown schematically. Ga was kept in liquid state by heating it above its melting point, up to 35 °C, in order to induce supercooling effect [119]. After heating the metal to this temperature, solidification process of liquid-Ga was inhibited; then, we dipped the post in the melt to decorate the PDMS tip with a Ga droplet. The experiments were carried out in ambient temperature. Ideally, heating Ga to about few degrees (1 to 2 °C) above its melting temperature does not impede its solidification at room temperature when cooled down.

### 1.8.3 Attachment of Liquid Gallium Droplet to PDMS Post

A pool of liquid-Ga was prepared by heating commercially available pure Ga (99.99%, ACROS Organics™) up to 10 °C above its melting temperature (29.7 °C). After heating to this temperature, the supercooling effect is induced, which depends on the degree of overheating [119,120]. The solidification of liquid-Ga is inhibited at room temperature and thus, we carried out the experiment conveniently by leveraging this effect. Ideally, heating liquid-Ga to about few degrees (1 to 2 °C) above its melting temperature does not impede its solidification when cooled down to room temperature. The PDMS post mounted to the force sensor was lowered into the Ga liquid to coat the material. After removing the PDMS from the liquid Ga, a spherical cap droplet was attached to the post due to cohesive bond between liquid Ga and the PDMS as shown in Figure 1.4, step-12.

### 1.8.4 Adhesion Setup

A customized adhesion setup mounted on an inverted optical microscope (Axio Observer A1, Zeiss) with a video camera (Grasshopper3, Point Gray Research Inc.) was used to visualize and record the contact interface (Figure 1.5). The force between the sample and substrate was measured by a high-resolution load cell (GSO-25, Transducer Techniques). The load cell was mounted to a high-precision piezo motion stage (LPS-65 2", Physik Instrumente GmbH & Co. KG) in the vertical  $z$  direction, with a resolution of 5 nm and maximum velocity of  $10 \text{ mm}\cdot\text{s}^{-1}$ . A long-ranged motor stage (M-605 2DD, Physik Instrumente GmbH & Co. KG) was used in  $y$  direction with 1- $\mu\text{m}$  resolution and high maximum velocity up to  $50 \text{ mm}\cdot\text{s}^{-1}$ . The substrate was fixed onto a sample holder within the focal range of the microscope and moved in  $x$  direction by the piezo stage (LPS-65 2", Physik Instrumente GmbH & Co. KG). A secondary video camera was used to visualize the side view of the sample during the experiments. The camera was attached to an objective lens (Mitutoyo M Plan Apo 10x Objective) and captured the  $z$  direction motions during preloading from the side. A computer controls all motion stages. Both environmental temperature and humidity were monitored using a commercially purchased sensor (Humidity/Temperature/Dew Point Meter, Fisher Scientific).

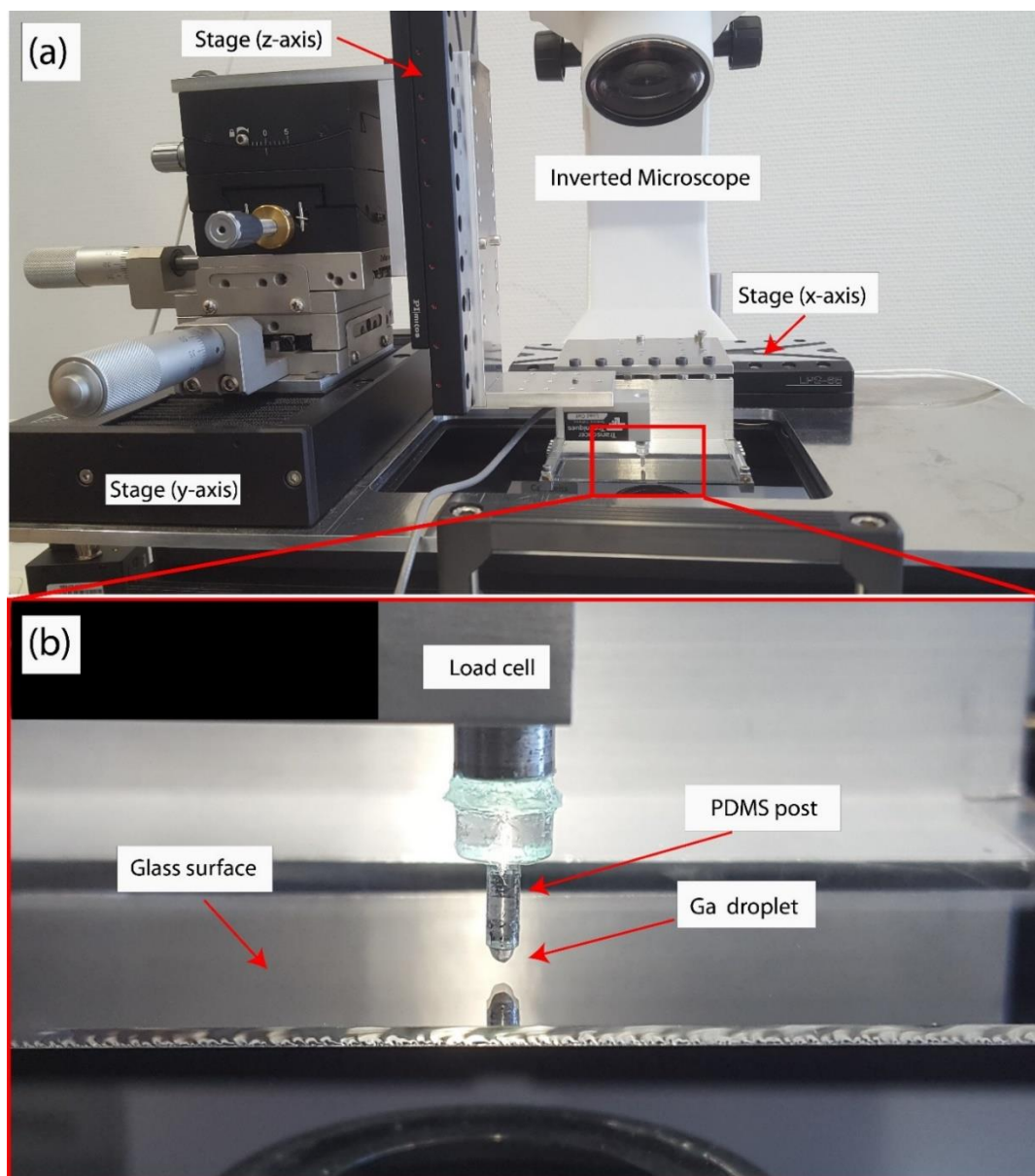


**Figure 1.5:** (a) Photograph of the custom experimental setup for characterization of the Ga droplet adhesion on a glass substrate. (b) The magnified side-view image of the Ga droplet attached to the PDMS pillar mounted on the load cell, and the glass surface on which the liquid Ga is pressed.

### 1.8.5 Microscopy Technique

A scanning electron microscopy (SEM) technique was used to characterize the surface structure and morphology of gallium material. In addition, the elemental composition of gallium was analyzed with this technique. An accelerated electrons beam bombarded the surface of the material, thereby creating secondary photons with a characteristics energy level. By scanning the illuminated sample surface under high vacuum, a detector can collect the scattered secondary electrons emitted by the material to reconstruct the surface morphology. The emitted secondary electrons are characteristics of the material under investigation. The secondary electrons are the result of interaction of the atoms from the sample due to the interaction with incident electron beam. Back scattered electrons due to elastic scattering from the atom of the material enabled elemental analysis by creating a contrast difference.

When secondary electrons are created in the material, an unoccupied state is left behind which can interact with a high energy level electron and result in characteristic X-ray emission that allow the further elemental characterization of the material through energy dispersive X-ray spectroscopy (EDX or EDS).

The surface of gallium is crumpled with uneven geometry when exposed to ambient condition. SEM imaging allow the visualization of the wrinkles that formed on gallium droplet showing the structure of the fresh gallium oxide skin that developed on the droplet. To prepare gallium sample for SEM, thin film samples were slowly cooled and solidified which were then quenched in liquid nitrogen prior to imaging. Afterward the sample was freeze-fractured to investigate the bulk structure property of the films Figure 1.6a depicts a typical gallium sample fractured into small piece and was mounted on a SEM holder with carbon tape as fixation support. During SEM imaging, the samples was held at -20 °C to prevent structural damage. EDX analysis for a Ga film crystallized at ambient condition shows the elemental content of the material (Figure 1.6b).

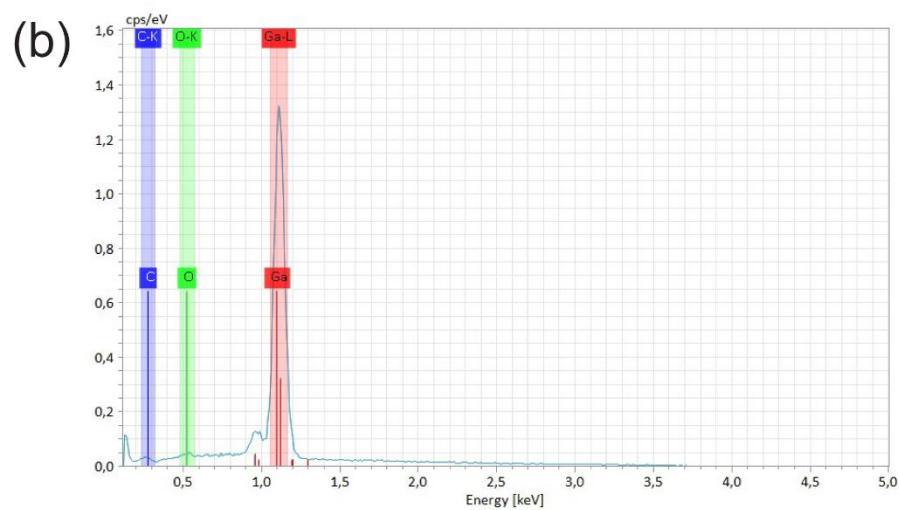
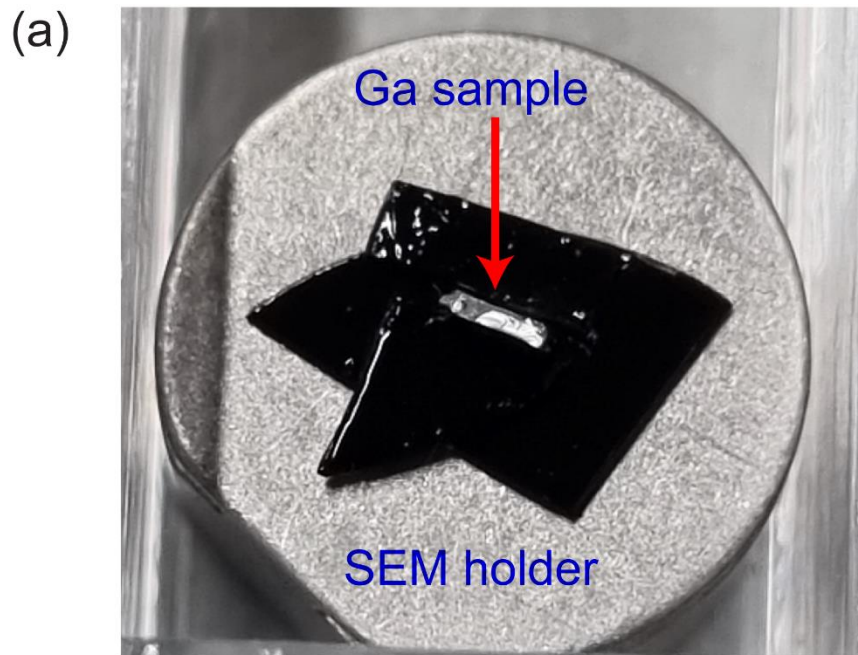


**Figure 1.6:** (a) Representation of SEM sample preparation for microstructure characteristics. The arrow is pointing at a fractured gallium film of 300  $\mu\text{m}$  thickness. The black film is conductive carbon tape suitable for SEM imaging. (b) An EDX analysis of pure Ga solid crystallized in open air.

### 1.8.6 Atomic Force Microscope (AFM)

Atomic force microscopy technique is utilized to for the characterization of surface roughness and morphology of material. AFM imaging technique uses laser beam deflection system with a cantilever. The laser reflection from the back of a reflective cantilever is detected onto a position-sensitive detector by scanning across a surface. The sharp tip of the cantilever is force sensitive and allows mapping material surfaces with micro- or nano-contours. With AFM, very fine roughness scale down to nanometer features are characterized. From the AFM result in Figure 1.7, we measured a surface roughness value of a rigid glass with a root-mean-square value of 1.23 nm.

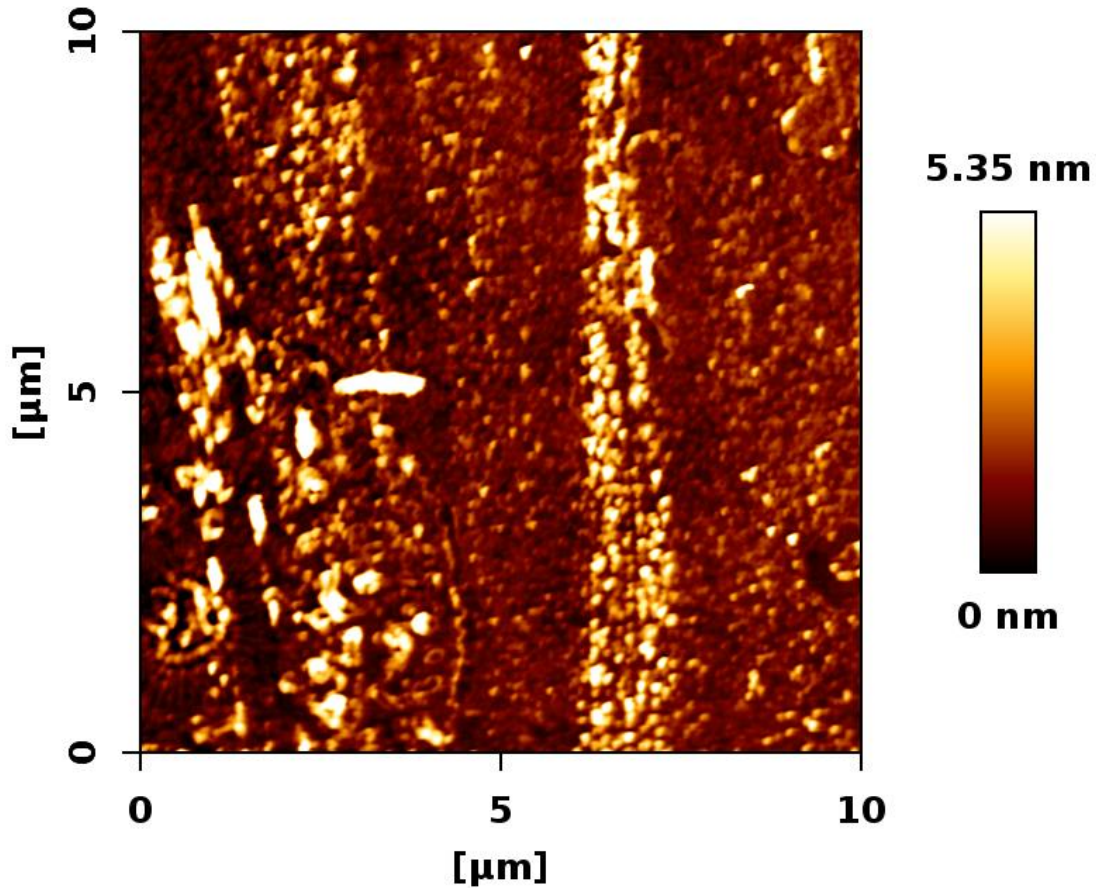


**Figure 1.7:** Atomic force microscope (AFM) surface 3D image of the glass substrate used in experiments. Root-mean-square (RMS) roughness of the glass surface is measured as 1.23 nm. The image was obtained using JPK NanoWizard ULTRA Speed AFM through tapping mode.

### 1.8.7 X-ray Diffraction (XRD) Technique

X-ray diffraction technique is a very powerful tool to investigate the structure of materials. It has been widely utilized in diverse application area including material science, physics, chemistry, and biology. X-ray diffraction technique is widely employ to understand structural property of matter such as crystal (long-range order) and amorphous (disorder). The method is nondestructive for most materials. XRD has major implication in tailoring microstructure for various applications. XRD technique is based on Bragg's diffraction of structure when illuminated with X-ray radiation. The mathematical expression of the Bragg's law of diffraction explains the relationship between the wavelength and angle of diffraction. It is written as:

$$n\lambda = 2d \sin \theta \quad (1.23)$$

where  $\lambda$  is the wavelength of X-ray photon,  $d$  is interlayer spacing between planes, and  $\theta$  is half the diffraction angle. For the XRD of thin film gallium sample, we adopted the conventional powder XRD D8 Advance Bruker X-ray machine using a Cu-K $\alpha$  ( $\lambda = 1.5418 \text{ \AA}$ ) to investigate the crystal structure of large area crystals of gallium obtained from the supercooled state. The crystal was fabricated on the desired substrate material such glass. Prior to the XRD analysis, the sample cooled in liquid nitrogen to prevent melting of gallium due to its low melting point. The tendency to melt the structure in gallium crystal at room temperature is high upon prolong exposure to high-energy radiation. In Figure 1.8, an example of gallium film prepared for the XRD experiment is illustrated. The sample thickness is around 65  $\mu\text{m}$ .

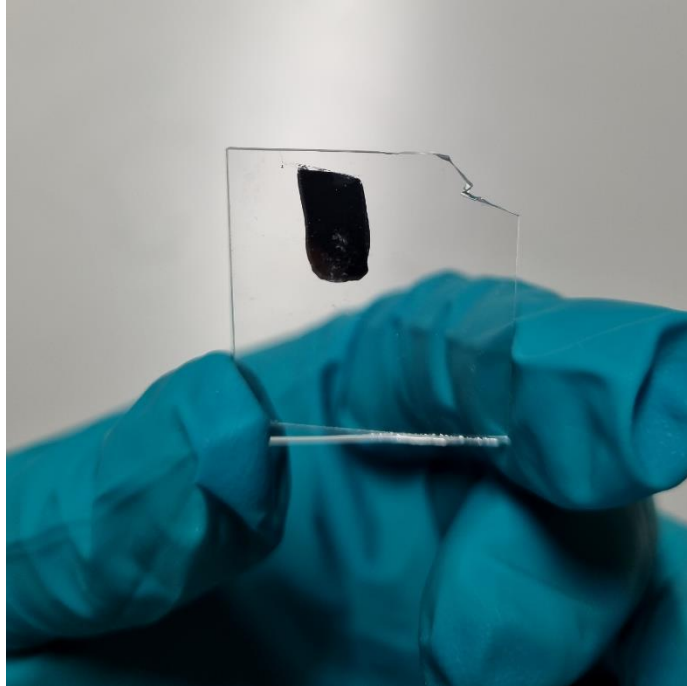


**Figure 1.8:** Sample preparation for X-ray diffraction measurement. The darker (silvery gray) region on the glass plate is a large area crystal of gallium obtained from the supercooled melt.

### 1.8.8 Optical Characterization and Device Fabrication

Optical reflection of measurements are performed in an electro-optic cell. The device was constructed by sandwiching liquid gallium or gallium-indium alloy in between two electrically conducting transparent glass plates. A spacer controlled the thickness of the assembled device. Copper electrodes were connected to the conductive side of both glasses using highly electrical conducting silver paste that is thermally cured for 30 minutes to enable secure electrical connections (Figure 1.9). Note that, liquid metal is sandwiched between the glasses with the conducting sides inward. For further experimental detail on optical sample preparation, the reader should referred to chapter 4. The optical effect upon field application is studied under reflective polarized optical microscopy (R-POM). Because of the opacity of gallium, the optical characterization was limited to reflective light, unlike the usual transparent materials, which transmit incident light. Ga and its EGaIn alloy show relatively very small absorptions at certain electromagnetic wavelength. The UV-Vis-NIR spectra of the two materials, pure Ga and EGaIn (75.5% Ga, 24.5% In) were carried out in thin film sandwiched between transparent glass. The

UV-Vis-NIR spectra exhibit small relative absorption at selective wavelengths in liquid Ga and EGaIn film under investigation (Figure 1.10). The measurement was performed using Perkin Elmer UV-Vis-NIR, lambda 1050+.

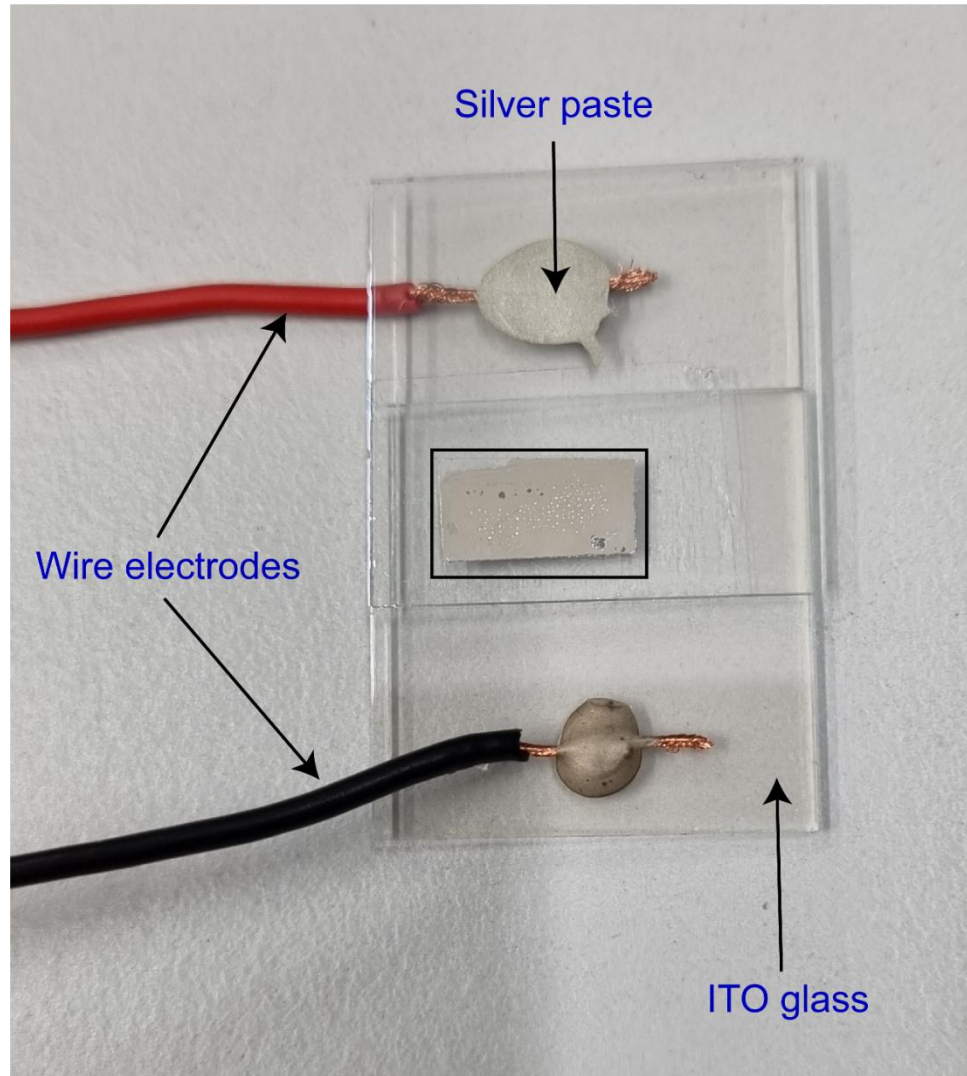


**Figure 1.9:** An illustration of electro-optic device. The device was assembled by sandwiching liquid metal film between two electrically conducting glass plates. The black rectangular box show the liquid Ga film of approximately  $1 \times 0.5 \text{ mm}^2$ .

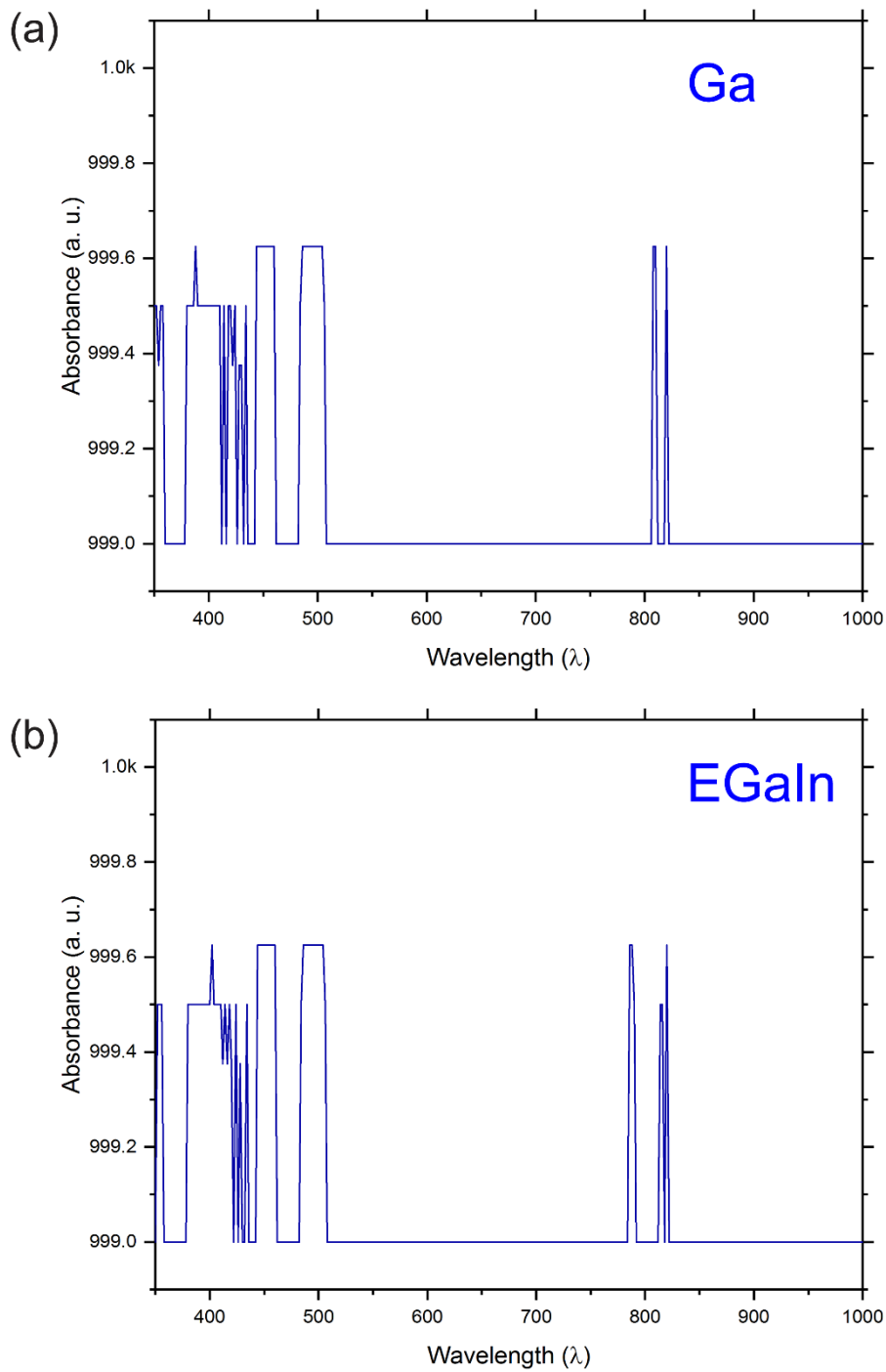


**Figure 1.10:** UV-Vis-NIR spectra of Ga (a) and EGaIn (b). There is similarities in absorption peaks at selective wavelengths in both pure Ga and EGaIn alloy.

## 1.9 Objectives of the Thesis

Due to the ever-growing demand of soft electronic devices for functional material interfacing with machine for sensing and motion detection, liquid metals are extensively studied. However, the understanding of structural and interfacial properties of liquid metals remained inconclusive. In this work, I set to resolve some of the fundamental questions related to the liquid structure of metallic materials. The findings presented in this thesis will change the scope of how liquid metals are utilized in soft-matter conductive material application and will open up a new avenue of material physics research.

Objectives of this thesis are:

- (1) To understand the role of the  $\text{Ga}_2\text{O}_3$  skin encapsulating liquid gallium droplet and its interaction with a rigid substrate
- (2) Explore the fundamentals of crystallization in supercooled liquids, the effect of supporting substrate on the crystallization kinetics, and the realization of glass transition in elemental gallium
- (3) Investigate structural order in gallium by revealing the liquid crystal mesophase in supercooled liquid gallium and gallium-indium, which has evaded scientists for decades.

## 1.10 Thesis Contributions

This thesis focuses on three different fundamental physical attributes of supercooled liquid metal gallium. New strategies have been developed to study the wrinkling behavior of oxide skin encapsulating liquid gallium droplet under mechanical deformation at a rigid interface, thermal effect on the crystallization kinetics on different interface materials, and molecular liquid crystal behavior of the supercooled liquid gallium and gallium-indium alloy. Thus, different fabrication methods and designs are utilized to reveal the fundamental aspects of liquid gallium that remained unknown hitherto. The main contributions are:

1. Characterization of wrinkling emergence and the transition from circular to radial wrinkles.

2. Highly oriented crystal formation on substrates, glass transition of elemental metal, and substrate-dependent adhesion of gallium.
3. Discovery of liquid crystal phase in supercooled liquid gallium and gallium-indium.

## 1.11 Thesis Outline

The thesis consists of three parts. Chapter 2 introduces the wrinkling mechanics and adhesion of supercooled droplet of gallium under mechanical confinement. The role of its oxide skin in contact with rigid substrates such as rigid glass, where wrinkling instability and interfacial adhesion is studied. We thoroughly investigated the evolution of wrinkling dynamics of the oxide crust analogous to a thin sheet of plastic stretched on a fluid surface. The wrinkling phenomena is an example of how natural systems develop folds and creases to relieve stresses and conform from three-dimensional (3D) to two-dimensional (2D) space. The force characterization gives an insight of how much deformation is required to rupture the oxide skin of liquid metal. Newtonian liquid-like property of the liquid droplet is verified through surface energy approximation. Residue deposition the substrate surface is analyzed for a delicate manipulation of the droplets. All this will enable the versatility on how to utilize liquid metal for soft electronic applications.

Chapter 3 summarizes the phase transformation kinetics of bulk gallium from liquid to solid state (crystallization kinetics). The influence of thermo-mechanical stress at the interface of the substrates with different thermal properties are investigated. The goal of this part of the work is to elucidate the intrinsic material properties of elemental gallium and leverage the unusual properties it present to understand the fundamental aspect of crystallization kinetics of liquid metals at ambient condition. The supercooling effect of gallium provides a suitable platform to investigate how metallic liquids crystallized. The unique effect of surface temperature and the thermal conductivity of the substrate are exceptional features allowing the formation of monolithic crystal film of gallium. Single crystal growth are achieved similar to Czochralski crystal growth method on a flat glass slide. This approach provides a new route to suitable production of high quality crystals on different substrates for optoelectronic, solar cell, and flexible electronics. One of the missing link between crystallization and surface property when growing a large area crystal is the influence of the substrate material. To solve this challenge, we have uncovered the

underlying principle governing heat dissipation through substrate. By tuning the surface temperature and the thermal conductivity of the substrate, we controlled the outcome of the crystallization process. Depending on the interface material, we can tailor the microstructure of the crystal formation leading to large area single crystal formation without the need for external forces such as magnetic or electric field during growth process. Moreover, the introduction of seeding crystal enabled on demand crystallization with high fidelity. Different from other supercooled liquids such as water, we now show that crystallization of supercooled liquid metal can be controlled by initiating a nucleation from a specific site. The method can be extended to a large-scale synthesis of high quality crystal from a melt precursor.

In Chapter 4, a discovery of liquid crystal phase in liquid metals is demonstrated. Over decades, scientist have posed the notion of structural order in liquid gallium. In an ideal isotropic liquid, atoms jiggle around randomly without any long-range order. On the contrary, crystalline materials are ordered with regular arrangement of atoms and defined translational symmetry. The atoms in crystals are fixed in position with a special modification. Different atoms form distinct modification of crystal structures. According to classification of matter, a phase that exist between the isotropic liquid and solid state is a mesophase. The mesophases can possess a property of both liquid and solid with a long-range molecular spatial organization and therefore are called liquid crystals (LCs). Unlike the disordered isotropic liquids, LCs possess long-range orientation, and in some cases, positional order. In 1888, Friedrich Reinitzer discovered the cholesteric LC phase in cholesteryl benzoate by observing the foggy blue color upon melting before reaching the isotropic phase [121]. Many scientists and engineers have detected series of optical activities and phase transitions in various LC materials. Currently, there are hundreds of organically synthesized LC molecules with exotic properties including the nematic, cholesteric, and smectic phases. The common nematic phase enabled the modern day LC display technology [122]. The constituent of LC molecules have been the covalently bonded organic molecules. Hitherto, in this thesis, an unprecedented discovery of LC structure in supercooled metallic liquid gallium and its alloy (gallium-Indium) is unveiled at room temperature. By the use of reflective polarized optical microscopy (R-POM) on Ga sandwiched between glass substrates treated with rubbed polymers that usually align the director of thermotropic liquid crystals (LCs) parallel to the rubbing, spectroscopy technique and differential scanning calorimetry, we have identified anisotropic reflection at 120°C that increases on cooling and persists down to room temperature. The optical

phenomenon investigated could be a paradigm shift in understanding the behavior of matter and justifies the long debated structural order mechanism in liquid metals.

Finally, the last chapter summarizes the overall contributions and results of our work and presents a future work for the immense potentials of liquid metals in electronic devices.

## 1.12 List of Publications

The work presented in this thesis is composed of published data in peer reviewed journals. All publication data in Chapter 2, 3, Appendix A, and Appendix B are reproduced with permission of the publishers. Publication data (P-3) in Chapter 4 and Appendix C have been submitted to a peer reviewed journal.

**P-1) Yunusa, M., Amador, G. J., Drotlef, D., Sitti, M. Wrinkling Instability and Adhesion of a Highly Bendable Gallium Oxide Nanofilm Encapsulating a Liquid-Gallium Droplet** *Nano Letters*, 18, 4, 2498–2504, 2018

**P-2) Yunusa, M.,\* Lahlou, A.,\* Sitti, M. Thermal Effects on the Crystallization Kinetics, and Interfacial Adhesion of Single-Crystal Phase-Change Gallium** *Advanced Materials*, 32 10, 1907453, 2020 (\* First co-authors)

**P-3) Yunusa, M., Adaka, A., Aghakhani, A., Shamsavan, H., Guo, Y., Alapan, Y., Jáklí, A., Sitti, M. Liquid Crystal Structure of Supercooled Liquid Gallium and Eutectic Gallium-Indium** *Advanced Materials*, 33, 38, 2104807, 2021 (Inside Back Cover)

During the time of my PhD work, I have contributed to other projects as co-author, which are not the primary topic of this thesis. Therefore, these works are listed as additional co-authored publications:

**A-1) Drotlef, D., Amjadi, M., Yunusa, M., Sitti, M. Bioinspired Composite Microfibers for Skin Adhesion and Signal Amplification of Wearable Sensors** *Advanced Materials*, 29, 28, 1701353, 2017 (Back Cover)

**A-2) Giachini, P., Gupta, S., Wang, W., Wood, D., Yunusa, M., Baharlou, E., Sitti, M., Menges, A. Additive manufacturing of cellulose-based materials with continuous, multidirectional stiffness gradients** *Science Advances*, 6, 8, eaay0929, 2020

**A-3) Bozuyuk, U., Alapan, Y., Aghakhani, A., Yunusa, M., Sitti, M. Shape anisotropy-governed locomotion of surface microrollers on vessel-like microtopographies against physiological flows** *Proceeding of the National Academy of Sciences* 118, 13, 2021



## **2 Wrinkling Instability and Adhesion of Liquid Gallium Droplet**

---

Reprint from reference [123]  
Nano Lett. 2018, 18, 4, 2498–2504  
DOI: 10.1021/acs.nanolett.8b00164  
© 2018 American Chemical Society

## 2.1 Introduction

The mechanical behaviors of nanofilms in response to external stimuli could provide insights into the morphology of biological systems. Recent studies have explored the wealth of such behaviors by exposing two-dimensional (2D) films to various loading conditions [60,71,124–126] as well as conforming them to three-dimensional (3D) objects [127,128]. The fundamental response explored in these studies is the out-of-plane wrinkling that occurs to alleviate compressive stresses. Wrinkling has implications in morphogenesis, interfacial-crack trapping to enhance adhesion, patterning, and functional optical and electronic materials [59,129–132]. Also, this frustrated geometry is naturally observed during crystal growth on curved surfaces [133,134]. For instance, the growth of a native gallium oxide ( $\text{Ga}_2\text{O}_3$ ) nanofilm a few nanometers thick [135,136] on the surface of liquid gallium and eutectic gallium-indium metals could result in a crumpled topology.

Gallium-based liquid metals have garnered considerable attention recently as a result of their unique intrinsic mechanical, thermal, phase-changing, and electrochemical properties [8,57,137,138]. Liquid gallium (Ga) has a low melting temperature (29.7 °C) and low viscosity (1.95 mPa·s at 30.5 °C), roughly twice that of water [54]. Its toxicity compared to mercury (Hg) is negligible [139], and the vapor pressure at room temperature is low ( $< 1.33 \times 10^{-9}$  Pa) [140]. Ga-based liquid metals are attractive for a broad range of applications including flexible or stretchable sensors, microelectronics, 3D printing, reversible adhesives, and next-generation nanomechanical devices [28,31,37,141–144]. The  $\text{Ga}_2\text{O}_3$  skin of liquid Ga and its alloys is a robust elastic nanofilm that provides mechanical support to the bulk liquid metals, even upon mechanical deformation. The oxide nanofilm is readily formed as the liquid metal is exposed to oxygen by initially forming one unit cell layer thickness [135,140]. It then grows at an ambient atmosphere, attaining a thickness value up to 3 nm [136]. Although a few studies have been conducted on the wetting behavior of Ga-based liquid metals [145,146], there are none on the interfacial adhesion mechanics of a liquid Ga droplet when its  $\text{Ga}_2\text{O}_3$  skin comes into contact with a rigid substrate. In this study, we present the mechanical behavior of the highly bendable native oxide skin when compressed against a rigid flat substrate as it exhibits a fascinating wrinkling phenomenon, and its implications on the adhesion energy necessary to separate the interface. The  $\text{Ga}_2\text{O}_3$  sheet relieves the applied compressive stress at the contact interface by transitioning from a circular to radial wrinkled state.

The circular wrinkles enhance fracture strength by trapping cracks that propagate along the radial direction.

While the adhesive contact mechanics of such oxide nanofilms on a liquid metal droplet may appear analogous to that of elastomeric thin membranes filled with air [147–149], our nanofilm mechanics differ significantly. In this study, the oxide nanofilm encapsulates an incompressible fluid with a constant volume, while the reported inflated and deflated elastomer membranes were filled with air that was compressible and had a variable volume. Moreover, the elastomer membranes were highly stretchable while our oxide nanofilm is mainly bendable. A scanning electron microscope (SEM) image of fresh Ga droplet shows a highly crumpled oxide membrane with sharp ridges and vertices (Figure 2.1a). These out-of-plane deformations are to relieve in-plane stresses that are induced by defects including grain boundary and atomic dislocation [140,150]. However, Figure 2.1b shows the SEM of the Ga droplet covered with the oxide skin after being deformed by a given preload (force). Note that the oxide skin ruptured at a high load, evidenced by the dark spots, which are discontinuities due to cracks.

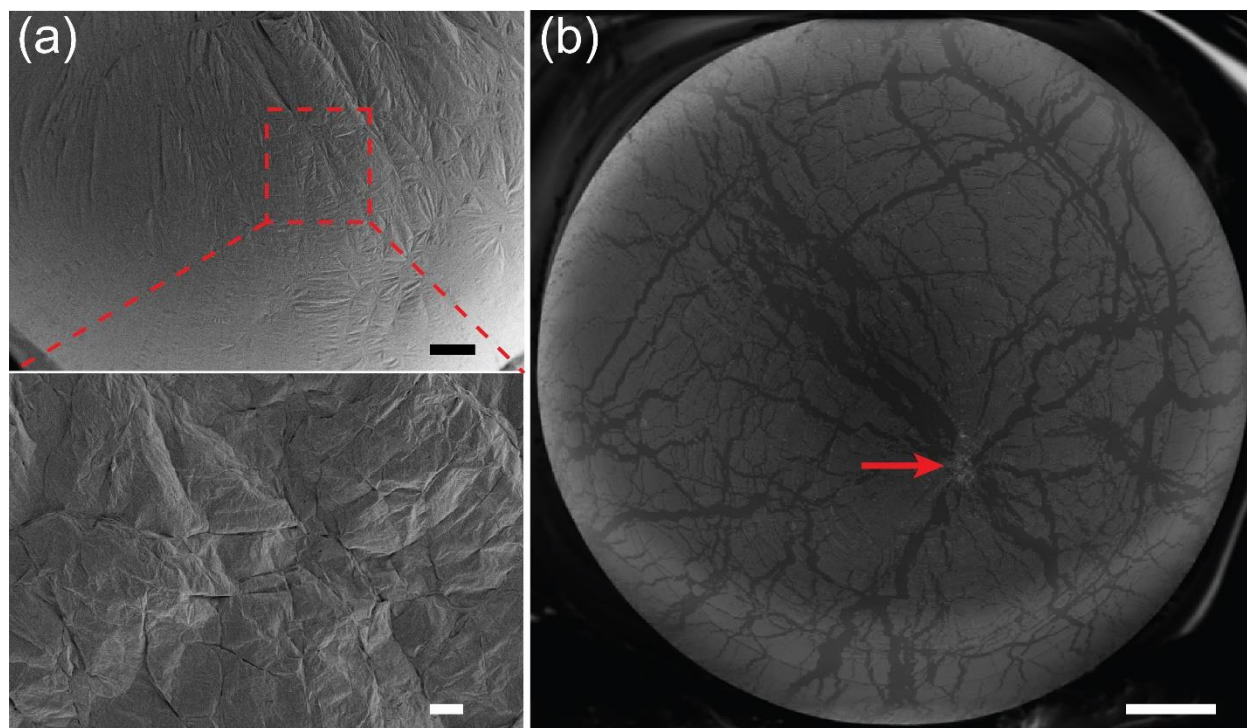


**Figure 2.1:** Morphology of the crumpled gallium oxide ( $\text{Ga}_2\text{O}_3$ ) nanofilm encapsulating a liquid-gallium (Ga) droplet. Scanning electron microscopy (SEM) images of the crumpled  $\text{Ga}_2\text{O}_3$  skin: (a) before contact with a smooth glass substrate and (b) after contact with a preload of 10 mN. The

scale bars are (a) 100  $\mu\text{m}$ , (a, inset) 20  $\mu\text{m}$ , and (b) 200  $\mu\text{m}$ , respectively. The arrow in (b) points to the center of contact of the Ga droplet.

## **2.2 Experimental Section**

### **2.2.1 Adhesion Setup**

Adhesion experiment studies were carried out using custom-made device to probe the mechanical deformation of liquid metal by leveraging its ability to remain liquid at room temperature. The force sensitive deformation of the liquid droplet was captured through force-distance relationship during loading and unloading. This method is widely employed in understanding Van der Waals adhesion of rigid surfaces and biological adhesion mechanism [151,152]. In this approach, the liquid metal droplet was compressed on a rigid surface where the adhesion between the flat substrate and the liquid metal encapsulated with native oxide was measured. Moreover, the adhesion experiment in combination with *in situ* phase transition experiment provided insight on the crystallization kinetics of supercooled liquid gallium.

### **2.2.2 Microscopic Characterization**

A scanning electron microscope (ZEISS ULTRA-55 SEM) technique was used for the characterization of wrinkle geometries of fresh gallium oxide skin that developed on the gallium droplet. The droplet was deposited on a PDMS post forming spherical cap of liquid Ga (Figure 2.1b).

## **2.3 Results**

### **2.3.1 Uniaxial Compression of Gallium**

A schematic of the experimental procedure for characterization of liquid Ga droplet on a smooth flat glass substrate is illustrated in Figure 2.2a. A hemispherical liquid Ga droplet was attached to the tip of a polydimethylsiloxane (PDMS) post with a 1.75 mm diameter. The setup was mounted on an inverted optical microscope. By means of a piezo stage, the Ga droplet was brought into

contact with a flat glass substrate, which has a root-mean-square (RMS) roughness of 1.23 nm (Figure 1.6), and the contact interface was recorded with a camera attached to the microscope. A secondary camera monitored the side profile of the droplet. The contact interface consists of the  $\text{Ga}_2\text{O}_3$  nanofilm with thickness ( $t$ ), contact width ( $W$ ), and height ( $H$ ) between the post and the flat substrate as seen Figure 2.2b. Force graph representation reveals steps of the experimental procedure when a droplet approached the rigid glass surface (Figure 2.2c). The PDMS post with the Ga droplet was mounted to a load cell and lowered (I) to establish contact with the substrate by the piezo motion stage with a constant speed of  $20 \mu\text{m/s}$  until a predefined compressive normal force (preload,  $F_{\text{pre}}$ ) was attained (II). The droplet was kept under preloaded condition for a dwelling time of 20 s (II-III). Then, the droplet was retracted with a constant speed of  $20 \mu\text{m/s}$  and the maximum negative force,  $F_{\text{off}}$ , during pull-off was achieved at IV. Note that V represents the lift-off (detachment) of the droplet from the contact interface. Here, after each experiment (from 0.1 to 10 mN), a new fresh Ga droplet was used for consistent measurements. The oxide nanofilm yielded and ruptured as the preload increased, such that cracks started to appear along the radial wrinkles and thus fresh new oxide was formed on the surface. All experiments were conducted at room temperature ( $20\text{-}25 \text{ }^\circ\text{C}$ ) with a relative humidity of approximately 25-35%.

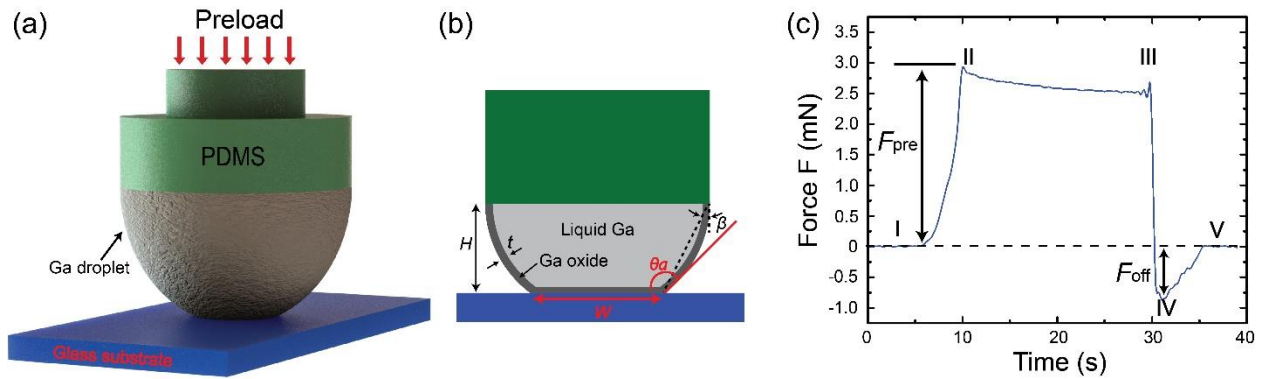


**Figure 2.2:** Experimental setup and geometrical parameters. (a) Schematic of the experimental setup with a Ga droplet (gray) attached to a PDMS post (green) and in contact with a flat smooth glass substrate (blue). (b) Side-view schematic of a cross-section through the central vertical plane depicting the measured geometrical parameters. The thin  $\text{Ga}_2\text{O}_3$  skin is displayed in dark gray, while the encapsulated liquid Ga is indicated in light gray. The parameters  $H$ ,  $W$ ,  $t$ , and  $\theta_a$  represent the height of the droplet between the PDMS post and the flat glass surface, contact width, thickness of the oxide skin, and the apparent contact angle of the droplet, respectively. (c) A representative force curve obtained from a measurement on the smooth glass substrate. Points I and V represent

approaching (contact point) and retraction (detachment point). Points II and III correspond to dwelling time. Points II and IV show the reaction points of the preload  $F_{pre}$  and pull-off force (adhesion)  $F_{off}$ , respectively.

**Force balance and interfacial tension:** By balancing the applied preload with the Laplace pressure of the bulging sides of the squeezed droplet [153], we estimated the apparent interfacial tension of the droplet at room temperature and pressure. Figure 2.3a-I depicts the side view geometry of a deformed liquid Ga droplet on a substrate at a preload of 4 mN. The force balance is expressed as:

$$F_{pre} = -\frac{2\pi W^2 \gamma}{4H} \cos \theta_a \quad (2.1)$$

where  $\theta_a$  is the apparent contact angle of the droplet (see Figure 2.2b), and  $\gamma$  is the apparent interfacial tension. Eq 2.1 is solved for the contact width  $W$ . The experimental observations are shown as the red dots in Figure 2.6b. The experimental data was fitted with a square root function using the curve fitting toolbox in Matlab (MathWorks, Inc., Natick, MA) with the apparent interfacial tension  $\gamma$  as a fitting parameter. All of the ensuing fitting was conducted using Matlab. The fit is represented by the dashed line in Figure 2.3b and has a coefficient of determination  $R^2 = 0.90$ .

We found an apparent interfacial tension of 0.591 N/m, which is remarkably close to the critical surface yield stress previously reported as 0.5-0.6 N/m using a rheometer [53,154]. The critical yield stress indicates the point beyond which the oxide nanofilm yields. In another study using the pendant-drop method, effective surface tension of 0.695 N/m was reported for a Ga droplet submerged in hydrochloric acid (HCl) bath of 1.0 M concentration [36]. The acidic environment inhibited the growth of the oxide nanofilm and so the effect of the surface yield stress was prevented. Note that the deviation observed in the fitting of our experiments may be associated with the surface yield stress based on the constant interfacial tension assumption. Moreover, it could also be affected by droplet pinning onto the PDMS post, which resulted in an asymmetric side deformation at the onset of bulging as the drive advances.

**Wrinkle modeling:** As the compression force is increased, a transition from circular to radial wrinkles occurs at the contact interface as shown in the microscopic images in Figure 2.3a-

II. The circular wrinkles are expected deformations of the thin oxide skin as its initial hemispherical shell geometry transitions to that of a flat disk during contact. The initial hemispherical geometry has a higher surface area than that of a flat disk; therefore, the excess skin folds into the liquid bulk to conserve the material. The analogy to this projection is similar to the map-maker's problem in which it is challenging to transform a sphere into a planar 2D surface [155]. The oxide was forced to conform to 2D region from 3D hemisphere. The length scale  $L$  (red circle) represents the transition point in which radial wrinkles will begin to form. We used a previously reported method for solving the problem of a thin sheet under axisymmetric loading [71]. This method solves the Föppl-von Kármán equations for the disc-like geometry of the oxide skin at the contact interface (see Figure A.1, Appendix A for detail), or:

$$\nabla \cdot \boldsymbol{\sigma} = 0 \quad (2.2)$$

$$\frac{Et^3}{12(1-\nu^2)} \text{Tr}(\boldsymbol{\kappa}) + \boldsymbol{\sigma} \cdot \boldsymbol{\kappa} = F_{pre} \quad (2.3)$$

where  $\boldsymbol{\sigma}$  is the in-plane stress tensor and  $\nabla$  is the gradient operator for the radial  $r$  and azimuthal  $\theta$  directions.  $E$  is the Young's modulus,  $\nu$  is the Poisson's ratio,  $\boldsymbol{\kappa}$  is the curvature tensor, and  $\text{Tr}(\boldsymbol{\kappa})$  is the mean curvature (see the note in Appendix A). The length scale  $W$  (yellow circle in Figure 2.3a-II) is the natural length scale because it represents the width of the region of interest of the thin elastic sheet.

The scale for force per unit length is  $PH \cos \beta$ , where  $P$  is the applied pressure at the contact interface, i.e.,  $P = F_{pre}/\pi(W/2)^2$ , and  $\beta$  is the angle between the points of contact between the Ga droplet and the post on the substrate. This scaling represents the force pulling on the edge of the elastic sheet and is an adaptation of the force scale from King *et al.* [71] to the case of a Ga droplet forced into contact with a flat substrate. The dimensionless governing ordinary differential equations (ODEs) can then be expressed as:

$$\partial_{\tilde{r}} \tilde{\sigma}_{rr} = \frac{1}{\tilde{r}} (-\tilde{\sigma}_{rr} + \tilde{\sigma}_{\theta\theta}) \quad (2.4)$$

$$\partial_{\tilde{r}} \tilde{\sigma}_{\theta\theta} = \frac{1}{\tilde{r}} (\tilde{\sigma}_{rr} - \tilde{\sigma}_{\theta\theta}) - \frac{Et(PW)^2}{8(PH \cos \beta)^3} \tilde{r} \frac{1}{\tilde{\sigma}_{rr}^2} \quad (2.5)$$

In our case, the dimensionless confinement parameter is:

$$\alpha = \frac{Et(PW)^2}{8(PH \cos \beta)^3} \quad (2.6)$$

This parameter represents the ratio of tensile stresses pulling the sheet towards and away from the center. By numerically solving the ODEs, we found that the hoop stress is tensile  $\sigma_{\theta\theta} > 0$  for confinement parameters below a critical value, or  $\alpha < \alpha^*$ , and the hoop stress becomes compressive,  $\sigma_{\theta\theta} < 0$ , for confinement parameters  $\alpha > \alpha^*$ . However, for sufficiently thin sheets, they are unable to withstand compression, thus resulting in bending and wrinkling. The bendability parameter,  $\epsilon^{-1} \equiv 12PHW^2 \cos \beta (1 - \nu^2) / (Et^3)$ , compares the bending and tensile forces in the sheet. Here,  $E \approx 230$  GPa [156]. We found high bendability of around  $10^6$ , which is close to the reported value ( $2 \times 10^5$ ) for a thin polymer sheet on a liquid droplet [71]. Note that  $E$  is most likely over-estimated, which makes our bendability value conservative. Therefore, for large confinement parameters  $\alpha > \alpha^*$ , we expect the roughly 3 nm thick oxide skin to bend under compression, resulting in zero hoop stress  $\sigma_{\theta\theta} = 0$ . Using asymptotic matching (see the note in Appendix A and ref [71], for details), we found the same power-law relationship between the radial wrinkle extent  $L$  and the confinement parameter  $\alpha$  as was found for a thin film on a liquid droplet [71]:

$$\frac{L}{W} = \left(\frac{\alpha}{\alpha^*}\right)^{-0.2} \quad (2.7)$$

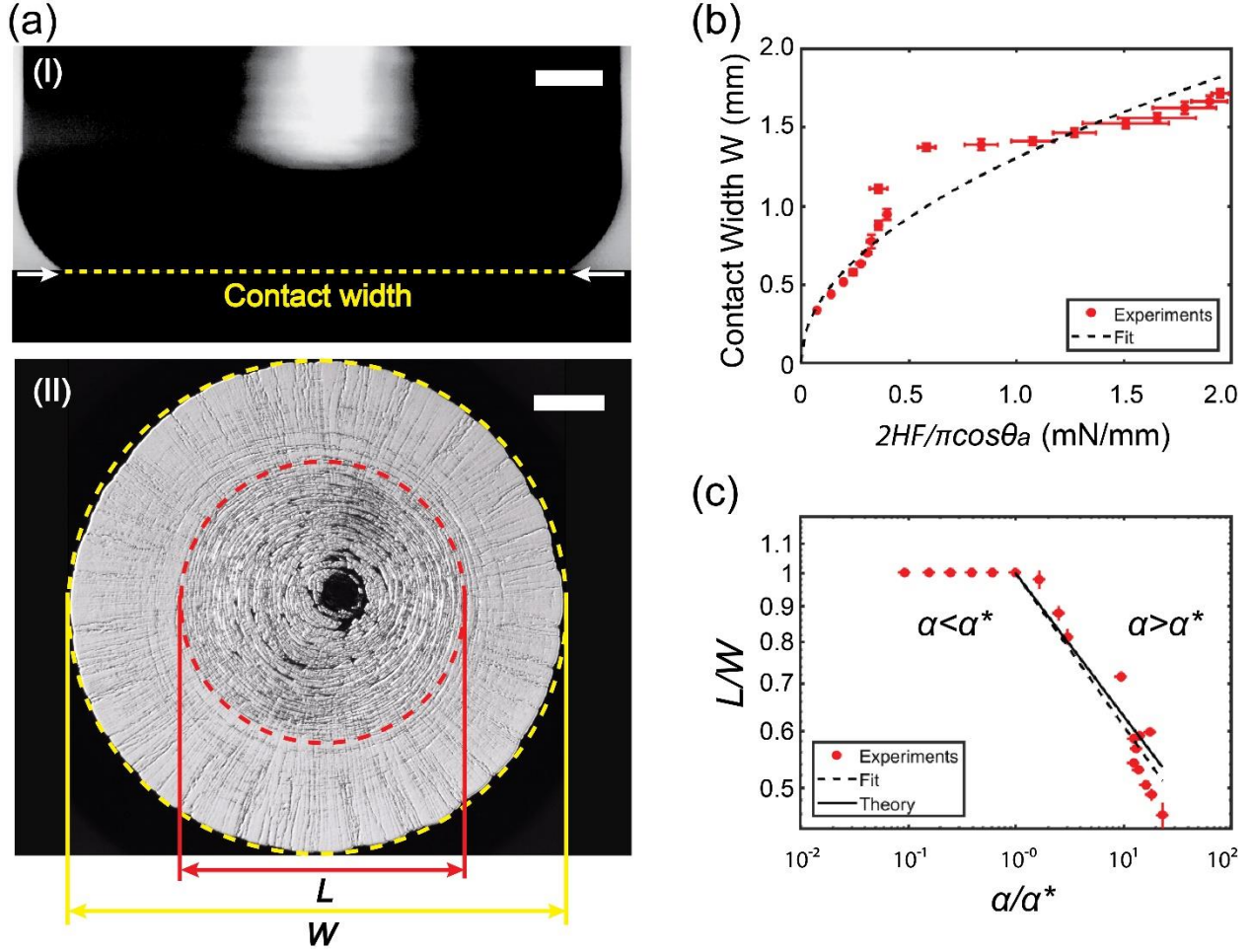


**Figure 2.3:** Liquid Ga and  $\text{Ga}_2\text{O}_3$  skin mechanics during preloading. (a) Liquid Ga droplet compressed against a smooth glass substrate with a preload of 4 mN. Panels I and II represent side and bottom views of the droplet, respectively. (b) Apparent interfacial tension fitting of the experimental data (red dots) using the theoretical model in eq 2.1. Black dashed line represents the square root fit for the apparent interfacial tension ( $R^2 = 0.90$ ). (c) Relationship between dimensionless radial wrinkle extent  $L/W$  and dimensionless confinement parameter  $\alpha$  (eq 2.6) normalized by the critical dimensionless confinement parameter  $\alpha^*$ , where the radial wrinkles initiated. Experimental data is depicted by red dots, experimental fit by the black dash line ( $R^2 = 0.89$ ), and theoretical prediction (eq 2.7) by the black solid line. Error bars represent standard deviation. The scale bars are 200  $\mu\text{m}$ .

Using controlled experiments, in which we varied the preload and thus the pressure  $P$ , we found the relationship between the dimensionless wrinkle extent  $L/W$  and the dimensionless confinement parameter normalized by the critical value beyond which radial wrinkling occurs  $\alpha/\alpha^*$  for our system. We found the critical confinement parameter as  $\alpha^* = 1.01$ . The best power-law fit for the experimental data, represented by the dashed line, was determined to be  $-0.21$  with a coefficient of determination  $R^2 = 0.89$  (Figure 2.3c). In addition, the number of radial wrinkles increased with increasing preload (Figure 2.4).

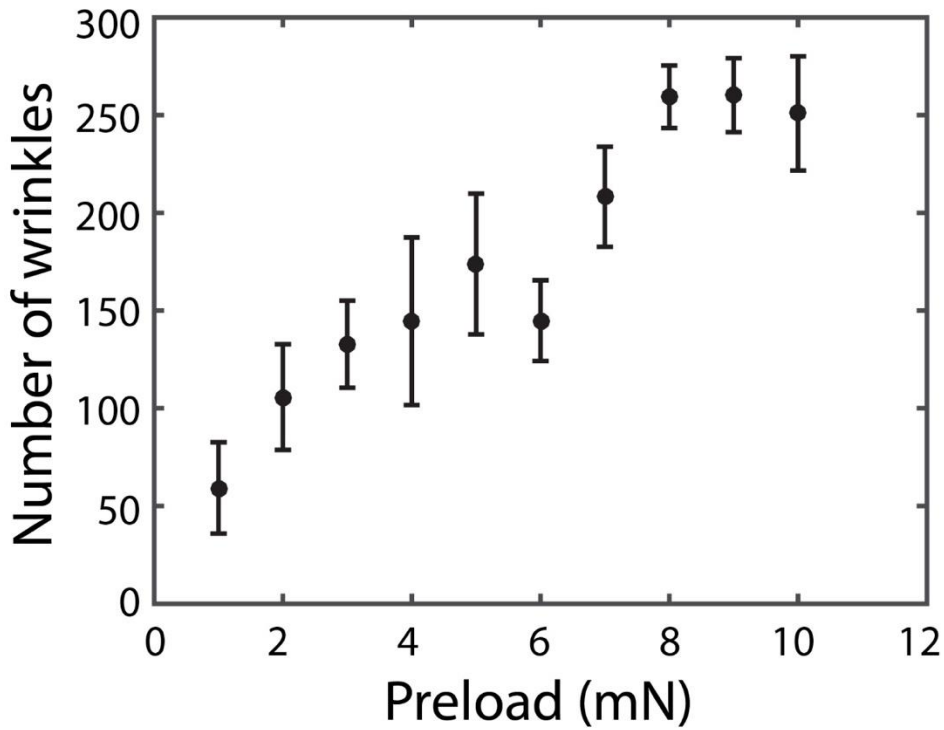


**Figure 2.4:** Relationship between number of wrinkles and preload. As preload is increased, the number of radial wrinkles also increased. Error bars represent standard deviation.

### 2.3.2 Droplet Deformation and Residue Analysis

Deposited residue of liquid Ga, adhesion dependent on preload, and interfacial energy were determined. We analyzed the contact interface on the glass substrates after each experimental cycle as seen in Figure 2.5. A clean contact surface was selected after each adhesion experiment while increasing the preload from 0.1 to 10 mN. At low preloads, up to 2 mN, Ga residue is not discernible on the glass substrate. From 3 mN and above, residue of Ga oxide can be observed at the contact interface, outlined by the blue circle. During higher preloading, radial oxide stripes are left on the substrate. Interestingly, the oxide skin can self-heal when it ruptures and spontaneously reconstructs. In light of this, new fresh oxide can grow upon exposure to oxygen leading to a slight increase of surface area of the  $\text{Ga}_2\text{O}_3$  layer in the process (Figure A.2, Appendix A).

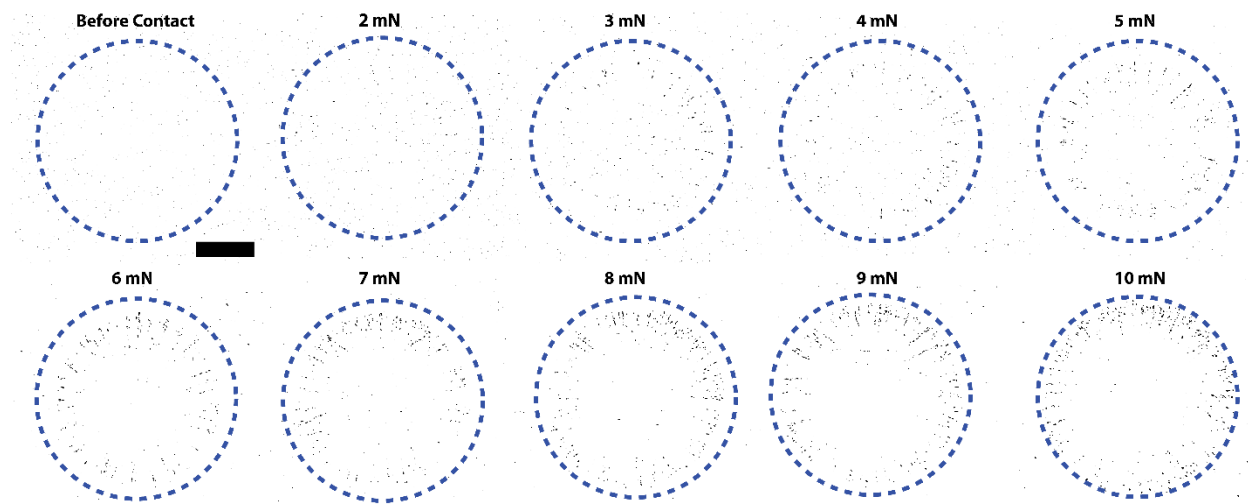


**Figure 2.5:** Adhesion characterization and residue deposition during pull-off. (a) Inverted light microscope images of the glass substrate before and after the liquid Ga is brought into contact with the glass substrate for varying preloads. The blue-dashed circle represents the contact area of the liquid Ga. The black spots are residues left behind by the liquid Ga. The scale bar is 0.5 mm.

To determine the deformation range and load dependence attribute of the compressed droplet, we show how  $F_{\text{off}}$  varied with the applied preload,  $F_{\text{pre}}$ , in Figure 2.6. The inset images (panels I-III) depict the side view of the spherical Ga droplet in contact with the flat glass substrate for applied preloads of 2, 5, and 10 mN, respectively. We observed a slight increase of  $F_{\text{off}}$  with

increasing  $F_{\text{pre}}$ , which may be related to the formation of fresh new oxide as a result of yielding. Specifically, when the preload is increased from 4 to 10 mN, we observed an increase of pull-off force by 48%. Along with this increase in  $F_{\text{off}}$ , we observed a 58% increase in contact area (Figure A.3, Appendix A).

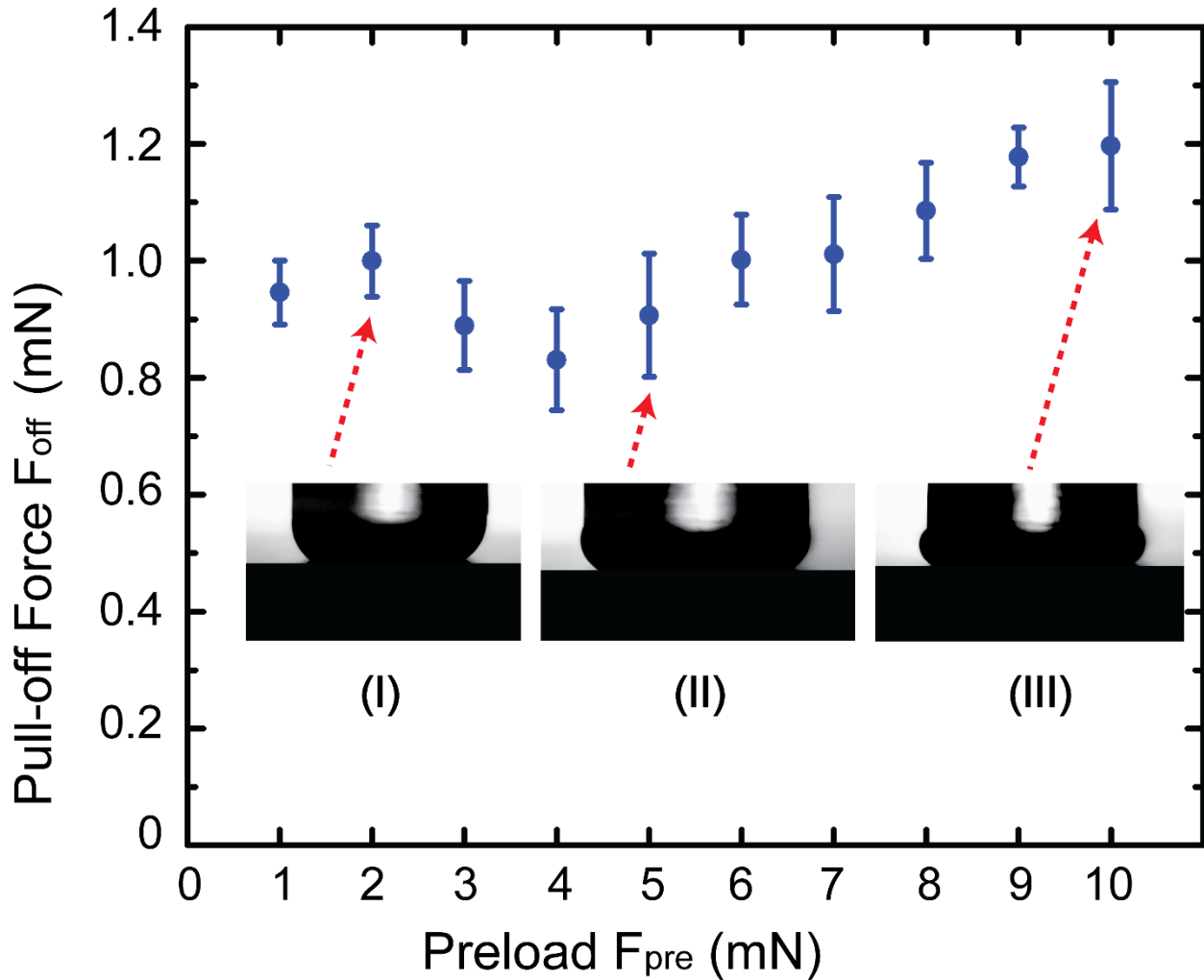


**Figure 2.6:** Relationship between pull-off force,  $F_{\text{off}}$ , and preload  $F_{\text{pre}}$ . Inset images show side views of the liquid Ga drop under different preloads.

The contact area dependency on the applied preload is shown in Figure A.4a, Appendix A, where both pull-off and the contact area exhibit the same trend. The pull-off force and the contact area saturated at higher preload condition. Upon close inspection, we show rate independence of pull-off force at different retraction speed (Figure A.4b, Appendix A).

### 2.3.3 Adhesive Stress and Surface Energy

To gain more insight into the oxide-skin rupturing mechanism, we evaluated the adhesive stress  $\sigma_{ad} = F_{off}/\pi(W/2)^2$  in Figure 2.7a, which shows an asymptotic decay with increasing preload, and is believed to be related to fracture strength and nanofilm yielding. At lower preloads (yellow-shaded region in Figure 2.7a), before transition from circular to radial wrinkles, adhesive stress is maximum, which correlates to high fracture strength during pull-off. The circular wrinkles act as discontinuities during crack propagation to trap the crack front, and thus, higher stress is required for the crack to advance further. The crack propagated in an intermittent fashion toward the center upon retraction. Such crack trapping mechanism can be found in biological adhesive soft pads of insect (e.g., the cricket *Tettigonia viridissima*) and synthetic materials [132,157]. An intermediate state exists at about 1 to 2 mN, after the radial wrinkles have emerged and the oxide skin was still intact (unshaded region in Figure 2.7a). Beyond the 2 mN threshold (red-shaded region Figure 2.7a), the oxide membrane cannot support the applied compressive stress, thereby rupturing along the radial wrinkles. The radial wrinkles are oriented parallel to the crack propagation front and do not significantly affect the adhesion. The stress levels off within the range of 0.5 - 0.6 kPa due to the increased contact area.

We further analyzed the interfacial energy of the Ga droplet on the glass substrate, assuming the droplet together with the Ga<sub>2</sub>O<sub>3</sub> nanofilm behaves like a fluid. In principle, bulk Ga liquid behaves like a Newtonian fluid. Therefore, the separation energy of the droplet at lift-off can be related to the normal pull-off force and the contact length at separation (*i.e.*, the triple contact circumference). This implies that when the pull-off force acting perpendicular to the contact length is plotted against the triple contact circumference, a linear graph passing through the origin should be obtained with a slope corresponding to the interfacial surface energy,  $\gamma_{sl} = F_{off}/\pi w \sin \theta_a$  [158].

In Figure 2.7b, we show the relationship between  $F_{\text{off}}$  and  $(\pi w \sin \theta_a)$  for the Ga droplet, in which  $\theta_a$  is the apparent contact angle of the droplet in the contact line vicinity during the maximum pull-off (Figure A.5, Appendix A). As shown, we observed a linear relationship passing through the origin with a slope of  $0.238 \pm 0.008 \text{ J m}^{-2}$  ( $R^2 = 0.98$ ). Our interfacial adhesion energy ( $0.238 \text{ J m}^{-2}$ ) is greater than the work of adhesion of solid Ga previously reported based on the Johnson-Kendall-Roberts (JKR) theory ( $0.182 \text{ J m}^{-2}$ ), and it is in good agreement with the adhesion energies of thin sheet nanomaterials such as graphene ( $0.27 - 0.40 \text{ J m}^{-2}$ ) [37,159,160].

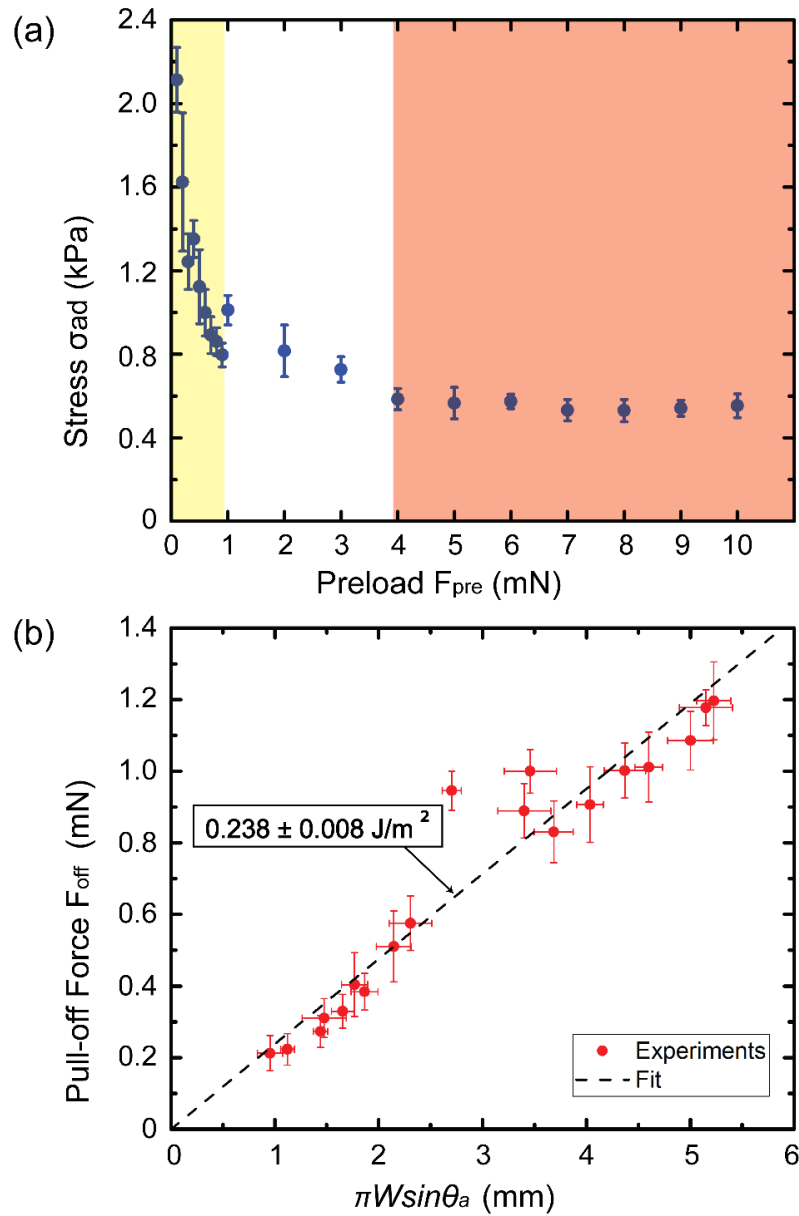


**Figure 2.7:** (a) Relationship between adhesive stress  $\sigma_{ad} = F_{off}/\pi(W/2)^2$  and preload  $F_{pre}$ . The yellow-shaded area represents preload conditions before the circular to radial wrinkling transition with high adhesive stress. The non-shaded area represents the condition in which circular and radial wrinkles coexist after the transition. The red-shaded area represents the condition in which the oxide membrane yields and ruptures because of high preloading. (b) Relationship between pull-off force  $F_{off}$  and vertical component of the contact perimeter  $\pi W \sin \theta_a$ . Experimental data is represented by red dots. The slope of the best linear fit (black dashed line,  $R^2 = 0.98$ ) represents the effective surface tension and surface energy. Error bars represent standard deviation.

## 2.4 Summary

The crumpled oxide nanofilm (Figure 2.1a) is the precursor to the wrinkling phenomenon we observed, which reveals the fundamental interfacial mechanics between the liquid Ga and the rigid glass substrate. Symmetry instability at high preloads results in bending and wrinkling to relieve the applied in-plane stress of the oxide film. Consequently, the highly bendable skin ruptures through the radially wrinkled regions at higher preloads, thus depositing oxide on the substrate. The wrinkling behavior closely follows established models for nanofilms under axisymmetrical loading, thus providing a new platform for studying wrinkling of thin films under external stimuli. Wrinkling is a familiar morphological instability in developmental biology (*i.e.*, morphogenesis), and its evolution has implications in soft tissue growth, from tumor development and invasion to biofilm expansion [161]. Notwithstanding the complex contact mechanics of the oxide skin, the adhesion between the Ga droplet and flat rigid substrate was found to be equivalent to that of a Newtonian fluid droplet on a flat rigid substrate, even across two orders of magnitude in preload. Through our analysis, we are capable of predicting the contact geometry and subsequent adhesion effectivity for a given preload. Additionally, we can predict when the oxide nanofilm ruptures and leaves residue on the surface, which may further facilitate cost-effective room-temperature 2D patterning of liquid Ga for future semiconductor applications [141]. Understanding the behavior of droplets encapsulated in thin membranes could also help improve food processing quality, cosmetics, and drugs. In short, our findings provide the tools for the precise control of liquid-metal interfaces.

# **3 Crystallization Kinetics and Interfacial Properties of Gallium**

---

Reprint from reference [47]

Adv. Mater. 2020, 32, 10, 1907453

DOI: 10.1002/adma.201907453

©2020 The Authors. Published by WILEY-VCH Verlag GmbH & Co. KGaA, Weinheim

### 3.1 Introduction

Understanding the crystallization process is essential in many research areas, such as phase-change (PC) memory [162,163], protein crystallization [164], biomineralization [165], pathologies [166], and semiconductors [167]. Crystallization occurs in two steps: nucleation and growth [78,164]. The nucleation of liquid is ubiquitous in nature and facilitated by active sites, such as impurities and surface irregularities (e.g., cleavages, atomically sharp wedges, and pores) [78,168–170]. Nucleation plays a crucial role in PC materials, where structural changes from amorphous to crystalline state is triggered by electrical or optical stimulation. For instance, Loke *et al.* [163] reported an ultrafast crystallization speed of 500 ps in Ge<sub>2</sub>Sb<sub>2</sub>Te<sub>5</sub> (GST) material by applying a constant low voltage via pre-structural ordering (incubation) effects. Simpson *et al.* [171] demonstrated an optical excitation with laser-based time-resolved pulses to investigate the interfacial crystallization of superlattices in GeTe–Sb<sub>2</sub>Te<sub>3</sub>. In addition, crystallization kinetics have been investigated in glass and supercooled liquids [162,172]. Despite a decade of advances in PC materials research, there are only a few studies on dielectric capping and stress conditions in PC device cells [75,173–176]. Therefore, a detailed study of the interface materials and crystallization temperature is still missing to unfold the potential of PC materials.

Many technological liquids, such as Si, Ge, Bi, and GST, exhibit supercooling behavior [162,167,169]. In casting technology, reducing the supercooling of liquid melts is vital in tailoring microstructure. The degree to which a liquid can be supercooled depends on the nature of the contacting solid wall [177]. Also, surface-induced crystallization is important in forming extended single-crystalline texture in supercooled liquids due to surface layering of atoms, molecules, and charged colloids adjacent to the solid walls of substrates [167,178–181]. In addition, single-crystal texture formation through physical confinement and uniaxial magnetic field have been demonstrated [182]. However, direct experimental evidence of the link between the interfacial temperature and the surface layering effect is still missing. Similarly, supercooled liquid Ga exhibits surface layering in contact with a hard wall of a diamond substrate [183]. Ga can be supercooled to  $-28\text{ }^{\circ}\text{C}$ , or  $58\text{ }^{\circ}\text{C}$  below its freezing point ( $29.8\text{ }^{\circ}\text{C}$ ) [184]. Because of its cost effectiveness and accessibility, Ga is an interesting material in phase transition (PT) studies. Ga also shows a promising potential in monatomic PC memory devices for data storage [77], superconductivity [185], metamaterial [186], and reversible adhesion [37].

To reverse the supercooling of liquid Ga, external perturbations are applied to induce nucleation and subsequent crystal growth [180,185,187]. Even though molecular liquids are promising candidates to study phase transformation at ambient pressures and moderate temperatures, it is rather difficult to practically monitor the exact site of nucleation, since nucleation is a stochastic process [164,169]. Here, we study crystallization of supercooled liquid Ga and vividly reveal the temporal change of its liquid-to-solid PT at the interface between the liquid Ga and different hard substrates.

### 3.2 Experimental Section

**3D printing of the post:** A cylindrical polymer (VeroClear material) post was printed using a 3D printer (Objet260 Connex, Stratasys Ltd.). The post has outer diameter of 3 mm, inner diameter of 2.5 mm, and a height of 5 mm. A hole cavity placed at the center along the length of the post compartmentalized an electrical resistor for heating purpose (Figure 3.1). The printed post was thoroughly cleaned in 1 M NaOH solution. It was then attached to a threaded metal holder to facilitate attachment onto a force sensor for adhesion measurement. A silicone adhesive (Sil-Poxy, Smooth-On Inc.) was applied between the metal and the base part of the plastic post. After curing at room temperature for 30 min, the two parts were strongly bonded.

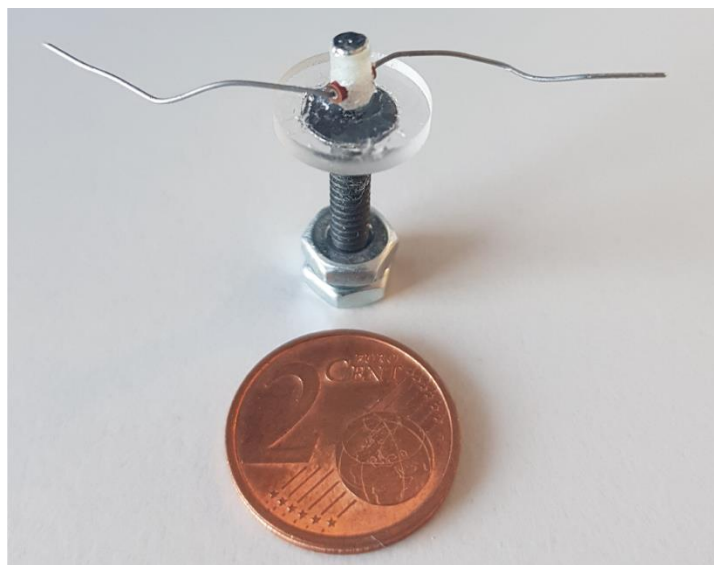


**Figure 3.1:** An illustration of 3D printed device assembled with all components.

**General handling warning:** Gallium-based liquid metals corrode metal surfaces, especially aluminum (Al). Therefore, careful handling of Ga and its alloys is recommended to avoid damage to instruments and equipment including microscopes and all devices composed of Al components.

**Deposition of the liquid Ga droplet onto the post:** Melt of Ga was prepared by heating commercially available pure liquid Ga (Gallium, 99.99%, ACROS Organics™) to 65 °C. After homogeneous heating, supercooling effect was induced. A 44 mg of the supercooled Ga was injected into the cavity at the center of the post, which then bulged at the tip of the post forming a hemispherical cap. The injected liquid metal was in thermal contact with a resistor inserted half-way in the cavity. This resistor is used to dissipate heat via Joule effect, to melt the Ga droplet. Finally, the post was mounted onto the force sensor with the liquid metal droplet attached.

**Adhesion measurement setup:** A customized adhesion measurement setup mounted on an inverted optical microscope (Axio Observer A1, Zeiss) with a video camera (Grasshopper3, Point Gray Research Inc.) was used to visualize the phase contrast images at the contact interface. The force between the sample and the substrate was measured by a high-resolution load cell (GSO-25, Transducer Techniques). The load cell was mounted to a high-precision piezo motion stage (LPS-65 2", Physik Instrumente GmbH & Co. KG) in the vertical  $z$  direction, with a resolution of 5 nm and maximum velocity of  $10 \text{ mm s}^{-1}$ . A long-ranged motor stage (M-605 2DD, Physik Instrumente GmbH & Co. KG) was used in  $y$  direction with  $1\text{-}\mu\text{m}$  resolution and high maximum velocity up to  $50 \text{ mm s}^{-1}$  [123].

**Humidity and temperature control:** Both environmental temperature and humidity were monitored using a commercially purchased sensor (Humidity/Temperature/Dew Point Meter, Fisher Scientific). The humidity ranged from 26 to 45% and the room temperature range was 22 to 25 °C. A six-channel handheld temperature data logger (OMEGA RDXL6SD, Omega Engineering, Inc.) was used to monitor *in-situ* temperature of both Ga and the surface. Heating and cooling temperature controller (BTC-1-100 and BTC-SLM, Bioscience Tools) was used to regulate the environment temperature. To harvest dissipated energy for direct heating of Ga, a 220 Ohm resistor was connected in series to a 9 V power source. The heat energy dissipated by the

resistor can raise up the temperature of the droplet instantaneously up to 60 °C, which is enough to melt the solid Ga instantly (the Ga melting temperature: 29.8 °C).

**Microscopic characterization:** A scanning electron microscope (Zeiss Ultra 500 Gemini SEM, Carl Zeiss Inc., Oberkochen, Germany) was used to characterize the seeding crystal surface and the area of the Ga droplet, which contacted to the substrate. Energy dispersive x-ray spectroscopy (Bruker, Billerica, MA) was performed using an accelerating voltage of 15 keV on the seeding crystal and the solidified Ga droplet. 3D laser scanning microscope (Keyence VK-X200) was used for characterizing surface topology of the substrate.

**X-ray diffraction (XRD) measurements:** XRD characterization was obtained with D8 Advance Bruker using a Cu-K $\alpha$  ( $\lambda = 1.5418 \text{ \AA}$ ). A glass substrate and the crystallized Ga were first cooled in liquid nitrogen prior to XRD measurement to prevent any structural disorder such as surface melting of the solid crystal. Lattice constants for XRD measurements were determined from ICDD card no: 03-065-2493 for Ga. All samples were prepared at ambient room temperature.

**Differential scanning calorimetry (DSC) analysis:** Thermal analysis were obtained by Discovery DSC 2500 (TA Instrument). Heating or cooling rate of 5 °C min<sup>-1</sup> with modulation amplitude of 0.32 °C to detect the endothermic and exothermic peak for the crystallized samples on different substrates. The sample mass was around 5 mg.

**Substrate materials:** All the substrates utilized in the experiments are commercially available. Zinc selenide, sapphire, and silicon substrates (discs) with 5 mm thickness and 25 mm diameter (Thorlabs. Inc.), a glass slide of 1 mm thickness and 120-160 nm thick ITO-coated glass slide (Sigma Aldrich), and a copper plate  $\geq 99.9\%$  (metal basis) with a thickness of 6.35 mm (Alfa Aesar) were used as the substrate materials. The copper plate was polished to maintain the same magnitude of nanoscale roughness across all target surfaces. Root-mean-square (RMS) roughness values of the smooth glass, ITO coated glass, ZnSe, sapphire, silicon, and polished copper substrates are 53, 61, 43, 54, 39, and 105 nm, respectively. The RMS roughness of frosted glass substrate is 1.41  $\mu\text{m}$ .

### 3.2.1 Supercooling Effect and Recalescence Point

A commercially available pure Ga (Gallium, 99.99%, ACROS Organics) was heated in an oven at 65 °C for an hour to assure a homogeneous melting of the complete solid to the liquid state. As such, a supercooled melt of Ga was obtained. The supercooled liquid was obtained as a result of overheating the liquid above the melting point of Ga (29.8 °C). The induced supercooling can only be reversed when the melt is cooled down to negative temperature. In this state, the supercooled liquid Ga was stable for at least 6 months without undergoing any phase transition. A droplet of the liquid metal was poured into a plastic holder with a cavity fitted with a thermocouple device to monitor the phase transition of the liquid and recalescence point. A thermocouple device was fitted entirely into to the liquid metal droplet while the temperature profile was registered using an Omega data logger (RDXL6SD). Due to the size of the droplet and high thermal conductivity  $28.2 \text{ W m}^{-1} \text{ K}^{-1}$  Ga [188,189], the temperature across the droplet of Ga was assumed to be uniform across the droplet during measurement. In addition, a 220 Ohm resistor connected to a 9 V battery was used to deliver the heat required to melt the droplet (Figure 3.2a).

To control the crystallization of the supercooled melt, seed crystal made of solid Ga was obtained from the supercooled Ga melt. The solid seed crystal was brought into contact with the metastable liquid Ga, thereby inducing crystallization of the supercooled Ga. We monitored the transformation using the thermocouple embedded inside the liquid metal. The recalescence point as the crystallization initiates at room temperature was observed in Figure 3.2b after the seeding crystal contacted the droplet. The crystallization is a first order transition where heat is dissipated into the environment as a result of an exothermic process, then the temperature of the droplet continued to rise. To make sure our method is repeatable, 5 cycle of seeding crystallization was repeated consecutively (Figure 3.2c). Moreover, the degree of overheating to induce supercooling in Ga was investigated in Figure 3.2d. By only heating Ga to 31 °C (~ 1 °C above its melting point), the solidification of Ga was unavoidable during cooling to room temperature. However, the supercooled state was very stable at room temperature when overheated by just more than 5 °C above the melting point of Ga.

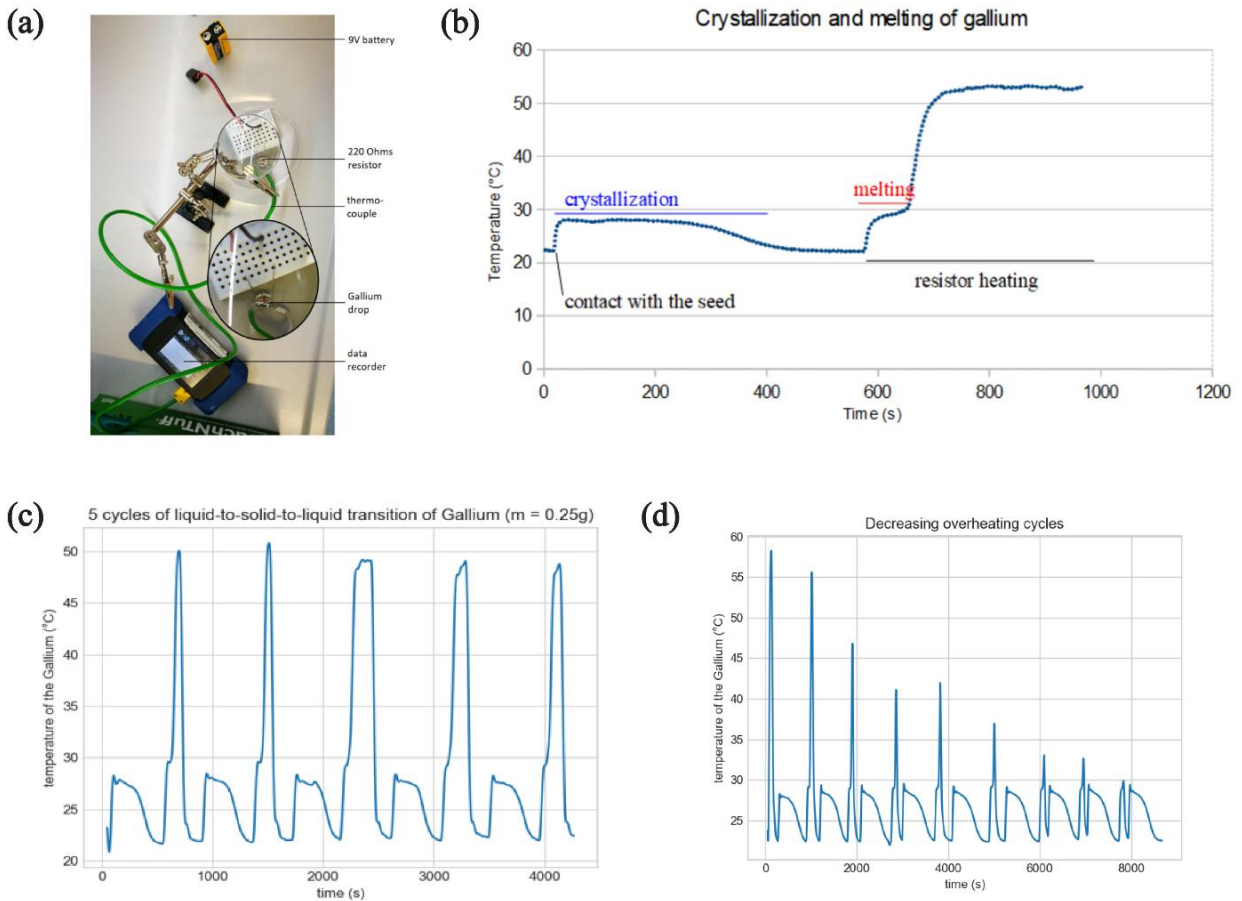


**Figure 3.2:** Supercooling and seeding crystallization. (a) Experimental set-up to measure temperature of the Ga during crystallization and melting. Melting of solid Ga crystal was realized through resistive heating by the resistor and the crystallization by contact with a solid Ga seed. The temperature was measured using thermocouple device. (b) Temperature curve monitored during crystallization of the droplet. Heating with the resistor allows melting of Ga and overheat it to benefit from the supercooled state when heating stops. (c) Repeatability of the process cycle with the same Ga drop, but different seeds to induce the crystallization as the seed melts and merges with the Ga drop in the melting phase. (d) Effect of overheating on supercooling state. For an overheating below 2 °C, the crystallization initiates spontaneously, whereas it only occurs after a contact with the seed crystal for higher overheating.

### 3.2.2 Analysis of Crystal Fraction During Crystallization Process

The crystallization process was monitored via an inverted optical microscope where videos were acquired through a transparent substrates. The recorded video frames of crystallized fraction were analyzed using Python's scikit-image library [190]. In order to follow the crystal growth in the

melt, the frame of the drop on the substrate right before crystallization is subtracted from each following frame sequence.

To precisely extract the crystal from the remaining image, a robust process of image segmentation method (watershed segmentation) [191] based on mathematical morphology was used. The image was binarized and only the largest interconnected area, corresponding to the crystal, was selected. This allowed the accurate measurement of the crystal surface growth as a function of time.\* To model the fraction of crystal growth, the obtained crystallized data sets were fitted using the well-known JMAK model [192].

As the droplet got larger, the rate at which heat dissipated by the substrate through the interface was limited by the material properties, such as thermal conductivity. This nonequilibrium dynamics caused the experimental data to deviate from the model because the crystallization is a self-limiting process. The fractional amount of the Ga crystallized depended on how fast the heat was driven away from the contact interface. To test the hypothesis of heat transfer at the interface, the crystallization time of droplets with different radii deposited onto polystyrene was measured. Let  $S$  be the surface area of the drop,  $V$  the volume,  $M$  the mass, and  $r$  the radius, then:

$$M \sim V \sim r^3 \quad (3.1)$$

$$S \sim r^2 \sim M^{2/3} \quad (3.2)$$

$$\ln(S) \sim \frac{2}{3} \ln(M) \quad (3.3)$$

If the phase-change energy dissipates through the surface then  $T_{crystallisation} \sim S \sim M^{2/3}$ . When plotting in logarithm of the crystallization time as a function of the mass, we found the slope of  $2/3$  within the confidence interval of the regression, validating this hypothesis (Figure 3.3). Therefore, the crystallization depends on the surface-to-volume ratio of the Ga and the substrate capacity to act as a heat sink.

---

\* <https://github.com/Alienor134/crystallization> [223]

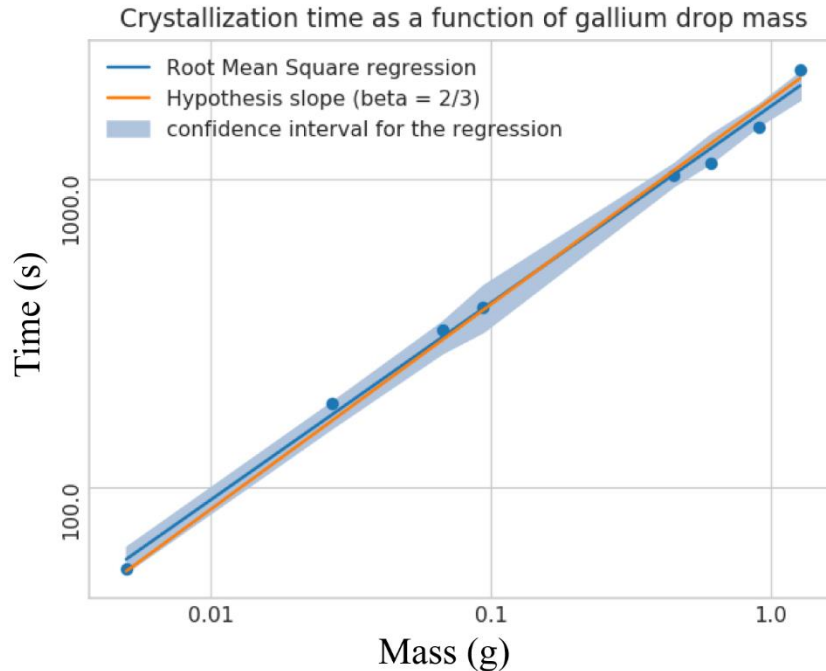
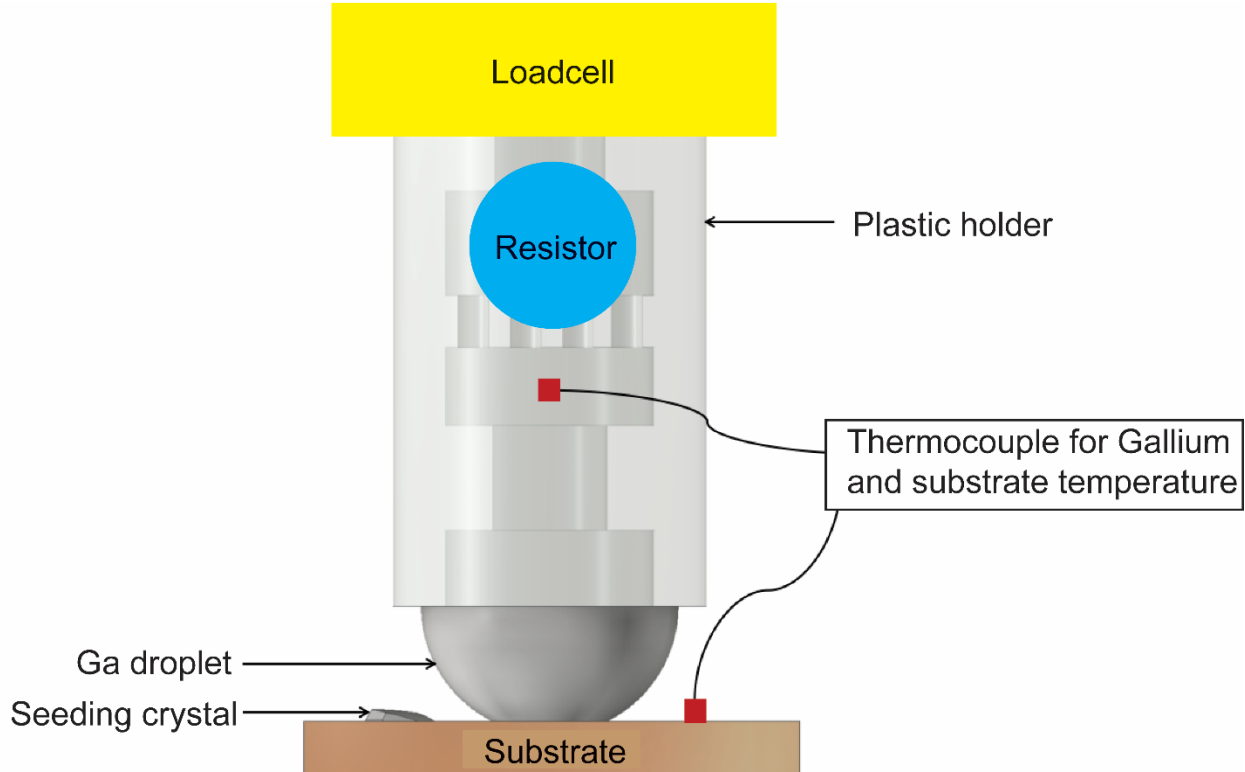


**Figure 3.3:** Relationship between the crystallization time and the droplet mass. The crystallization time depends on the power  $2/3$  of the mass, supporting the hypothesis that the energy of phase transition dissipating through the interface limits the crystallization speed.

### 3.3 Results and Discussion

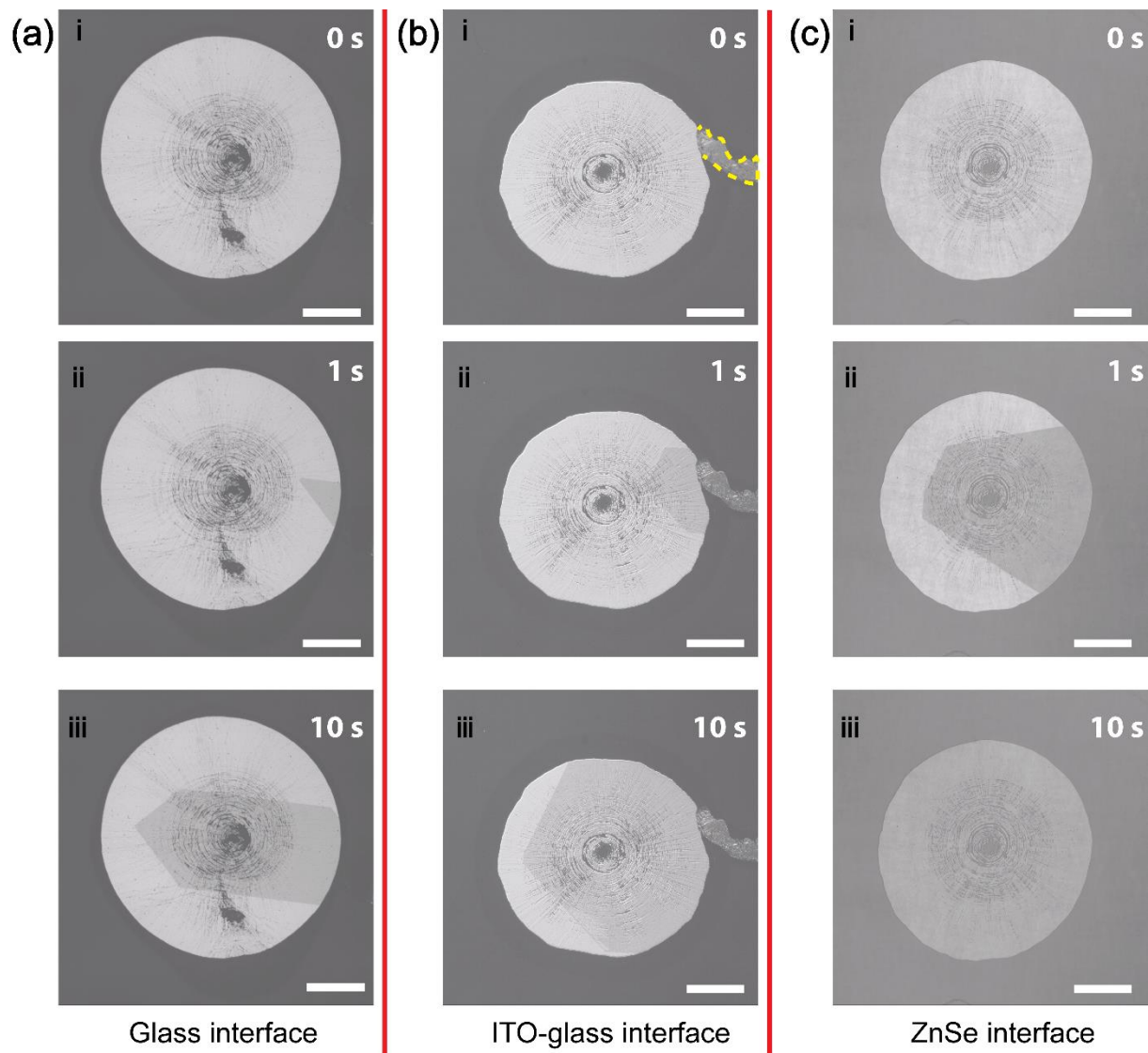
#### 3.3.1 Crystallization Kinetics

Prior to crystallization experiment, supercooled liquid Ga droplet embedded in cavity was attached to a loadcell device as depicted in Figure 3.4. The device was lowered gently on to the substrate surface at a constant speed of  $200 \mu\text{m s}^{-1}$ , attaining a compression load of 10 mN. The supercooled Ga droplet conformed to the substrate forming circular and radial wrinkles at the interface [123]. The wrinkling instability emerged at the interface to relieve the applied compressive stress. The crystallization of the liquid droplet was realized through a contact with a seeding crystal of solid Ga [180]. We visualized the spatiotemporal evolution of the crystallization dynamics on transparent glass, indium tin oxide coated glass (ITO glass), and zinc selenide (ZnSe) substrates.



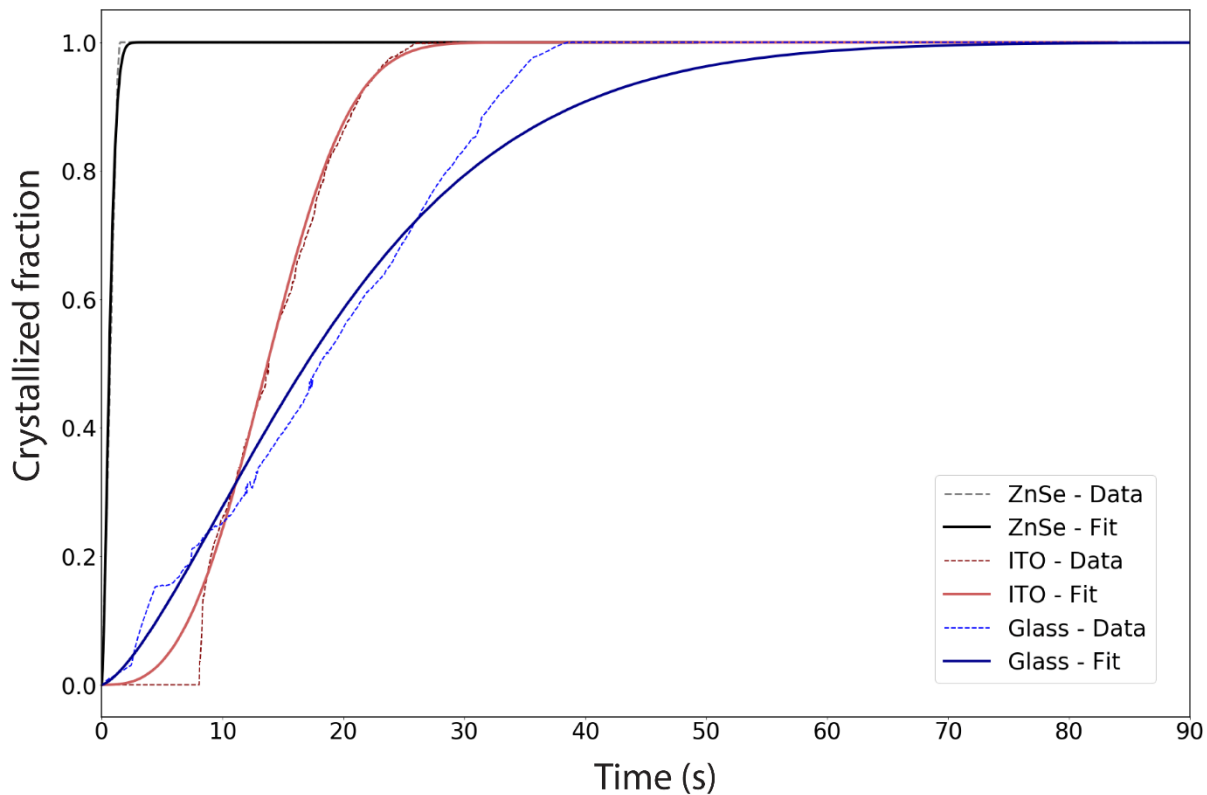
**Figure 3.4:** Device schematic for the crystallization kinetics study. Ga droplet in contact with different substrates at different thermal conditions. A 3D-printed plastic holder encased the supercooled Ga droplet attached to a loadcell. The thermocouple monitored the temperature profile between the Ga droplet and different substrates during crystallization. A resistor inside the holder was used to heat the droplet on demand.

Figure 3.5a-c show the snapshots of the crystallization front and the corresponding time lapse of the crystallized fraction of Ga on the substrates. When compared to the glass substrate with low thermal conductivity ( $0.94 \text{ W m}^{-1} \text{ K}^{-1}$ ), the crystal growth rate was fast on the ITO-glass substrate owing to the high thermal conductivity of the ITO coating ( $10.2 \text{ W m}^{-1} \text{ K}^{-1}$ ). Similarly, a fast crystal growth rate was obtained on the ZnSe substrate ( $18 \text{ W m}^{-1} \text{ K}^{-1}$ ).



**Figure 3.5:** Contact interface and crystallization front visualization and characterization. (a), (b), and (c) Inverted optical microscope video snapshots of the interface through optically transparent substrates showed seeded crystallization kinetics at the interface. Depicted images are phase-contrast optical microscope images of the crystallization. The front propagated from right side (point of contact) to the left side of the images. The snapshots of crystallization kinetics were taken from individual droplets using a 1.75 mm post diameter at the interface of glass (a), ITO-glass (b), and ZnSe (c) substrates. The yellow dashed line represents the outline of the seeding crystal seen in the right side of the contact interface of ITO-glass (b-i). Similar seeding method was used for glass and ZnSe. Time lapses of the crystallization kinetics appeared on each corresponding image. Scale bars are 400  $\mu\text{m}$ .

We used an image-processing algorithm (python) to track the crystal front of a 1.75 mm diameter droplet through the transparent contact interfaces (Figure 3.6) [190]. The Johnson-Mehl-Avrami-Kolmogorov (JMAK) equation was used to calculate the volume fraction crystallized,  $X$ , which increases with time  $t$  according to  $X = 1 - \exp[-(kt)^n]$ . We assumed a 3D growth, where  $n = 3$  [192].



**Figure 3.6:** Fraction of the crystallized Ga on glass, ITO-glass, and ZnSe substrates.

The model agreed well with the experimental data, which showed the relation between the heat dissipation of the crystallized fraction of Ga as dominated by the thermal conduction by the interface material as seen in the case of small droplets in Figure 3.6. Further, as the droplet mass increased, slower growth rate was observed due to the dependence of the substrate capacity to dissipate heat during the crystallization process (Figure 3.7).

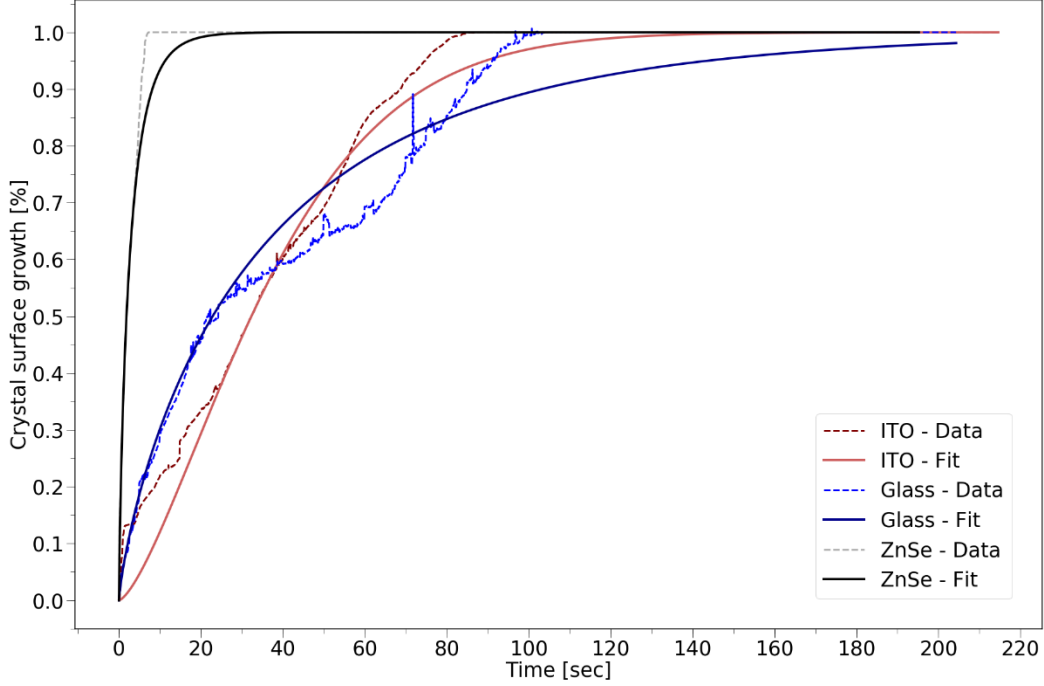


**Figure 3.7:** Crystallization of a large droplet and effect of the heat trapped at the interface. Crystal growth fraction on different transparent substrates. The data are collected for a large a droplet encapsulated in sample-holder with a diameter of 2.5 mm. The crystallization time is longer because of the surface-to-volume effect of heat dissipation. The heat of fusion deposited on the substrates therefore increased the surface temperature of the substrates depending on the heat dissipation capacity of the material. Limited heat dissipation through the substrates could be associated to the discrepancy in glass and ITO-glass measurement due to low thermal conductivity. Thus, instantaneous annealing of the crystallized fraction was realized in the confined space that resulted in highly ordered structure.

### 3.3.2 Interfacial Heat Dissipation Mechanism

To understand the physical mechanism of heat dissipation at the substrate-droplet interface, we used the heat conduction model reported by de Ruiter *et al.* [193]. The model predicts the droplet interfacial temperature  $T_{d,int}$  upon crystallization as:

$$T_{d,int} = T_{s,o} + (T_{d,o} - T_{s,o}) \frac{1}{1 + e_s/e_d} \quad (3.4)$$

where  $e_i = (K\rho c_p)_i^{1/2}$  is the effusivity ( $i = s$  for substrate and  $i = d$  for droplet),  $T_{d,0}$  and  $T_{s,0}$  are the initial droplet and surface temperature, respectively,  $K$  is the thermal conductivity,  $\rho$  is the density, and  $C_p$  is the heat capacity. The effusivity ratio determines how much heat is driven away from the interface. For a large effusivity ration,  $e_s/e_d \gg 1$ , heat can be transported away easily transported from the interface and therefore  $T_{d,int.} = T_{s,o}$ . For a small effusivity ratio,  $e_s/e_d \ll 1$ , heat will be trapped at the interface and therefore  $T_{d,int.} = T_{d,o}$ , given that  $T_{d,o} = T_m = 29.85\text{ }^\circ\text{C}$ . In Figure 3.8a, we show how the thermal conductivity of substrate affects the crystallization process. The experiments were performed on different transparent and non-transparent substrates with higher thermal conductivity including sapphire, silicon, and copper to verify the heat dissipation mechanism based on the thermal conduction model. Note that, in the case of Ga, we assumed that the initial droplet temperature was the same as the fusion temperature due to the induced supercooling effect. On the dielectric glass surface, the heat released during fusion was trapped at the interface, and therefore the interface temperature was elevated close to the melting temperature ( $T_m$ ) of Ga. However, heat is rapidly dissipated at the interface when the thermal conductivity of the substrate is high (e.g., ZnSe, sapphire, silicon, and copper substrates). The heat released by the Ga droplet is dissipated via the substrate through thermal diffusion. The thermal conductivity of the substrate limits how much heat can be dissipated. The thickness of the substrates was chosen to satisfy the requirement for a semi-infinite surface (see Tables B.1 and B.2, Appendix B).

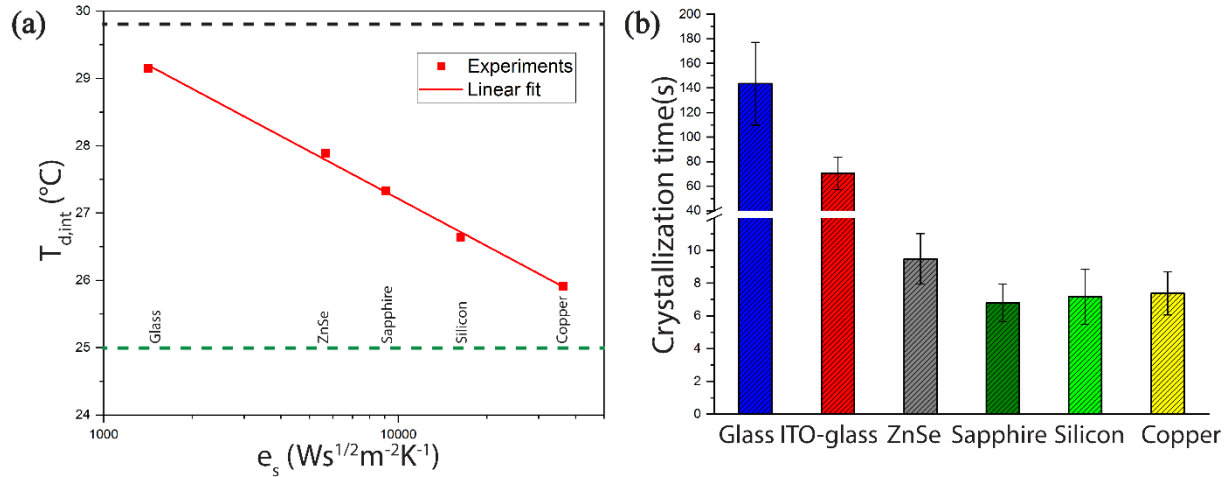


**Figure 3.8:** Droplet interfacial temperature and adhesion characterization using in situ temperature probing. (a) Interfacial temperature measurements on different substrates.  $T_{d,int}$  was calculated using eq 3.4. The dashed green and black lines represent the initial substrate temperature ( $T_{s,0} = 25^\circ C$ ) and the initial droplet temperature ( $T_{d,0} = 29.85^\circ C$ ), respectively. Red line represents the linear fitting of the data points ( $R^2 = 0.99$ ). (b) Crystallization time measurement results of different substrates with decreasing thermal conductivity. (b) Crystallization time measurement results of different substrates with increasing thermal conductivity.

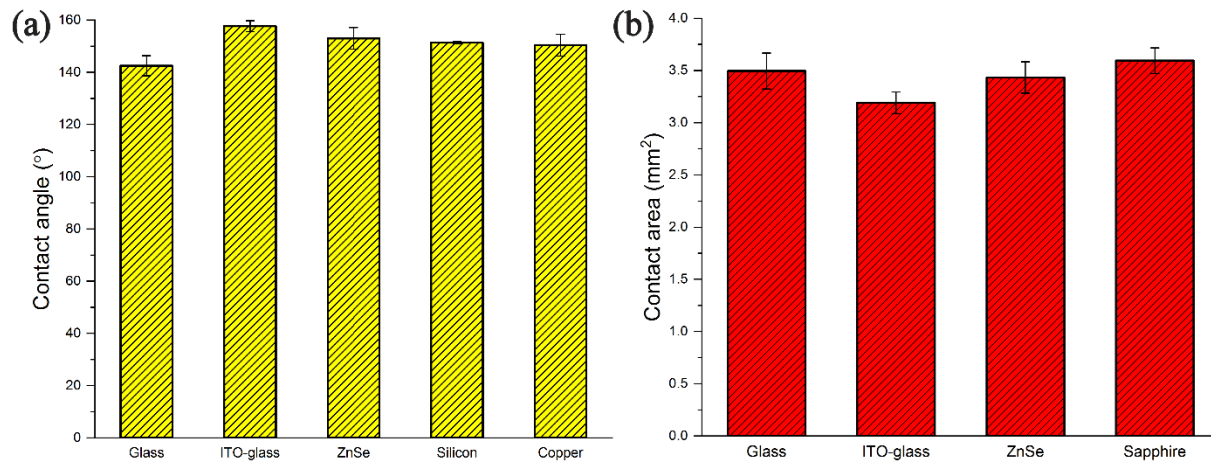


**Figure 3.9:** Wetting contact angle and the surface area of the crystallized Ga droplet on a 1.75 mm-diameter post. The droplets in the measurements are conformed to the surface with a preload of 5 mN and thereafter crystallized on the individual substrates to be able to measure the contact angle using a Contact Angle Goniometer (a). Apparent contact area when Ga in contact with all only transparent target substrates (b).  $N = 5$ .

The characteristic length scale of diffusion is defined by  $\tau_d = L^2/\alpha_{diff}$ , where  $L$  is the thickness and  $\alpha$  is the thermal diffusivity. The crystallization time decreased with increasing thermal conductivity of the respective substrates (Figure 3.8b). Different wetting behavior of Ga on the substrates resulted in a slight variation in contact angle measurements (Figure 3.9a). Therefore, the apparent contact area measurement showed a negligible variation within the transparent substrates (Figure 3.9b).

### 3.3.3 Solidification and Interfacial Adhesion of Supercooled Ga Droplet

To investigate the interfacial adhesion of the supercooled Ga on different substrate materials, we performed force measurements of the crystallized Ga droplets whereas *in-situ* temperature measurement enabled precise characterization of both the crystallization and adhesion as shown in Figure 3.10. The temperature profile was crucial in determining the starting and ending of crystallization, especially when the substrate was opaque. We harnessed the heat dissipated by the resistor attached to the device to melt the Ga droplet. The melting process was a sharp first-order transition at a fixed temperature under constant pressure. Supercooling of about 29 °C was induced after superheating the droplet by 7.7 °C. A Peltier device was used in Figure 3c to cool down the liquid Ga droplet to 0 °C. without undergoing solidification. The crystallization was only achieved by seeded growth. The driving force of crystallization (the Gibbs free energy difference between the crystalline phase and the supercooled liquid,  $\Delta G$ ) is related to the latent heat of melting  $\Delta H_m$  and the melting temperature  $T_m$  by the equation:  $\Delta G \cong \Delta H_m \frac{\Delta T}{T_m}$ , where  $\Delta T$  is the supercooling temperature ( $T_m - T$ ) and  $\Delta H_m = 5585 \text{ J mol}^{-1}$  for Ga [185].

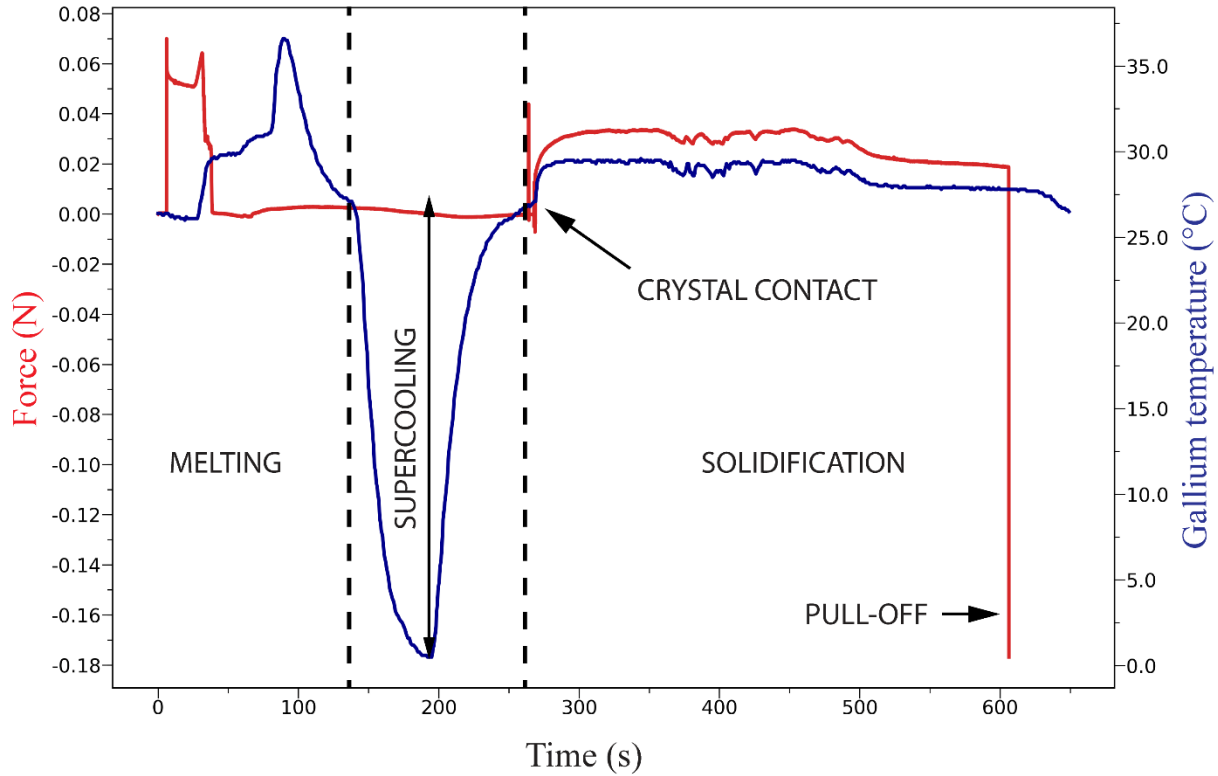


**Figure 3.10:** In-situ temperature measurement is superimposed on the adhesion curve of the supercooled Ga droplet (2.5 mm post diameter) on the dielectric glass substrate. The melting region is where the melting of the solid Ga takes place. The temperature of Ga is plotted in blue color, while the force curve is plotted in red. Once the melting is over, the temperature increased rapidly to 37.5 °C at a heating rate of 1 °C s<sup>-1</sup>. Overheating the droplet during melting induces the supercooling. Dropping the temperature to 0 °C shows the supercooling degree where Ga remains in its liquid state without undergoing crystallization, unless contacted by the seeding Ga crystal (blue line). The solidification region is where the crystal growth progressed. The pull-off force is the measure of adhesion upon separating the Ga droplet from the substrate.

The seeding material made of Ga crystal had surface irregularities and sharp wedges of the lamella morphology as revealed by the SEM images. It is important to note that the irregularity and crevice on the seeding crystal could acts, as nucleation center for the crystallization as such is ubiquitous in nature (Figure 3.11). Solidification process usually occurred at the wall of a container through heterogeneous nucleation. However, in supercooled liquids, metastability of the liquid state prevents the formation of stable nucleus in the liquid. For a stable nucleation to occur, the critical nucleus of solid clusters in a melt must be achieved according to Gibb’s approximation.

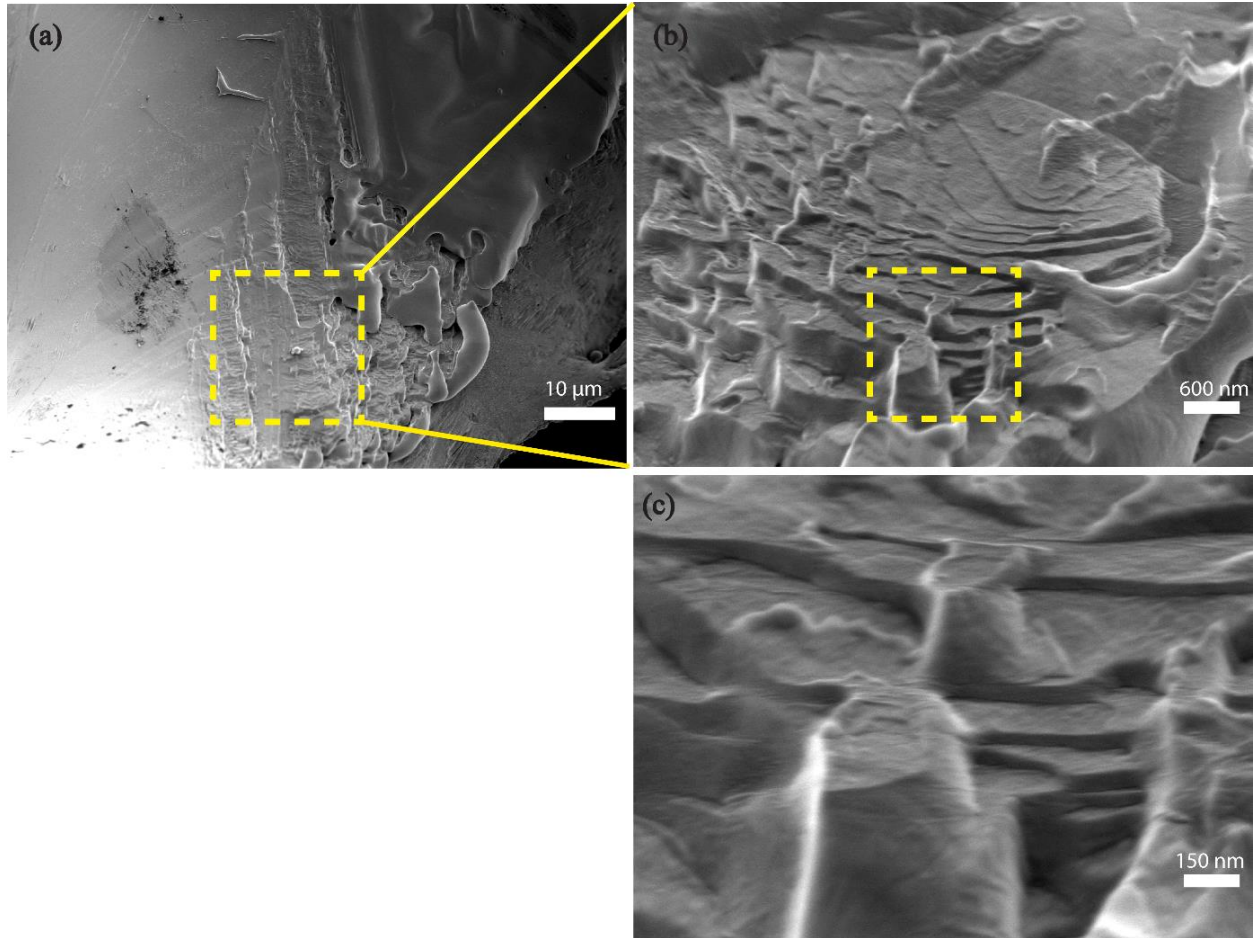


**Figure 3.11:** Scanning electron microscopy (SEM) images of the Ga seed topology. The surface of the seeding Ga crystal appears to have a nanoscale sharp edges and wedges that are layered in lamella-like structure. Image (b) shows the magnified yellow-dotted square in (a), and (c) is the magnified yellow-dotted square in (b). The seeding crystal was formed from the supercooled Ga melt under isothermal condition.

When the crystallization is completed, the loadcell was retracted at a constant speed of  $200 \mu\text{m s}^{-1}$  in order to measure the adhesion between the solid droplet and the substrate (Figure 3.11). The robustness and repeatability of the seeding method was investigated in Figure 3.2. The adhesion characterization of Ga in both liquid and solid states measured on different substrates is shown in Figure 3.12.

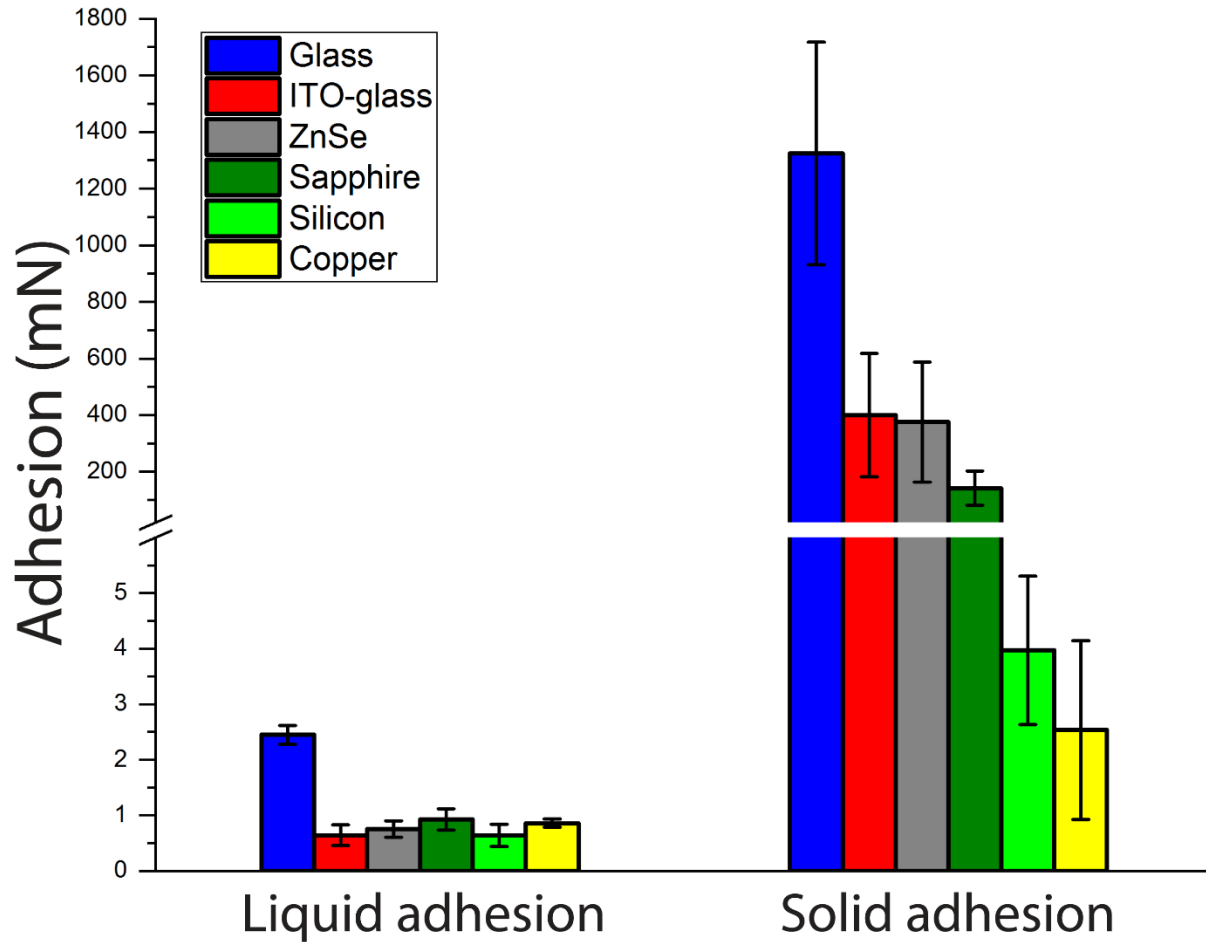


**Figure 3.12:** Adhesion measurement results of the liquid and solid Ga droplet on different substrates with increasing thermal conductivity. The standard deviation is based on 4 to 6 repeated experiments.

The adhesion reduced drastically on the thermally conducting substrates such as silicon and copper due to fast crystallization kinetics and peeling of the crystallized droplet. Thermal stress is dominant over adhesion stress at the interface of silicon and copper. Moreover, by keeping the surface temperature high, close to Ga melting point, the peeling effect during crystallization was reduced and the adhesion increased even on copper substrate (Figure 3.13). To grasp better understanding of the adhesion results, surface roughness effect was evaluated by measuring adhesion on a rough frosted glass.

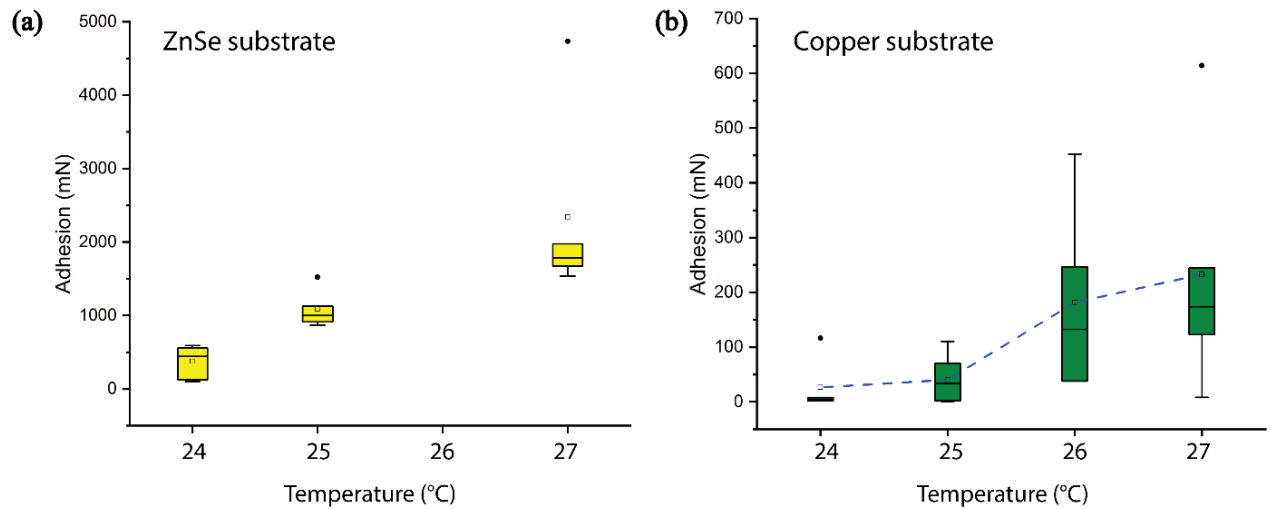


**Figure 3.13:** Effect of initial surface temperature of substrates on adhesion. The adhesion shows temperature dependence, which corresponds to the homogeneous crystal formation at an elevated temperature of 2 – 3 °C above the room temperature. Experimental data points  $n = 4$  to 6. The black dots are points outside the bounds of the whiskers or outliers. The adhesion increases as the substrate temperature increased on both (a) 5 mm ZnSe and (b) 6.4 mm copper substrate.

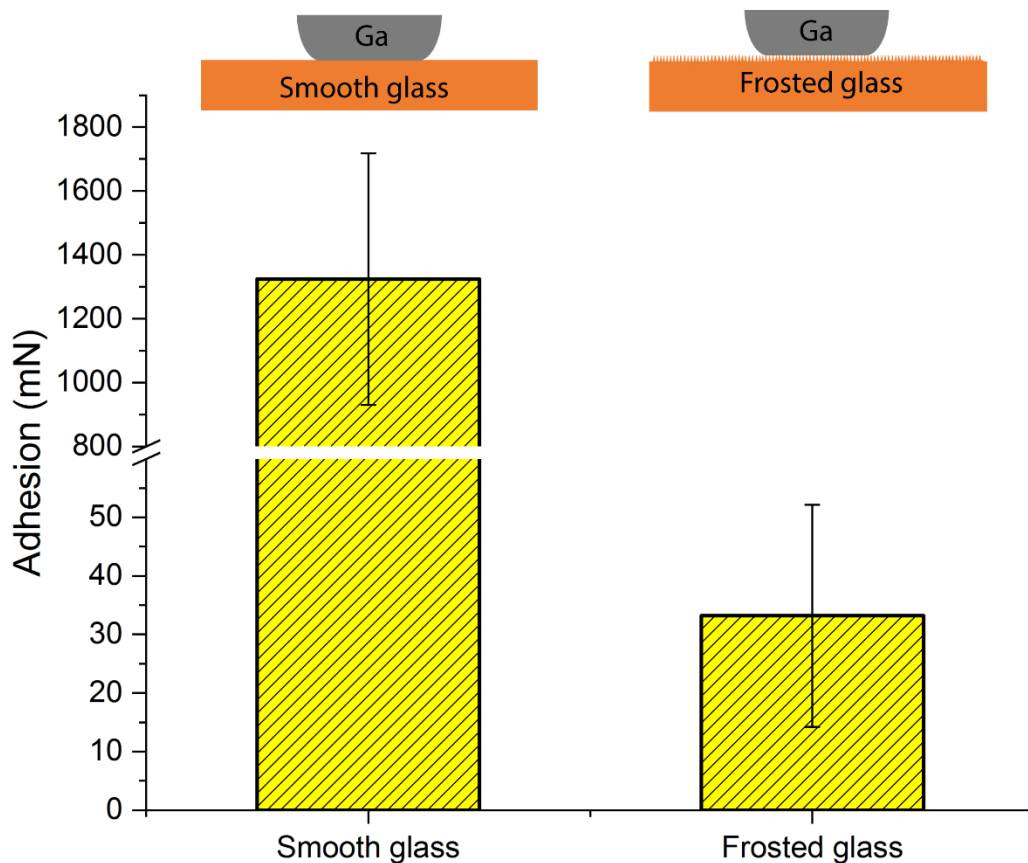


**Figure 3.14:** Adhesion variation due to the surface roughness effect. On a frosted glass, the adhesion decreased sharply due to high roughness level (root-mean-square roughness of around  $1.41\ \mu\text{m}$ ) compared to smooth glass substrate ( $53\ \text{nm}$ ).  $N = 5$ .

The adhesion reduced by an order of magnitude on the rough glass compared to the smooth one due to high-amplitude roughness (root-mean-square roughness of around  $1.41\ \mu\text{m}$ ) (Figure 3.14), which reduced the real contact area of the liquid Ga on the surface. Despite low adhesion of Ga on rough surfaces, it is much better than dry elastomeric adhesives on rough surfaces due to better conformity [194]. Energy-dispersive X-ray (EDX) spectroscopy of both the seeding crystal and the crystallized droplet were used to evaluate the composition of Ga (Figure B.1, Appendix B).

### 3.3.4 Single Crystal Formation and X-ray and Thermal Analysis

Interestingly, when quenched at a high temperature, the crystallized Ga on ZnSe and sapphire conformed to the substrates with an extended smooth crystal structure due to a slow growth rate. On the contrary, the crystal growth was multi-faceted (dendritic) when quenched at a low surface temperature, which resulted in a fast growth rate.

Two key factors that gave rise to the smooth and dendritic crystal formation in the supercooled liquid Ga are worth elaborating. First, surface layering of the adjacent atoms or molecules in the supercooled liquid provided the pathway for the formation of the extended single-crystal. Since surface layering is not however, restricted only to the hard wall of the substrate, it could occur at the interface of the nanometer-thick oxide skin of the liquid metal, which can serve as a precursor for the single-crystalline formation at the interface [179,195]. Second, slow growth rate as a result of limited heat dissipation contributed to the formation of the smooth single-crystalline texture through instantaneous annealing effect of the low melting point Ga at the interface. This typical crystallization scenario is prevalent on the dielectric glass substrate, where heat released during fusion was trapped continuously at the contact interface. As mentioned previously, the implication of instantaneous annealing on ZnSe and sapphire was verified. On these surfaces, conventionally, the fast cooling rate is due to their capacity to dissipate thermal heat because of their high thermal conductivity.

By keeping the surface temperature at 27 °C ( $0.9T_m$  of Ga) throughout the crystallization process, the crystal growth was similar to the smooth single-crystalline Ga seen on the dielectric glass substrate, with crystallization front propagating across the liquid in one direction forming a uniform crystal layering on the substrates. In addition, we verified the crystalline structure of an extended solidified Ga on large area substrates. The supercooled liquid was confined between the substrate and a glass-capping layer (Figure 3.15). The crystal was grown via the seeded growth method from the liquid.

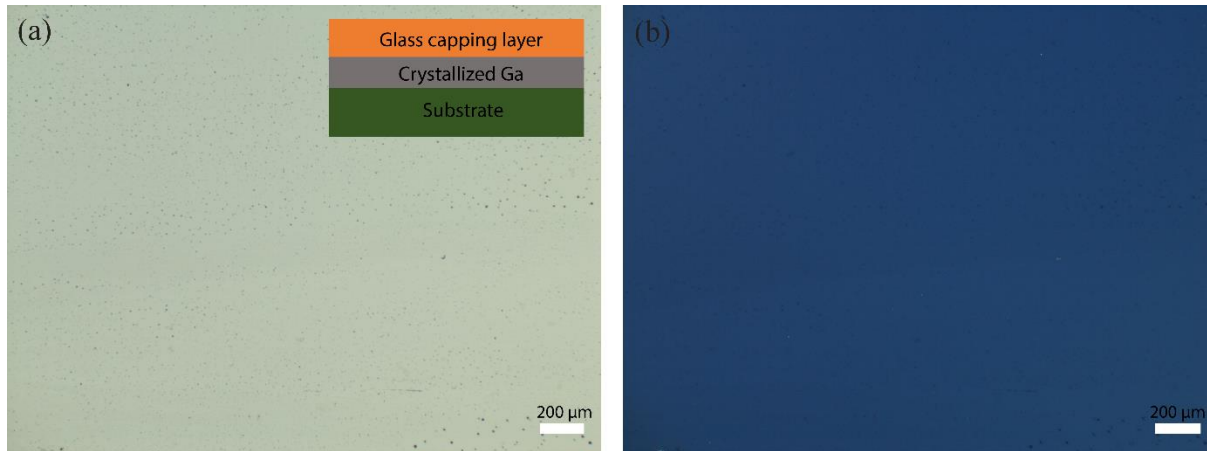


**Figure 3.15:** Large area single-crystal formation. (a) Optical microscope image of a large area single-crystal obtained by confinement of the supercooled liquid Ga between two glass substrates. The inset schematic represents the preparation method. Seeded growth of the crystal was initiated by contacting the liquid with a seed crystal. Large area single-crystal up to of  $0.5 \times 2 \text{ cm}^2$  was fabricated on different substrates at room temperature. (b) Polarized optical micrograph of the single-crystal in (a).

X-ray diffraction (XRD) measurements revealed a highly ordered, extended single-crystalline structure of  $\alpha$ -Ga when crystallized between glass/glass or sapphire/glass-capping (Figure 3.16a). The  $2\theta$  scan using  $\text{CuK}\alpha$  radiation showed strong peaks of (020), (040), and (060) preferred orientation from the (010) family. The room temperature crystallized bulk  $\alpha$ -Ga had an orthorhombic crystal structure with space group  $Cmca$  ( $a = 4.519 \text{ \AA}$ ,  $b = 7.657 \text{ \AA}$ ,  $c = 4.526 \text{ \AA}$ ) and contained eight atoms in the conventional unit cell. The calculated d-spacings were  $b/2 = 3.8 \text{ \AA}$ ,  $b/4 = 1.9 \text{ \AA}$ , and  $b/6 = 1.3 \text{ \AA}$ , which agree with the reported literature values.[196] The preference of the single-indexed crystal planes of (010) family on the substrate could be attributed to the surface energy minimization. The formation energies with respect to  $\alpha$ -Ga of (010) orientation (0.36 eV per atom) was lower than that of (100) orientation (0.64 eV per atom) [5]. This indicates better stability of (010) at room temperature up to  $T_m$ . The atoms between two Ga layers along (010) are bonded covalently and show directionality with a mixture of covalent and metallic properties. In a previous study, it was reported that a perfect single-crystal structure of solid Ga could form on sapphire substrate in a nanodroplet of supercooled Ga [197]. In addition, the XRD measurements revealed a repeating ordered structure with a peak at  $38.2^\circ$  and  $44.4^\circ$  when crystallized on ITO glass, ZnSe, silicon, and copper.

Figure 3.16b shows the enlarged (010) peak (cyan rectangle) from the sapphire substrate, and Figure 3.16c demonstrate the large area single crystalline film of Ga obtained at room temperature from the supercooled liquid. To understand the thermal behavior of the crystallized Ga, we performed differential scanning calorimetry (DSC) analysis for the crystallized Ga on different substrates. The analysis from DSC analysis results show the existence of a glassy structure with a glass transition ( $T_g$ ) at around 15 °C (Figure 3.17). Moreover, the solidification process on the substrates induces different modification of microstructures in the crystallized Ga droplet. The cooling curve of the DSC measurement of droplets obtained on different substrates shows different exothermic behavior, whereas the melting point is the same for all the droplets irrespective of the substrate material (Figure B.2, Appendix B). Detailed study on the influence of the oxide formation during crystallization is a future work. Scanning electron microscope (SEM) image of a fast-quenched droplet on silicon substrate shows a localized nanoscale spatial ordering in the freeze-fractured cross-section of the glassy structure (Figure B.3, Appendix B).

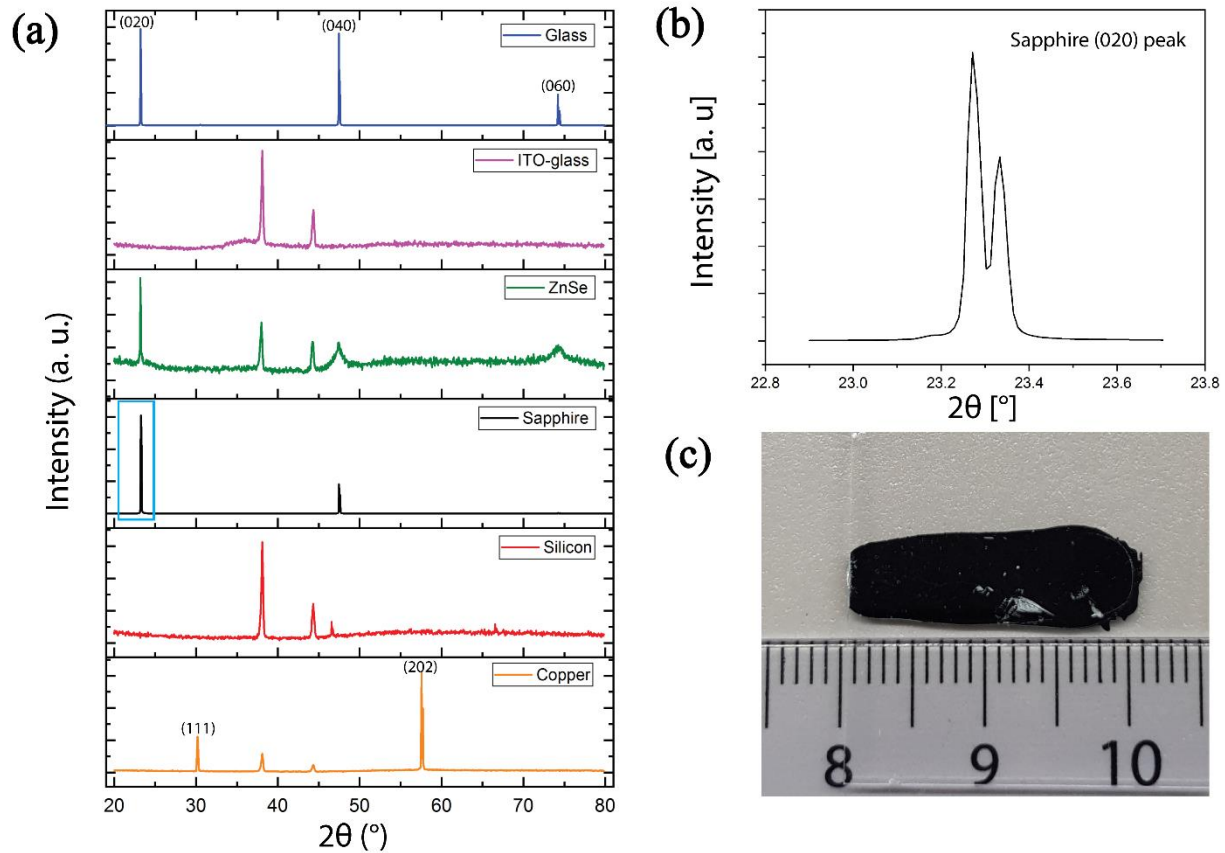


**Figure 3.16:** Structural characterization of the highly ordered Ga crystal. (a) X-ray diffraction (XRD) measurement of the crystallized Ga on different substrates.  $2\theta$  scan of highly ordered single-crystal Ga film. (b) Enlarged (010) peak of crystallized Ga on sapphire substrate (cyan rectangle). (c) Single crystalline Ga film of approximately  $120 \mu\text{m}$  thickness and  $0.5 \times 2 \text{ cm}^2$  square area.

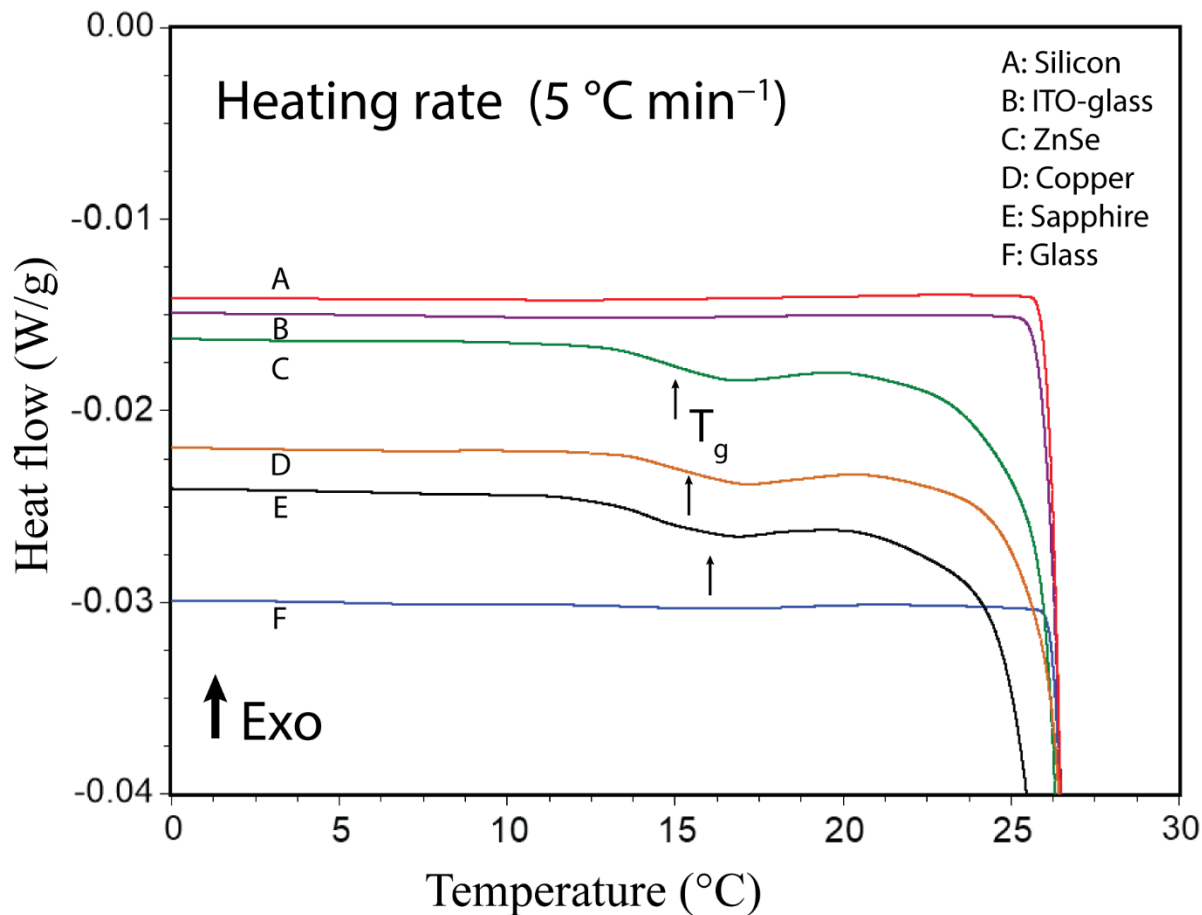


**Figure 3.17:** Differential scanning calorimetry (DSC) analysis of the crystallized Ga droplets on different substrates. The  $T_g$  curves are indicated with the small arrows.

### 3.4 Summary

The PC property of Ga could be a potential tool in designing a caloric capacitor that can store unused thermal energy to perform a useful work in dynamic electromechanical devices. The interface characteristics revealed will encourage better evaluation of energy efficient PC materials with a minimum phonon scattering and less power dissipation, and paves the way for surface induced single-crystal formation from supercooled liquids. This finding could validate the temperature dependence of surface layering in supercooled liquids.

# **4 Liquid Crystal Structure in Supercooled Liquid Gallium and Eutectic Gallium-Indium**

---

Reprint from reference [198]

Adv. Mater. 2021, 33, 38, 2104807

DOI: 10.1002/adma.202104807

©2021 The Authors. Published by WILEY-VCH Verlag GmbH & Co. KGaA, Weinheim

## 4.1 Introduction

Elemental Ga is a strange metal with mixed covalent and metallic bond property at ambient pressure and temperature [89]. Unlike any other simple liquid, supercooled liquid Ga is very complex liquid that exhibits both covalent and metallic character [42]. The outstanding ability of elemental Ga to form allotrope [83,85,199] and its low-melting temperature (29.8 °C) make it a good candidate as a nontoxic metallic material with high thermal and electrical conductivity [15]. In 1952, Frank hypothesized that an icosahedral short-range order should be energetically favorable in supercooled liquids consisting of atoms of roughly spherical symmetry [40,200].

For decades, the anomalous structural ordering in supercooled liquid Ga has garnered great attention in the scientific community. In previous attempts to describe the unusual property of liquid Ga, Tsay and Wang [201] reported on the tetrahedron of Ga consisting of two dimers interlocked – having four indices with 4-atoms. One of the nearest neighbor atoms has longer bond length compared to the rest of the neighbors, and therefore the tetrahedron is asymmetrical. In the case of the short-lived covalent Ga dimers, a bond length of near 2.44 Å was attributed to the structural shoulder observed from the molecular dynamic simulation [42]. However, a Ga-Ga pair separation of greater than 2.5 Å in a cluster structure is more likely to exist in the liquid [97]. Thus, a medium-range order of more than 20 Ga atoms are involved in the structural order in liquid Ga [202]. To unravel the origin of the structural order in liquid Ga, classical molecular dynamic simulation have been investigated [42,97,201–203]. Neutron and X-ray scattering experiments revealed a scattering shoulder of structural order in the liquid [4,43–45]. Several interpretations were proposed for the structural order in liquid Ga such as (i) short-lived dimeric bonding characteristic of the solid orthorhombic  $\alpha$ -Ga phase that persisted in the liquid state, or (ii) structures beyond short-range order – polyhedron clusters of 4 and 5 atom units [44,201,202]. Recent studies highlighted that the dimeric bonding characteristics of  $\alpha$ -Ga phase does not persist in the liquid state, whereas increasing fraction of five-fold symmetry and crystalline motifs exist in the liquid state [4,97,203]. In addition, X-ray analysis of liquid Ga droplet on diamond revealed the layering effect of Ga dimer ( $\text{Ga}_2$ ) molecules on hard substrate [183]. Recently, transmission electron microscope (TEM) analysis showed the thermally stable coexistence of liquid-solid phases in Ga and eutectic Gallium Indium (EGaIn) nanodroplets [8,9]. Both liquid Ga and EGaIn exhibit liquid-liquid phase transition behavior [85,103,104,204].

Hitherto, the long-standing debate on the origin of structural order in liquid Ga is still unsettled. In this study, we aim to shed light on the possible long-range order in supercooled liquid Ga sandwiched between various polymer-coated glass substrates by the use of reflective polarized optical microscopy (R-POM) utilized in liquid crystal (LC) research, differential scanning calorimetry (DSC) and SEM.

## 4.2 Experimental Section

### 4.2.1 Microscope and Light Spectroscopy Technique

A scanning electron microscope (**Zeiss Ultra 500 Gemini SEM, Carl Zeiss Inc., Oberkochen, Germany**) was used to characterize microstructure and morphology of Ga films. Prior to SEM examination, the films were quenched in liquid nitrogen. The freeze-fractured films were examined under SEM at -20 °C to prevent structural damage. 3D laser scanning microscope (Keyence VK-X200) was used for characterizing surface topology.

**Polarized light microscope (ZEISS Axio Imager.Z2, Carl Zeiss Inc., Oberkochen, Germany)** equipped with polarizers and rotating stage was used for optical observations and phase sequence determination of the liquid crystal phase.

**Linkam (THMS600) temperature controlled stage** mounted of ZEISS Axio Imager.Z2 enabled *in situ* thermal control of the sample and subsequent imaging during experiments. Precise cooling of sample was achieved via liquid nitrogen cooling through LNP96 cooling option.

**Spectroscopy technique** was performed using compact CCD spectrometer (Thorlabs) for wavelengths ranging from 200 to 1000nm. The device was integrated with a linear fiber bundles. Collimated broadband light was used to illuminate the sample in reflection mode.

#### 4.2.2 Liquid Crystal (LC) Cell Preparation and Electrical Characterization

To realize electro-optics in LC cell, coating polyimide (PI) within the inner glass surface of the cell was desired for surface anchoring. Pre-cleaned glass slides were spin-coated with 10 wt % solution of PI2555 (HD Microsystems) in 1-Methyl-2-pyrrolidone, anhydrous, 99.5% (Sigma Aldrich) for 5s at 800 rpm. Then followed by 45s at 5000 rpm and baked at 180 °C for 1 h. Different cell thickness between 10 and 50  $\mu\text{m}$  was maintained using polystyrene spacer particles (Cospheric LLC). The supercooled liquid Ga (with shelf life of more than 6 months) was then assembled by shearing between the two PI coated glasses (Figure 4.1). To induce planar alignment with PMMA plates (2 mm-thick), the surfaces were rubbed with velvet cloth. Electro-optics actuation with DC voltage (DC power supply, KEYSIGTH U80001A) of 18 V was applied across 10  $\mu\text{m}$ -thick film. For AC actuation, function generator (Tektronix AFG3102C) combined with a high frequency power amplifier (TREK MODEL 2100HF) to deliver 18 V using square or sine wave function. A mixed channel oscilloscope (Tektronix) device monitored the frequency response of the actuation signal. Resistance characterization was performed using KEYSIGTH ENA Network Analyzer (5Hz – 3GHz).

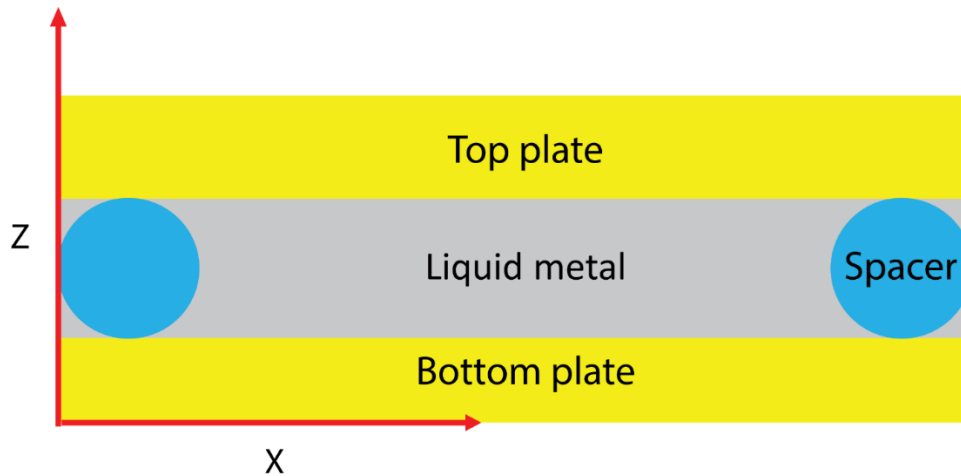


**Figure 4.1:** Illustration of the LC cell assembly for optical study of liquid Ga.

## 4.3 Results and Discussion

### 4.3.1 Thermal Analysis and Hidden Optical Activity in Supercooled Ga

Differential scanning calorimetry (DSC) of Ga shows the first order transitions upon heating and cooling. On heating from -80 °C to 150 °C at 2 °C/min, the pure Ga melts to pseudo-isotropic liquid phase at around 30 °C (Figure 4.2). During cooling, the liquid crystallized to  $\alpha$ -Ga at -51 °C because of the supercooling effect of Ga. Although Ga is a polymorphic metal, only the peak that corresponds to the orthorhombic  $\alpha$ -Ga phase was detected in DSC. Other metastable polymorphs of Ga crystal are  $\beta$ -Ga,  $\gamma$ -Ga, and  $\delta$ -Ga, which are monoclinic, orthorhombic and tetragonal, respectively [83,85]. Interestingly, these polymorphs can be detected in the DSC curve of the EGaIn alloy, which is a low melting point eutectic liquid (Table 4.1 and Figure C.1, Appendix C) [205,206]. Moreover, DSC experiments performed at much higher temperature (400 °C) did not reveal any phase transition peak.

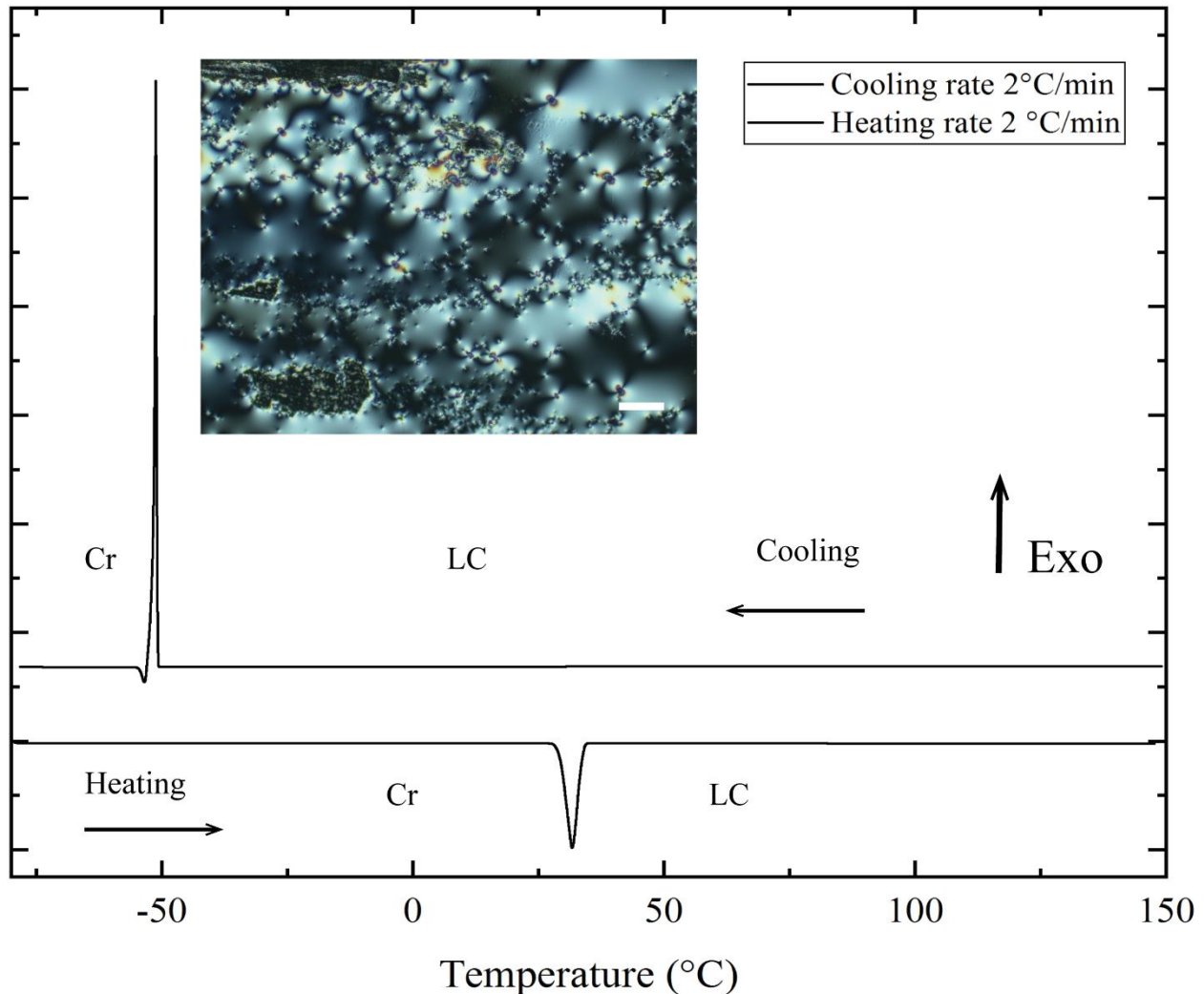


**Figure 4.2:** Differential scanning calorimetry analysis of Ga upon heating and cooling. The pseudo-isotropic liquid appears above the melting point (30 °C) of  $\alpha$ -Ga crystal during heating. The liquid recrystallized at -51 °C indicating the stability of the supercooled state. The inset image represents R-POM texture of the LC phase in supercooled Ga similar to the Schlieren textures of nematic or smectic-A (SmA) liquid crystals with homeotropic alignment. Scale bar is 200  $\mu\text{m}$ .

In a thin layer of the supercooled liquid Ga prepared on a glass substrate at room temperature (RT) with open-air boundary, a grayish texture is observed using circularly polarized light in R-POM (Figure 4.2 inset). The fact that the reflected light is not extinguished between the crossed polarizers means anisotropic reflection at the Ga-substrate interface. The texture resembles to Schlieren textures of various liquid crystal phases subjected to homeotropic boundary condition (boundary layer tends to align the LC director normal to the substrate) [207]. There are only two brush defects seen, which means the presence of only 1/2 strength defects. In Liquid

crystals such textures may be due to pretilt of the elongated building blocks, or may indicate biaxial nematic or smectic phase [208,209]. Note that the open-air surface of the liquid may be covered with an oxide layer of about 3-nm. This highly transparent oxide layer occurs naturally when exposed the liquid to open ambient air [123,210]. This may cause some pretilt at the air-Ga interface, but otherwise the optical property of the thin liquid Ga is unaffected due to the optical transparency of the oxide[210,211].

**Table 4.1:** Phase transition enthalpies taken from DSC analysis at 2 °C/min heating and cooling rate.

Material	Phase transition	T [°C] ( $\Delta H$ [ $Jg^{-1}$ ]) Heating cycle	T [°C] ( $\Delta H$ [ $Jg^{-1}$ ]) Cooling cycle
Ga	Cr—LC	+31.71 (79.78)	-51.21 (136.91)
EGaIn	Cr <sub>1</sub> —Cr <sub>2</sub>	-23.07 (12.22)	-32.17 (12.72)
	Cr <sub>2</sub> —Cr <sub>3</sub>	-11.87 (37.47)	-27.16 (25.76)
	Cr <sub>3</sub> —LC	+19.61 (3.11)	+17.67 (1.70)

Cr; crystal phase 1, 2, and 3 represent different polymorphs of Ga.

### 4.3.2 Polarization Optical Microscopy (POM) Investigation

R-POM observations in the supercooled liquid Ga was also carried out in cells where the material was sandwiched between two glass plates coated with polymer layers that provide either planar or homeotropic alignment for liquid crystals at RT (22 °C). For instance, a planar alignment where the director is parallel to the substrates, was achieved by confining the liquid in between two rubbed poly(methyl methacrylate) (PMMA) plates separated by a gap ranging from 5 to 50  $\mu\text{m}$  at 22 °C.

In Figure 4.3, the planar condition of the supercooled liquid Ga in the PMMA cell with 40- $\mu\text{m}$  separation is illustrated. An R-POM image of the liquid Ga film without analyzer with the rubbing and the shear flow direction initially pointed at  $45^\circ$  with respect to the polarizer by the red double-head arrow (Figure 4.3a). The crossed-polarized optical image of the cell appeared bright since the molecular optical axis is at  $45^\circ$  with respect to the two polarizers in agreement with the shear flow direction (Figure 4.3b). The dark area in Figure 4.3b is PMMA plate. However, the crossed-polarized optical image of the cell appeared dark when rotated the sample to  $45^\circ$  with reference to either one of the polarizers, and the optical long axis aligned with one of the polarizers, the sample is extinguished (Figure 4.3c). The PMMA surface shows a strong planar anchoring of the liquid Ga molecule.

POM textures were also studied in sandwich cells, where in one of the substrates in microchannel (15  $\mu\text{m}$  width, 55  $\mu\text{m}$  period, and 17  $\mu\text{m}$  depth) were made of polydimethylsiloxane (PDMS) prepared at room temperature (Figure C.2, Appendix C). The channels infiltrated with EGaIn liquid at 22  $^\circ\text{C}$  immediately show planar alignment that after 2 hours show parabolic focal conics (PFC) type domains [212] with long axis of elongated parabolas pointing perpendicular to the channel walls (Figure C.3, Appendix C). Note that the images in Figure C.2 and C.3 were obtained in transmission POM. Such kind of parabolic focal conic (PFC) defects are well-known in liquid crystals with either smectic layers of smectic LCs or pseudo-layered structures of chiral nematic or the twist-bend nematic phases. PFC appears when either the layer spacing decreases, for example, on cooling or when the films are dilated [213]. PFC defects have also been observed in the helical nanofilament phase of bent-core LC molecules near the glass interface when quenched to RT [214,215]. These observations indicate the presence of some kind of true or pseudo-layer structure of the supercooled liquid Ga. The direction of the PFC domains also indicates that the layers are parallel to the channel wall. This is due to the shear alignment that allows flow only along the channel wall and the smectic layers [216].

In a 17  $\mu\text{m}$  thick cell where the substrates were treated by a polyimide that usually promotes homeotropic alignment (director perpendicular to the substrate) for thermotropic liquid crystals, Ga filled cell appears dark in R-POM with crossed polarizers even when the sample was rotated  $45^\circ$  with respect to the polarizers (Figure 4.3e,f). Pseudo-isotropic textures are usually observed for nematic and smectic-A (SmA) LC phases between homeotropic anchoring surfaces.

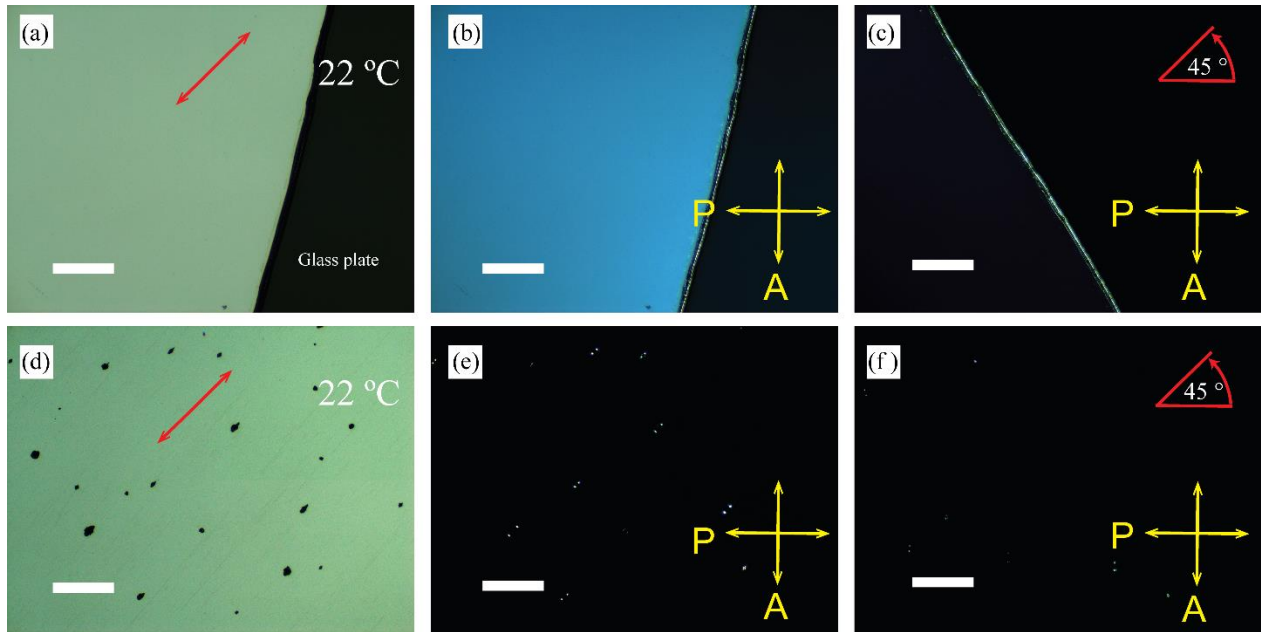


**Figure 4.3:** Reflection polarized optical microscope (R-POM) images of liquid Ga cell confinement. R-POM images of a planar and homeotropic texture taken at 22 °C without analyzer (a) and (d), with crossed polarized (b) and (e), and sample rotated 45° with respect to the polarizers (c) and (f). Note that the red arrows represent the flow directions. The sample stage was initially placed at 45° so that the shear flow direction is at 45° with respect to the polarizers. The thickness of planar and homeotropic cells are 40  $\mu\text{m}$  and 17  $\mu\text{m}$ , respectively. Scale bars: (a) – (f) 200  $\mu\text{m}$ .

For untreated glass cell, the formation of focal conic defect (FCD) was observed in the sandwiched film of liquid Ga at the clean glass boundary (Figure 4.4). The formation of focal conic domains is a characteristic of orthogonal SmA liquid crystal and has been observed in helical nanofilaments phase due to unwinding of the helical structure near the glass surface as the twisted conformation of the HNF cannot completely fill the space on the flat glass surface [214].

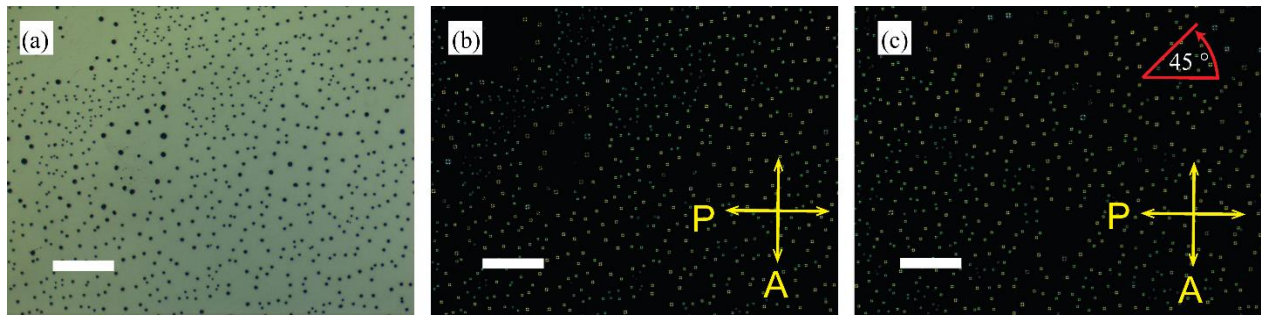


**Figure 4.4:** Focal conic defects in untreated glass with 10  $\mu\text{m}$  cell thickness. R-POM images without analyzer (a), crossed-polarized (b), and ample rotated  $45^\circ$  with respect to the polarizers (c). The R-POM observation was conducted at  $22^\circ\text{C}$ . Scale bars are  $100\ \mu\text{m}$ .

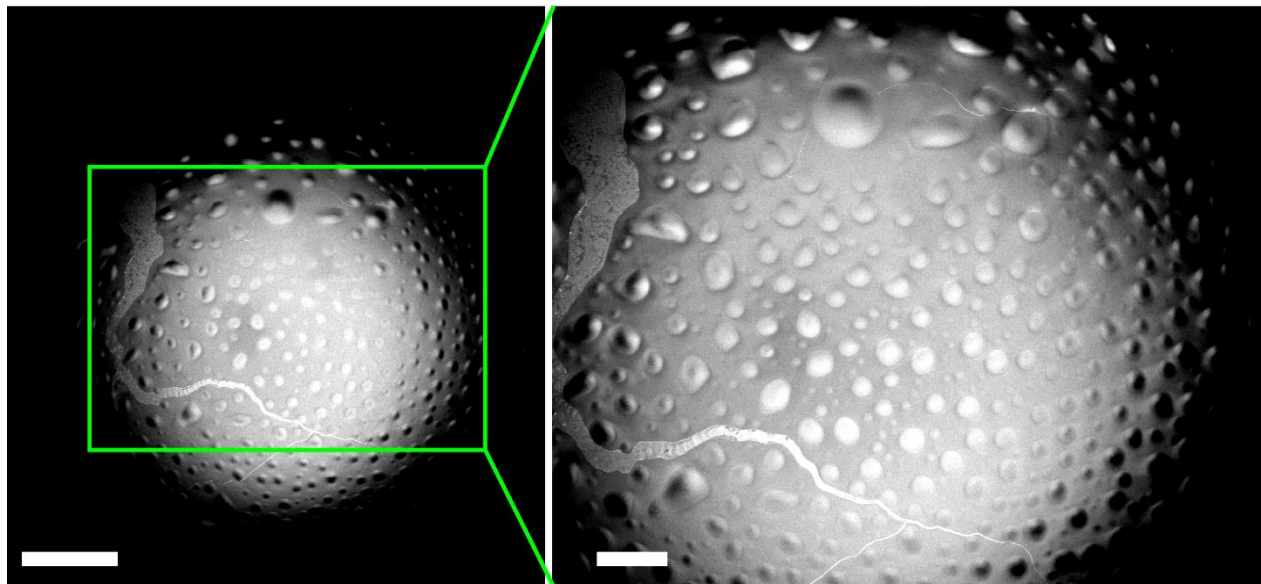


**Figure 4.5:** SEM micrographs of liquid Ga droplet. The surface of droplets was cleaned in 0.5 M HCl solution to remove any oxide before SEM imaging. The SEM of the liquid Ga droplet shows structures similar to focal conic of smectic droplets. Scale bars: (a)  $100\ \mu\text{m}$ , and (b)  $40\ \mu\text{m}$ . Droplet size is around  $600\ \mu\text{m}$ .

In addition, focal conic texture that is very similar to smectic droplet appeared on the liquid Ga droplet characterized using scanning electron microscope (SEM) (Figures 4.5). Detailed experiments on the surface stabilized smectic-like phase revealed a parabolic focal conic-like texture resembling that of a dilated SmA (Figure 4.6) [213].

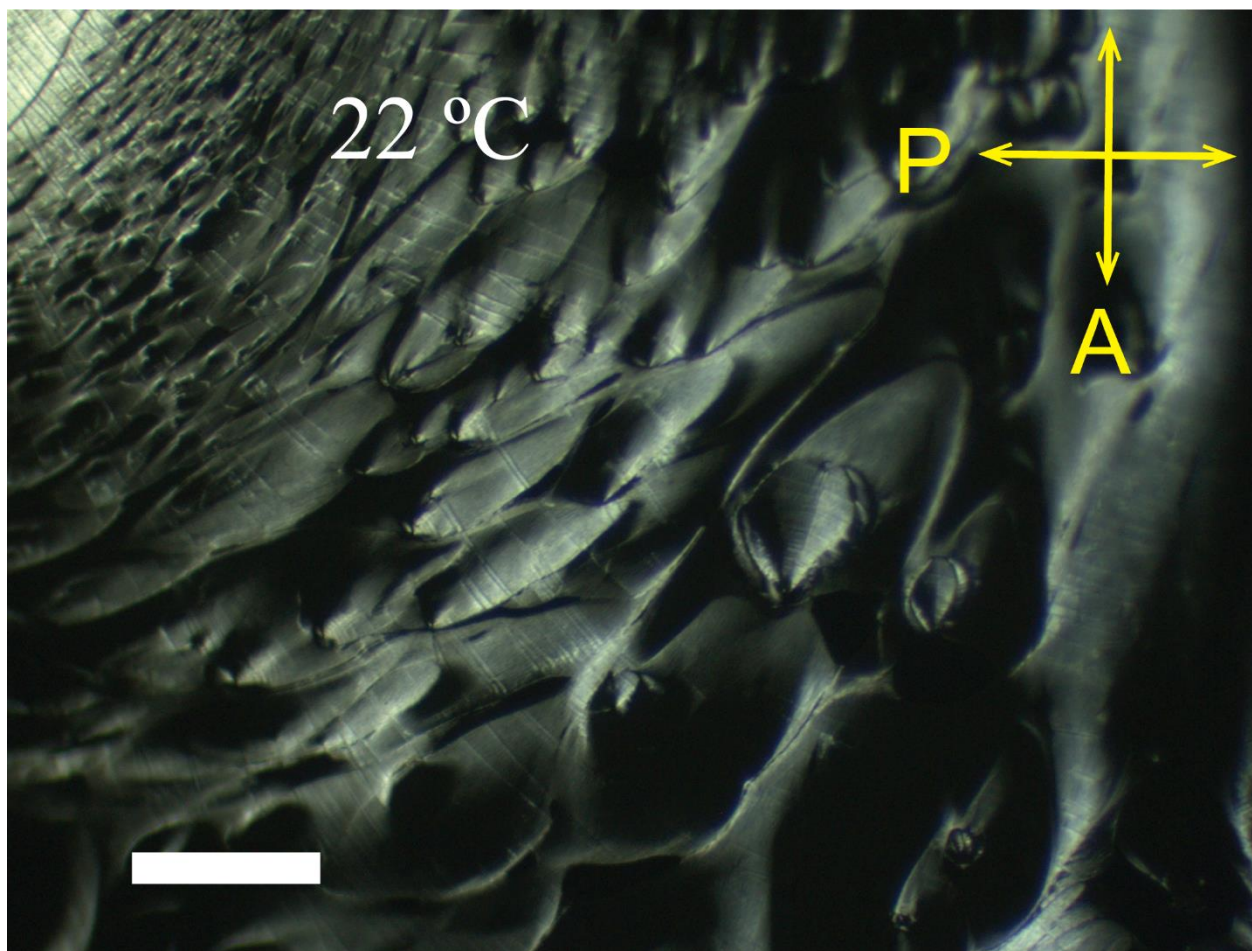


**Figure 4.6:** Parabolic focal conic defect-like texture of dilated SmA or nematic texture in an unknown cell thickness. Scale bar is 100  $\mu\text{m}$ .

### 4.3.3 Thermotropic Behavior, Order Parameter, and Microstructure

In order to investigate the thermotropic property of the LC structure phase in liquid Ga, a planar cell with a 50- $\mu\text{m}$  thickness was subjected to slow heating/cooling at 2  $^{\circ}\text{C}/\text{min}$  (Figure 4.7a). The optical texture was monitored with R-POM and the high temperature phases were studied. Several observations were noted while heating the cell starting from RT. The long molecular axis of the sample and the flow direction were oriented at 45 $^{\circ}$  with respect to the polarizers. In such position, the intensity of the cell gradually decreased with increasing temperature (Figure 4.7b). At temperature range between 120 and 130  $^{\circ}\text{C}$ , the cell became completely dark (Figure 4.7c).

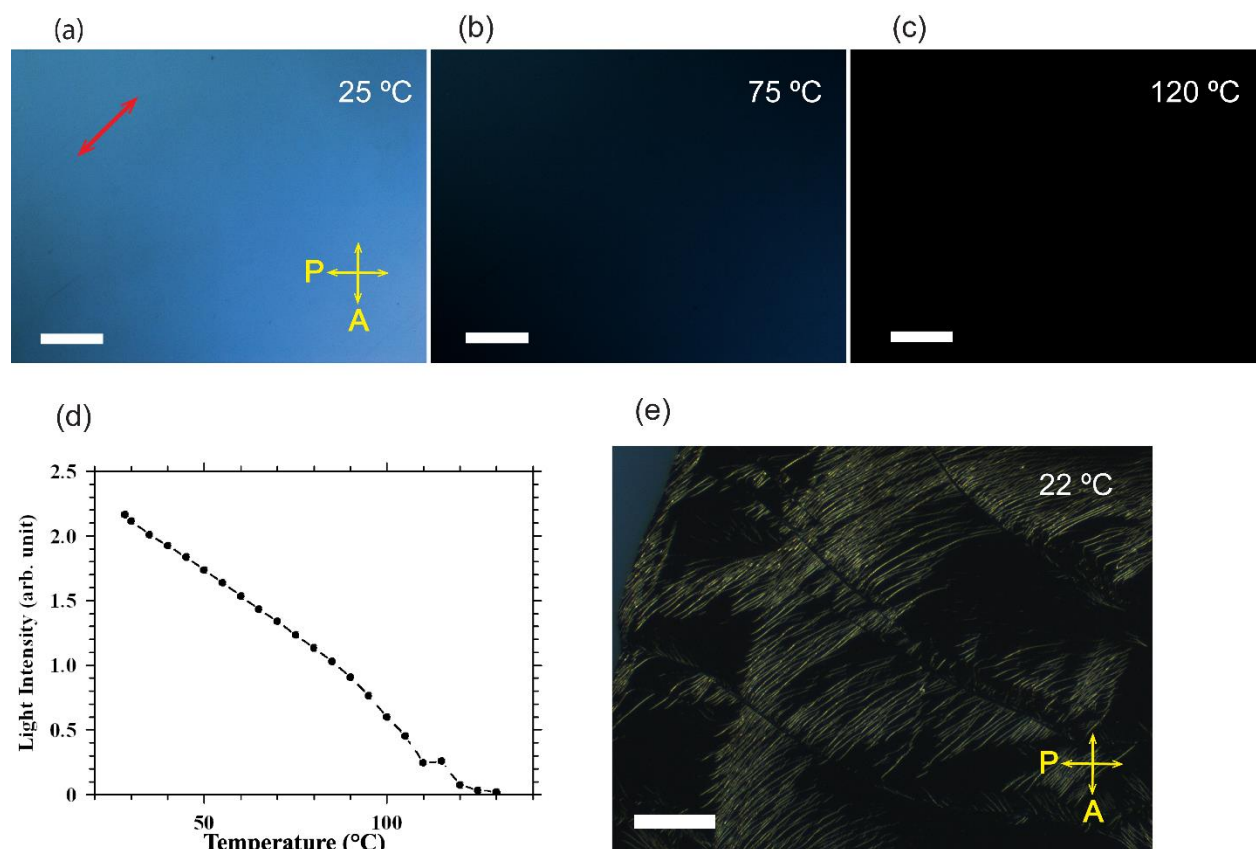


**Figure 4.7:** Thermotropic LC structure behavior of supercooled liquid Ga. (a), (b), and (c) Temperature dependence of anisotropic LC structure in planar orientation revealed in R-POM. The bright state disappeared at high temperature because of realignment of the molecular optical long axis with the polarizers. (d) Reflectance intensity measurement of the planar geometry with respect to temperature change. At 120 °C, the intensity decreased almost to zero. (e) Stripes texture obtained from high temperature above 120 °C. Scale bars: (a) – (c) 100  $\mu\text{m}$ , (e) 100  $\mu\text{m}$ .

By further heating, isotropic domains started to appear up to 145 °C. The anisotropic reflection intensity of liquid Ga upon temperature variation decreases to almost zero at 120 °C in a planar cell with 10- $\mu\text{m}$  film thickness (Figure 4.7d). Interestingly, crystalline strands were observed around birefringence bubble during isotropic transition at around 145 °C (Figure 4.7e). The strands elongate near the bubble, which shows needle-like domains that nucleates at a defect area. The R-POM image in Figure 4.7e was taken at 22 °C after slowly cooling the Ga film to RT. The stripe texture looks like that of TGBA\* or SmA phase subjected to homeotropic boundary condition [207].

It is important to know that the spatially confined supercooled liquid Ga is very stable at RT and beyond (Figure C.4, Appendix C). The liquid can withstand extreme temperature value down to  $-84\text{ }^{\circ}\text{C}$  before crystallizing. The sandwiched Ga between the substrates does not crystallize at all at RT, except at its crystallization temperature. The upper working temperature limit is above  $130\text{ }^{\circ}\text{C}$  prior to the formation of isotropic domain. The proposed phase sequence of the Ga obtained from the R-POM observation differs from the phase transitions analysis conducted with the DSC measurement. We proposed a molecular arrangement of the predicted orthogonal smectic phase with the phase sequence of the LC mesophases in supercooled liquid Ga based on R-POM observations in Figure 4.8. Note that the molecular structure of Ga mesophase could possibly composed of clusters with variable shapes such as oblate or prolate spheroid [217,218]. Therefore, the model below is purposely for visualization and may not be accurate.

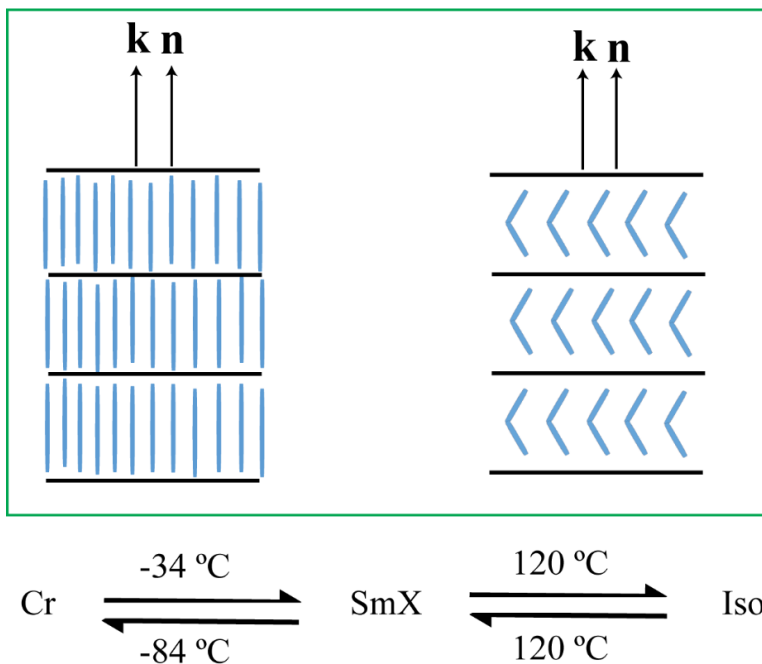


**Figure 4.8:** An illustration of the possible molecular or cluster arrangement that give rise to the orthogonal liquid crystal properties in the structure of supercooled Ga.

SEM images of slowly quenched planar aligned sample shows stripe structures from the confined liquid Ga cell. The width ( $w$ ) of the stripes is 40 nm according to the SEM observation (Figure 4.9).

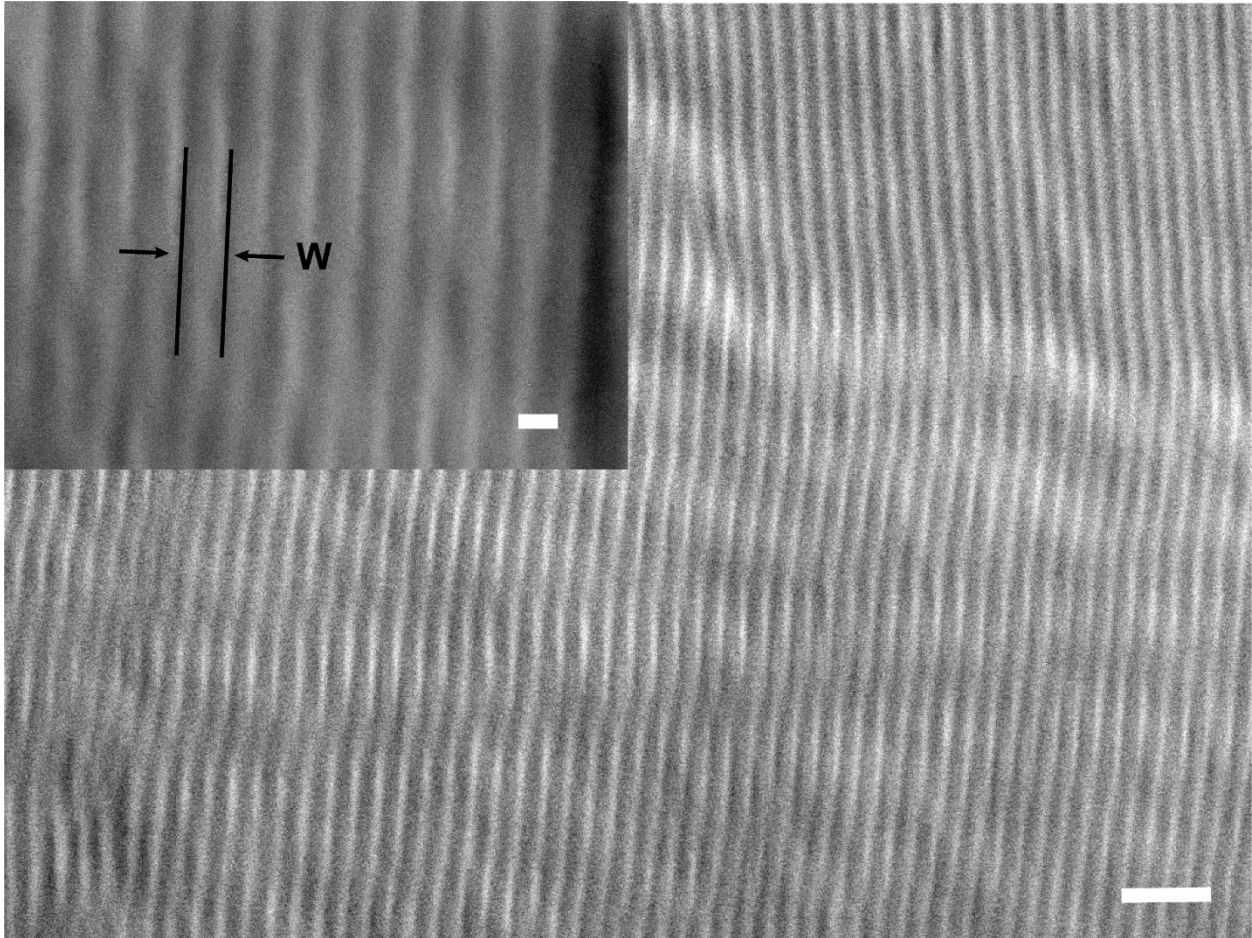


**Figure 4.9:** SEM images of stripes in homeotropic anchoring condition at a glass boundary. The width of the structures is ca. 40 nm measured from the SEM images. Scale bars: 200 nm and 40 nm (inset).

SEM images of the needle-like structure around birefringent bubbles clearly show spatial arrangement of nanostructures with size that ranges from hundreds of nanometers to 2.5  $\mu\text{m}$  (Figure 4.10a,b). To prepare the glassy Ga samples, the samples were plunged into liquid nitrogen prior to the SEM observation. The images were taken at  $-20\text{ }^{\circ}\text{C}$  to prevent any structural reorganization and damage by the electron beam during SEM characterization. It is worth to mention that glass transition of Ga metal was reported previously in a slowly quenched Ga film, which reassured the molecular behavior of the liquid phase [47].

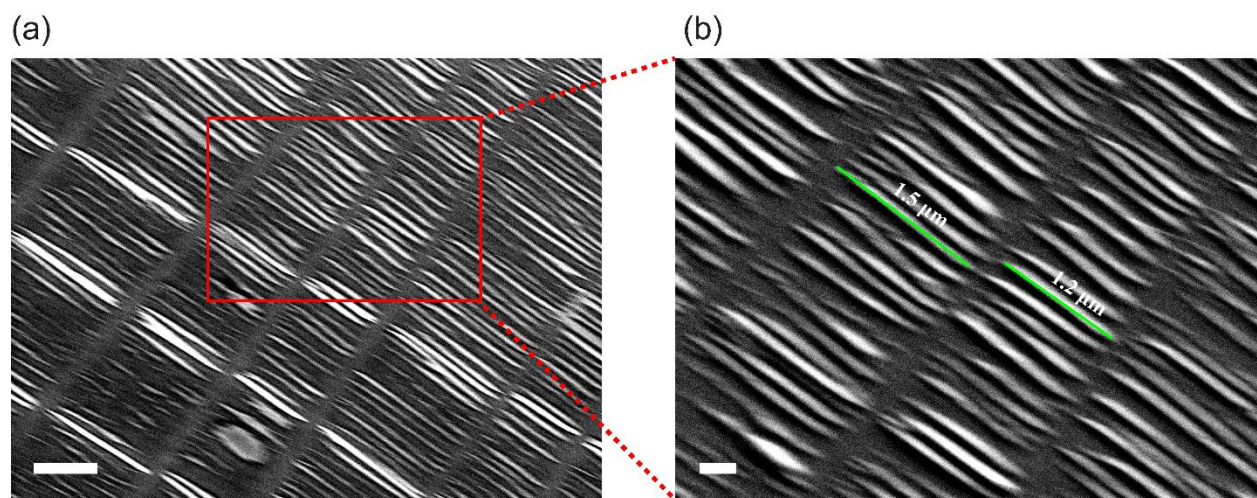


**Figure 4.10:** Scanning electron microscope of needle-like texture of of nanocrystals around liquid Ga. The texture was stabilized at RT prior to SEM imaging. Scale bars: (a) 1  $\mu\text{m}$ , and (b) 300 nm.

During retraction of the contact line of liquid Ga sandwiched between clean glass and PDMS, Bouligand arcs-like formation with bimodal (two-pitch) arced patterns were visualized with R-POM at RT (Figures 4.11a,b) [219]. Bouligand arcs are inherent property of chiral biological LC material such as chromosome, cholesteric fiber, and insect's exoskeleton [220–222]. The arcs show a series of bow-shaped fibers (arced or parabolic patterns) of regular stratification corresponding to the half-helical pitch  $h$ . The arcs indicate the characteristics of chiral LC obtained via an oblique sectioning.

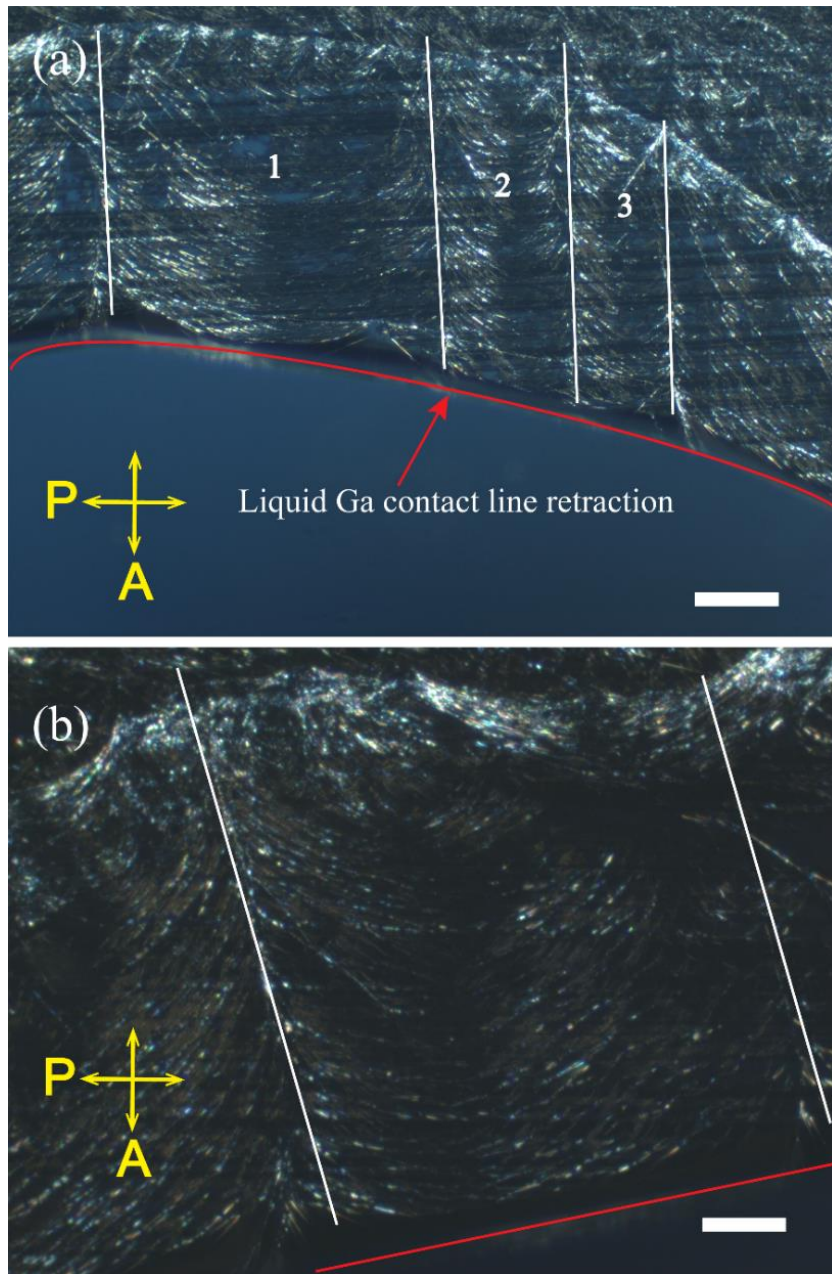


**Figure 4.11:** Bouligand arcs-like formation in supercooled liquid Ga on glass surface. Bouligand arcs were observed in liquid Ga on glass surface by the retraction of contact line of the liquid, which made an oblique angle with the glass surface. (a) Stretched arced patterns showing the bimodal pitch behavior of the liquid in the regions labelled 1, 2, and 3. The red line represents the retracting fluid front. (b) A large stretched arc with a clear bow-shape pattern. The bow-shape of Bouligand arcs seem to have originated from a liquid with pitch variation. The glass used here is untreated. Images were taken at 22 °C. Scale bars are 100  $\mu\text{m}$ .

#### 4.3.4 Electro-Optics

Counterintuitively, the molecular-cluster behavior of LC-Ga enabled electro-optics switching where birefringent state is induced via the application of low electric field (DC) of  $1.8 \text{ V}/\mu\text{m}$  at RT in a confinement between two ITO-glass separated by  $10 \mu\text{m}$  as shown in Figure 4.12a,b. The homeotropic ITO cell was obtained by polyimide (PI) coating. In addition, the electro-optics switching was realized by applying square wave AC field of  $1.9 \text{ V}/\mu\text{m}$  at 1 Hz across the cell. The reflected light intensity increased with the strength of the applied field as can be seen in Figure 4.12c. The corresponding current across the cell is linearly dependent on the applied potential field mas shown in Figure 4.12d.

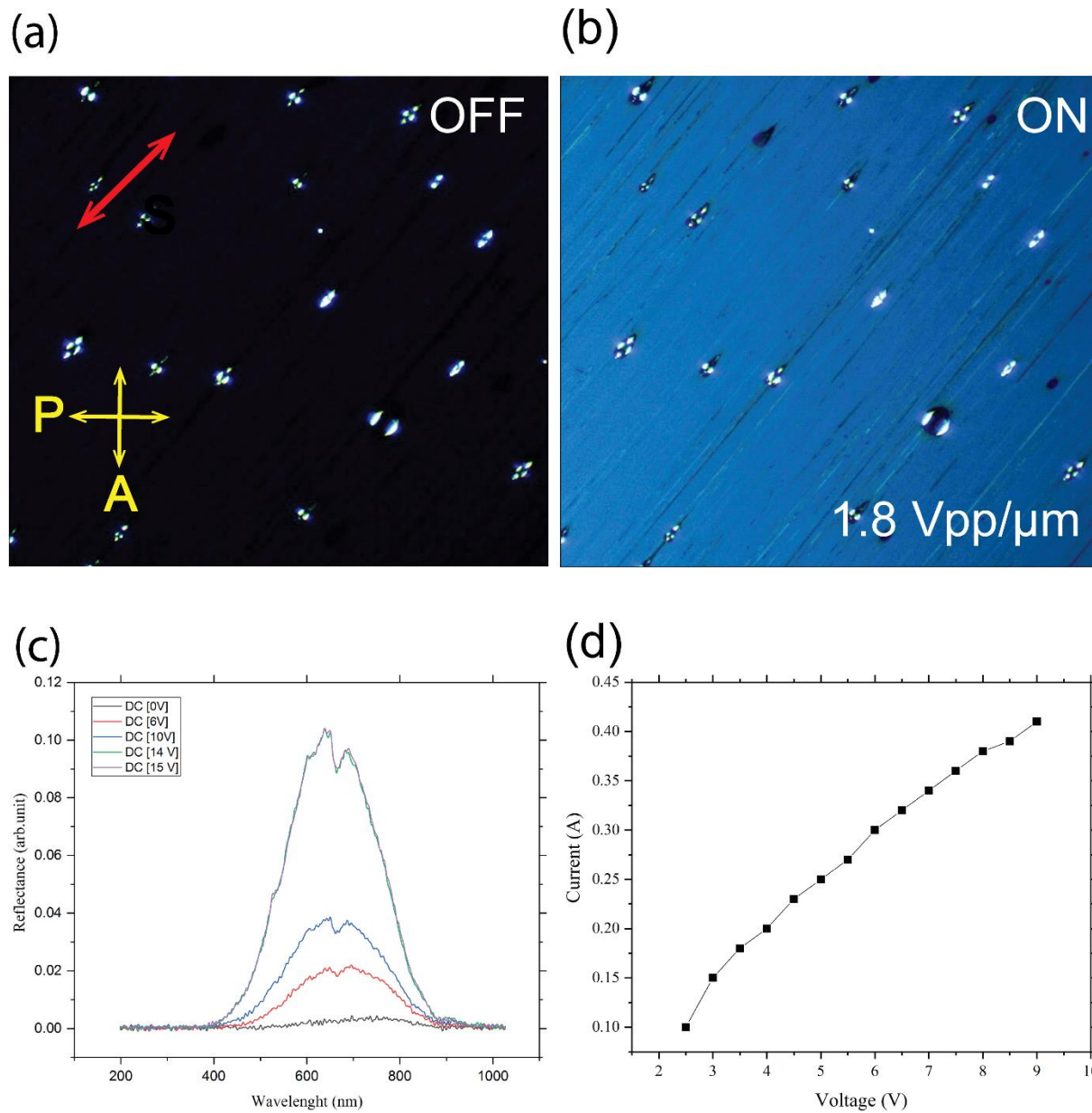


**Figure 4.12:** Electro-optics and electrical characterization of LC structure of liquid Ga. (a), (b) Electro-optics switching at RT with DC field in a 10- $\mu\text{m}$  polyimide-treated cell. (c) Reflectance intensity dependence on increasing switching voltage using DC field. The reflection intensity covers a broadband wavelength from 400 to 900 nm. (d) Almost linear dependent of current on the applied voltage across the cell.

Because of the high electrical conductivity of liquid Ga, the applied DC field across the cell generated heat in the liquid via possible joule heating and thus the temperature of the cell rises to around 50 °C. The temperature within the cell is uniform due to high thermal conductivity of liquid Ga. During this localized heating, there is less thermal dissipation through the bulk glass plates. The consequences of the electro-thermal effect was scrutinized further. At relative temperature above ambient condition, the electro-optic effect was not affected. However, above 130 °C, the electric field dependence of the birefringence vanished. The temperature dependent behavior of resistance across liquid Ga cell was characterized in PI treated cell with 17- $\mu\text{m}$  film thickness. The resistance of the liquid Ga decreased with temperature rise from 20 to 140 °C Figure 4.13a. Moreover, frequency response of the resistance was recorded from 100 kHz to 1 MHz. In Figure 4.13b, temperature dependent resistance at 100 kHz is plotted with varying temperature during cooling. Even though the resistance of Ga is low relative to conventional LC materials, such temperature dependent of the resistance could be attributed to polar behavior, which is typical for dielectric LC materials.

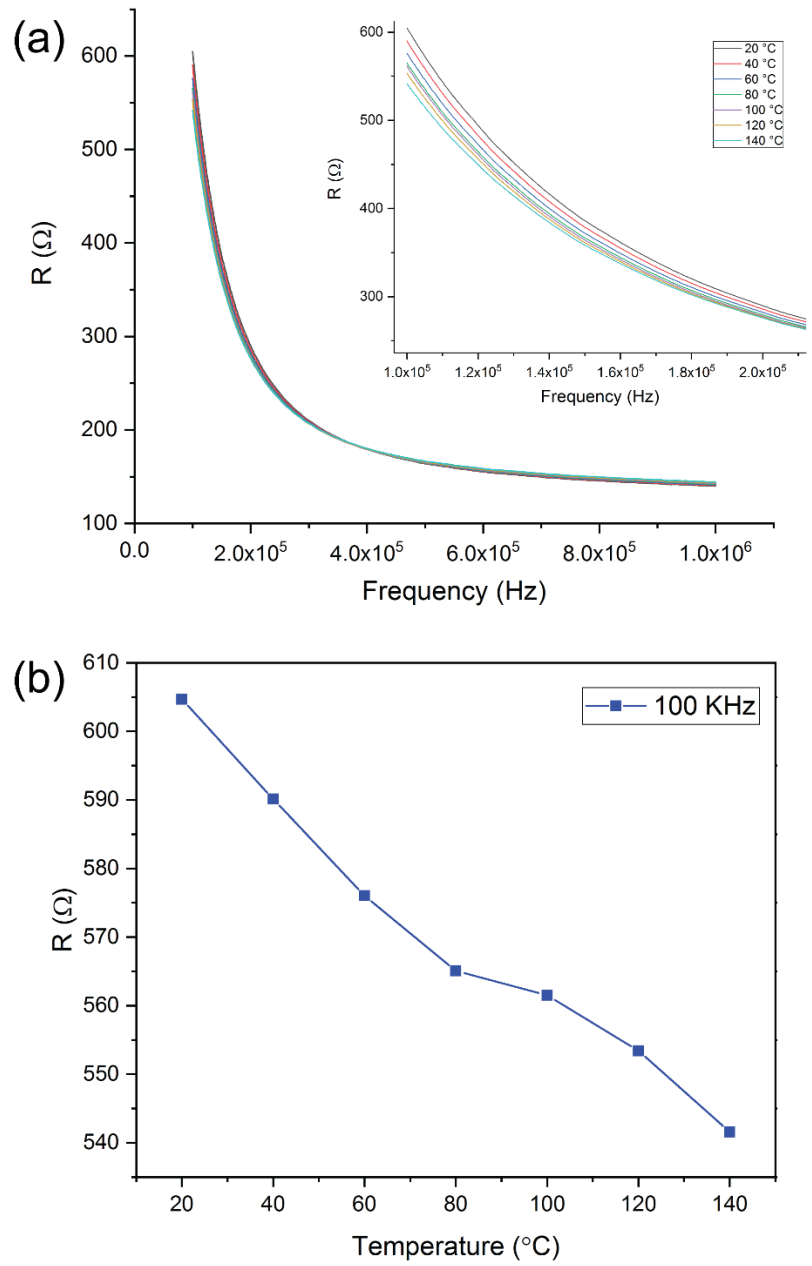


**Figure 4.13:** (a) Temperature dependent of resistance in Ga LC cell with film thickness of  $17 \mu\text{m}$ . (b) Resistance-temperature plotted at 100 kHz across the cell during cooling.

## **4.4 Summary**

In this work, we unraveled the attribute of liquid crystal structure in Ga by adopting approaches utilized in the liquid crystal research. We use reflection polarized optical microscope, surface treatment, and thermal analysis to study properties of supercooled liquid Ga and EGaIn that has evaded scientists for decades. The revealed optical characteristics of liquid metal could open up a new avenue of research activity in understanding the behavior of liquid metals, which are gaining potential in the soft electronic and sensors for future robotics. In addition, this study could help explain the unusual cluster formations in liquid Ga and can pave the way for a development of new physics to explain the ubiquitous anomalous behavior of metallic liquids.



# 5 Conclusion and Future Work

## 5.1 Conclusion

In conclusion, fundamental properties of supercooled liquid Ga have been discussed in this dissertation. Three different contributions pertaining liquid Ga are discussed: 1) wrinkling instability and adhesion of supercooled liquid Ga under uniaxial loading condition, 2) thermal effects on the crystallization kinetics of supercooled liquid Ga, and 3) liquid crystal structure in supercooled liquid Ga and GaIn. Different experimental approaches were incorporated to achieve the objectives of this dissertation. The main findings and contributions are stated below.

### 5.1.1 Winkling instability and adhesion of the oxide nanofilm skin of liquid metals

- Characterized the wrinkling instability that emerged at the interface between liquid metal and glass substrate through circular to radial wrinkle transition under axisymmetric loading.
- Mechanical attributes of the oxide skin enabled high surface conformation and exhibiting liquid-like behavior.
- Adhesion force and interface energy characterization.
- Insight on the rupturing mechanism of the compressed liquid Ga droplet and surface tension analyses.

### 5.1.2 Thermal effect and crystallization kinetics of supercooled liquid Ga

- Interfacial temperature effect on crystallization
- Thermo-mechanic influence on adhesive strength
- Extended large area oriented growth of crystal on dielectric glass
- Heat dissipation mechanism on different substrates
- Microstructure analysis of crystallized droplets
- Glass transition determination by differential scanning calorimetry in elemental metallic material.

### 5.1.3 Liquid crystal structure of the supercooled liquid Ga

- Understanding structural origin in liquid Ga.
- The utilization of reflective light microscope to probe liquid crystal order in metallic liquid.
- Thermotropic behavior with onset of anisotropic reflection from 120 °C up to room temperature.
- Stable liquid crystal phase observation in supercooled liquid Ga and EGaIn.
- Realization of planar and homeotropic alignment in liquid metal.
- Revealed the existence of lamellar texture corresponding to smectic liquid crystal phase.

## 5.2 Future Work

The work presented in this dissertation may mark the beginning of a new research activity in the domain of materials science and liquid crystal research. There are certain aspects that specifically required further scrutiny. Some of our suggestions for further study of the works are listed below:

- The role of substrate and thermal conductivity on the interfacial wetting during crystallization is complex, where the need for further analytical tool to *in situ* observe the mechanism at the interface is required. During crystallization, there is competition between thermal stress and adhesive stress that determine the fate of the gallium droplet. Therefore, droplets on the substrate either stick or peel-off. To investigate such effect correctly, one need to develop an imaging technique and analytical tool to model the deformation of the

droplet at  $t$  the onset of crystallization. A mean of external actuation such as vibration to induce crystallization will offer robust control on the supercooling. A seed material that is compatible with the crystalline structure of Ga can also offer suitable approach in order to avoid melting of the parent Ga seed.

- For the unprecedented LC structure in Ga and EGaIn, the anisotropic behavior in the liquid awaits to be explored. Due to the metallic and covalent nature of the liquid Ga, it is possible to characterize its dielectric properties. The extent of the LC stability investigated in this work is up to 74 hours. Further stability experiment and thermal relaxation over long period is recommended.

# Bibliography

1. de Boisbaudran L. 1875 On the chemical and spectroscopic characters of a new metal (gallium). *London, Edinburgh, Dublin Philos. Mag. J. Sci.* (doi:10.1080/14786447508641312)
2. de Boisbaudran L. 1876 On the physical properties of gallium. *London, Edinburgh, Dublin Philos. Mag. J. Sci.* (doi:10.1080/14786447608639126)
3. Moskalyk RR. 2003 Gallium: The backbone of the electronics industry. *Miner. Eng.* (doi:10.1016/j.mineng.2003.08.003)
4. Drewitt JWE, Turci F, Heinen BJ, Macleod SG, Qin F, Kleppe AK, Lord OT. 2020 Structural Ordering in Liquid Gallium under Extreme Conditions. *Phys. Rev. Lett.* **124**, 145501. (doi:10.1103/PhysRevLett.124.145501)
5. Kochat V *et al.* 2018 Atomically thin gallium layers from solid-melt exfoliation. *Sci. Adv.* (doi:10.1126/sciadv.1701373)
6. Daeneke T, Khoshmanesh K, Mahmood N, De Castro IA, Esrafilzadeh D, Barrow SJ, Dickey MD, Kalantar-Zadeh K. 2018 Liquid metals: Fundamentals and applications in chemistry. *Chem. Soc. Rev.* (doi:10.1039/c7cs00043j)
7. Kalantar-Zadeh K *et al.* 2019 Emergence of Liquid Metals in Nanotechnology. *ACS Nano.* (doi:10.1021/acsnano.9b04843)
8. Losurdo M, Suvorova A, Rubanov S, Hingerl K, Brown AS. 2016 Thermally stable coexistence of liquid and solid phases in gallium nanoparticles. *Nat. Mater.* **15**, 995–1002. (doi:10.1038/nmat4705)
9. Tang SY *et al.* 2019 Phase Separation in Liquid Metal Nanoparticles. *Matter* **1**, 192–204. (doi:10.1016/j.matt.2019.03.001)
10. Chen S, Wang HZ, Zhao RQ, Rao W, Liu J. 2020 Liquid Metal Composites. *Matter.* (doi:10.1016/j.matt.2020.03.016)

11. Zavabeti A *et al.* 2017 A liquid metal reaction environment for the room-temperature synthesis of atomically thin metal oxides. *Science* (80-. ). **358**, 332–335.  
(doi:10.1126/science.aao4249)
12. Hu L, Wang L, Ding Y, Zhan S, Liu J. 2016 Manipulation of Liquid Metals on a Graphite Surface. *Adv. Mater.* (doi:10.1002/adma.201601639)
13. Chacko S, Joshi K, Kanhere DG, Blundell SA. 2004 Why do gallium clusters have a higher melting point than the bulk? *Phys. Rev. Lett.* (doi:10.1103/PhysRevLett.92.135506)
14. Duggin MJ. 1969 The thermal conductivity of liquid gallium. *Phys. Lett. A*  
(doi:10.1016/0375-9601(69)90528-3)
15. Dodd C. 1950 The electrical resistance of liquid gallium in the neighbourhood of its melting point. *Proc. Phys. Soc. Sect. B* (doi:10.1088/0370-1301/63/9/303)
16. Yu S, Kaviany M. 2014 Electrical, thermal, and species transport properties of liquid eutectic Ga-In and Ga-In-Sn from first principles. *J. Chem. Phys.* (doi:10.1063/1.4865105)
17. Markvicka EJ, Bartlett MD, Huang X, Majidi C. 2018 An autonomously electrically self-healing liquid metal-elastomer composite for robust soft-matter robotics and electronics. *Nat. Mater.* (doi:10.1038/s41563-018-0084-7)
18. Jin Y, Lin Y, Kiani A, Joshipura ID, Ge M, Dickey MD. 2019 Materials tactile logic via innervated soft thermochromic elastomers. *Nat. Commun.* (doi:10.1038/s41467-019-12161-1)
19. Kim M gu, Brown DK, Brand O. 2020 Nanofabrication for all-soft and high-density electronic devices based on liquid metal. *Nat. Commun.* (doi:10.1038/s41467-020-14814-y)
20. Cheng S *et al.* 2020 Electronic Blood Vessel. *Matter* (doi:10.1016/j.matt.2020.08.029)
21. Kim S, Oh J, Jeong D, Bae J. 2019 Direct Wiring of Eutectic Gallium-Indium to a Metal Electrode for Soft Sensor Systems. *ACS Appl. Mater. Interfaces*  
(doi:10.1021/acsami.9b05363)
22. Martin-Monier L, Gupta T Das, Yan W, Lacour S, Sorin F. 2021 Nanoscale Controlled

- Oxidation of Liquid Metals for Stretchable Electronics and Photonics. *Adv. Funct. Mater.* (doi:10.1002/adfm.202006711)
23. Tavakoli M, Malakooti MH, Paisana H, Ohm Y, Green Marques D, Alhais Lopes P, Piedade AP, de Almeida AT, Majidi C. 2018 EGaIn-Assisted Room-Temperature Sintering of Silver Nanoparticles for Stretchable, Inkjet-Printed, Thin-Film Electronics. *Adv. Mater.* (doi:10.1002/adma.201801852)
  24. Pan C, Markvicka EJ, Malakooti MH, Yan J, Hu L, Matyjaszewski K, Majidi C. 2019 A Liquid-Metal–Elastomer Nanocomposite for Stretchable Dielectric Materials. *Adv. Mater.* (doi:10.1002/adma.201900663)
  25. Cooper CB, Arutselvan K, Liu Y, Armstrong D, Lin Y, Khan MR, Genzer J, Dickey MD. 2017 Stretchable Capacitive Sensors of Torsion, Strain, and Touch Using Double Helix Liquid Metal Fibers. *Adv. Funct. Mater.* (doi:10.1002/adfm.201605630)
  26. Fassler A, Majidi C. 2015 Liquid-Phase Metal Inclusions for a Conductive Polymer Composite. *Adv. Mater.* (doi:10.1002/adma.201405256)
  27. Mohammed MG, Kramer R. 2017 All-Printed Flexible and Stretchable Electronics. *Adv. Mater.* (doi:10.1002/adma.201604965)
  28. Ota H, Chen K, Lin Y, Kiriya D, Shiraki H, Yu Z, Ha T-J, Javey A. 2014 Highly deformable liquid-state heterojunction sensors. *Nat. Commun.* **5**, 5032. (doi:10.1038/ncomms6032)
  29. Reichel KS, Lozada-Smith N, Joshipura ID, Ma J, Shrestha R, Mendis R, Dickey MD, Mittleman DM. 2018 Electrically reconfigurable terahertz signal processing devices using liquid metal components. *Nat. Commun.* (doi:10.1038/s41467-018-06463-z)
  30. Thrasher CJ, Farrell ZJ, Morris NJ, Willey CL, Tabor CE. 2019 Mechanoresponsive Polymerized Liquid Metal Networks. *Adv. Mater.* (doi:10.1002/adma.201903864)
  31. Ladd C, So JH, Muth J, Dickey MD. 2013 3D printing of free standing liquid metal microstructures. *Adv. Mater.* **25**, 5081–5085. (doi:10.1002/adma.201301400)
  32. Parekh DP, Ladd C, Panich L, Moussa K, Dickey MD. 2016 3D printing of liquid metals

- as fugitive inks for fabrication of 3D microfluidic channels. *Lab Chip* (doi:10.1039/c6lc00198j)
33. Farrell ZJ, Tabor C. 2018 Control of Gallium Oxide Growth on Liquid Metal Eutectic Gallium/Indium Nanoparticles via Thiolation. *Langmuir* (doi:10.1021/acs.langmuir.7b03384)
  34. Joshipura ID, Ayers HR, Majidi C, Dickey MD. 2015 Methods to pattern liquid metals. *J. Mater. Chem. C.* (doi:10.1039/c5tc00330j)
  35. Jacob AR, Parekh DP, Dickey MD, Hsiao LC. 2019 Interfacial Rheology of Gallium-Based Liquid Metals. *Langmuir* (doi:10.1021/acs.langmuir.9b01821)
  36. Xu Q, Oudalov N, Guo Q, Jaeger HM, Brown E. 2012 Effect of oxidation on the mechanical properties of liquid gallium and eutectic gallium-indium. *Phys. Fluids* **24**. (doi:10.1063/1.4724313)
  37. Ye Z, Lum GZ, Song S, Rich S, Sitti M. 2016 Gallium Adhesion: Phase Change of Gallium Enables Highly Reversible and Switchable Adhesion (*Adv. Mater.* 25/2016). *Adv. Mater.* **28**, 5087–5087. (doi:10.1002/adma.201670176)
  38. Powell RW. 1949 Some anisotropic properties of gallium. *Nature*. (doi:10.1038/164153b0)
  39. Turnbull D. 1949 The subcooling of liquid metals [4]. *J. Appl. Phys.* (doi:10.1063/1.1698534)
  40. Frank FC. 1952 Supercooling of liquids. *Proc. R. Soc. London. Ser. A. Math. Phys. Sci.* **215**, 43–46. (doi:10.1098/rspa.1952.0194)
  41. Soares BF, Jonsson F, Zheludev NI. 2007 All-optical phase-change memory in a single gallium nanoparticle. *Phys. Rev. Lett.* (doi:10.1103/PhysRevLett.98.153905)
  42. Gong XG, Chiarotti GL, Parrinello M, Tosatti E. 1993 Coexistence of monatomic and diatomic molecular fluid character in liquid gallium. *EPL* **21**, 469–475. (doi:10.1209/0295-5075/21/4/015)
  43. Demmel F. 2018 Dynamics on next-neighbour distances in liquid and undercooled

- gallium. *J. Phys. Condens. Matter* (doi:10.1088/1361-648X/aab72)
44. Mokshin A V., Khusnutdinoff RM, Galimzyanov BN, Brazhkin V V. 2020 Extended short-range order determines the overall structure of liquid gallium. *Phys. Chem. Chem. Phys.* **22**, 4122–4129. (doi:10.1039/c9cp05219d)
  45. Xiong LH *et al.* 2017 Temperature-dependent structure evolution in liquid gallium. *Acta Mater.* **128**, 304. (doi:10.1016/j.actamat.2017.02.038)
  46. Hoyer W, Thomas E, Wobst M. 1980 Structure investigation on liquid gallium. *Krist. und Tech.* (doi:10.1002/crat.19800150806)
  47. Yunusa M, Lahlou A, Sitti M. 2020 Thermal Effects on the Crystallization Kinetics, and Interfacial Adhesion of Single-Crystal Phase-Change Gallium. *Adv. Mater.* (doi:10.1002/adma.201907453)
  48. Hardy SC. 1985 The surface tension of liquid gallium. *J. Cryst. Growth* (doi:10.1016/0022-0248(85)90367-7)
  49. Abbaschian GJ. 1975 Surface tension of liquid gallium. *J. Less-Common Met.* (doi:10.1016/0022-5088(75)90077-6)
  50. Young T. 1805 An essay on cohesion of fluids. *Philos. Trans. te R. Soc. London*
  51. Israelachvili JN. 2011 Intermolecular and Surface Forces Preface to Second Edition. *Intermol. Surf. Forces, 3rd Ed.*
  52. Xu Q, Oudalov N, Guo Q, Jaeger HM, Brown E. 2012 Effect of oxidation on the mechanical properties of liquid gallium and eutectic gallium-indium. *Phys. Fluids* (doi:10.1063/1.4724313)
  53. Larsen RJ, Dickey MD, Whitesides GM, Weitz DA. 2009 Viscoelastic properties of oxide-coated liquid metals. *J. Rheol. (N. Y. N. Y.)* **53**, 1305–1326. (doi:10.1122/1.3236517)
  54. Spells KE. 2002 The determination of the viscosity of liquid gallium over an extended nrange of temperature. *Proc. Phys. Soc.* **48**, 299–311. (doi:10.1088/0959-5309/48/2/308)
  55. Eaker CB, Dickey MD. 2016 Liquid metal actuation by electrical control of interfacial

- tension. *Appl. Phys. Rev.* (doi:10.1063/1.4959898)
56. Tang SY, Khoshmanesh K, Sivan V, Petersen P, O'Mullane AP, Abbott D, Mitchell A, Kalantar-Zadeh K. 2014 Liquid metal enabled pump. *Proc. Natl. Acad. Sci. U. S. A.* (doi:10.1073/pnas.1319878111)
  57. Khan MR, Eaker CB, Bowden EF, Dickey MD. 2014 Giant and switchable surface activity of liquid metal via surface oxidation. *Proc Natl Acad Sci U S A* **111**, 14047–14051. (doi:10.1073/pnas.1412227111)
  58. Hu L, Wang L, Ding Y, Zhan S, Liu J. 2016 Manipulation of Liquid Metals on a Graphite Surface. *Adv. Mater.* **28**, 9210–9217. (doi:10.1002/adma.201601639)
  59. Efimenko K, Rackaitis M, Manias E, Vaziri A, Mahadevan L, Genzer J. 2005 Nested self-similar wrinkling patterns in skins. *Nat. Mater.* **4**, 293–297. (doi:10.1038/nmat1342)
  60. Cerda E, Mahadevan L. 2003 Geometry and Physics of Wrinkling. *Phys. Rev. Lett.* **90**, 074302. (doi:10.1103/PhysRevLett.90.074302)
  61. Huang J, Juskiewicz M, De Jeu WH, Cerda E, Emrick T, Menon N, Russell TP. 2007 Capillary wrinkling of floating thin polymer films. *Science (80-. )*. **317**, 650–653. (doi:10.1126/science.1144616)
  62. Stafford CM *et al.* 2004 A buckling-based metrology for measuring the elastic moduli of polymeric thin films. *Nat. Mater.* (doi:10.1038/nmat1175)
  63. Kim DH *et al.* 2011 Epidermal electronics. *Science (80-. )*. (doi:10.1126/science.1206157)
  64. Li Z, Zhai Y, Wang Y, Wendland GM, Yin X, Xiao J. 2017 Harnessing Surface Wrinkling–Cracking Patterns for Tunable Optical Transmittance. *Adv. Opt. Mater.* (doi:10.1002/adom.201700425)
  65. Rhee D, Lee WK, Odom TW. 2017 Crack-Free, Soft Wrinkles Enable Switchable Anisotropic Wetting. *Angew. Chemie - Int. Ed.* (doi:10.1002/anie.201701968)
  66. Chung JY, Nolte AJ, Stafford CM. 2011 Surface wrinkling: A versatile platform for measuring thin-film properties. *Adv. Mater.* (doi:10.1002/adma.201001759)
  67. Harris AK, Wild P, Stopak D. 1980 Silicone rubber substrata: A new wrinkle in the study

- of cell locomotion. *Science* (80-. ). (doi:10.1126/science.6987736)
68. Brochard-Wyart F, Gilles de Gennes P. 2003 How soft skin wrinkles. *Science* (80-. ). (doi:10.1126/science.300.5618.441)
69. Oratis AT, Bush JWM, Stone HA, Bird JC. 2020 A new wrinkle on liquid sheets: Turning the mechanism of viscous bubble collapse upside down. *Science* (80-. ). (doi:10.1126/science.aba0593)
70. Genzer J, Groenewold J. 2006 Soft matter with hard skin: From skin wrinkles to templating and material characterization. *Soft Matter*. (doi:10.1039/b516741h)
71. King H, Schroll RD, Davidovitch B, Menon N. 2012 Elastic sheet on a liquid drop reveals wrinkling and crumpling as distinct symmetry-breaking instabilities. *Proc. Natl. Acad. Sci.* **109**, 9716–9720. (doi:10.1073/pnas.1201201109)
72. Kumar D, Paulsen JD, Russell TP, Menon N. 2018 Wrapping with a splash: High-speed encapsulation with ultrathin sheets. *Science* (80-. ). (doi:10.1126/science.aa01290)
73. Zhang W, Mazzarello R, Wuttig M, Ma E. 2019 Designing crystallization in phase-change materials for universal memory and neuro-inspired computing. *Nat. Rev. Mater.* (doi:10.1038/s41578-018-0076-x)
74. Hwang CS. 2015 Prospective of Semiconductor Memory Devices: from Memory System to Materials. *Adv. Electron. Mater.* **1**. (doi:10.1002/aelm.201400056)
75. Zhang W, Mazzarello R, Wuttig M, Ma E. 2019 Designing crystallization in phase-change materials for universal memory and neuro-inspired computing. *Nat. Rev. Mater.* **4**, 150–168. (doi:10.1038/s41578-018-0076-x)
76. Salinga M *et al.* 2018 Monatomic phase change memory. *Nat. Mater.* **17**, 681–685. (doi:10.1038/s41563-018-0110-9)
77. Soares BF, Jonsson F, Zheludev NI. 2007 All-optical phase-change memory in a single gallium nanoparticle. *Phys. Rev. Lett.* **98**, 1–4. (doi:10.1103/PhysRevLett.98.153905)
78. Turnbull D. 1950 Formation of crystal nuclei in liquid metals. *J. Appl. Phys.* **21**, 1022–1028. (doi:10.1063/1.1699435)

79. Turnbull D. 1950 Formation of crystal nuclei in liquid metals. *J. Appl. Phys.*  
(doi:10.1063/1.1699435)
80. Liu Z, Bando Y, Mitome M, Zhan J. 2004 Unusual freezing and melting of gallium encapsulated in carbon nanotubes. *Phys. Rev. Lett.* (doi:10.1103/PhysRevLett.93.095504)
81. Kenichi T, Kazuaki K, Masao A. 1998 High-pressure bct-fcc phase transition in Ga. *Phys. Rev. B - Condens. Matter Mater. Phys.* (doi:10.1103/PhysRevB.58.2482)
82. Di Cicco A. 1998 Phase transitions in confined gallium droplets. *Phys. Rev. Lett.*  
(doi:10.1103/PhysRevLett.81.2942)
83. He H, Fei GT, Cui P, Zheng K, Liang LM, Li Y, De Zhang L. 2005 Relation between size and phase structure of gallium: Differential scanning calorimeter experiments. *Phys. Rev. B - Condens. Matter Mater. Phys.* (doi:10.1103/PhysRevB.72.073310)
84. Meng Chen X, Tao Fei G, Feng Li X, Zheng K, De Zhang L. 2010 Metastable phases in GalliumIndium eutectic alloy particles and their size dependence. *J. Phys. Chem. Solids*  
(doi:10.1016/j.jpcs.2010.03.049)
85. Li XF, Fei GT, Chen XM, Zhang Y, Zheng K, Liu XL, Zhang L De. 2011 Size-temperature phase diagram of gallium. *EPL* **94**, 16001. (doi:10.1209/0295-5075/94/16001)
86. Konrad H, Weissmüller J, Birringer R, Karmonik C. 1998 Kinetics of gallium films confined at grain boundaries. *Phys. Rev. B - Condens. Matter Mater. Phys.*  
(doi:10.1103/PhysRevB.58.2142)
87. Degtyareva O, McMahon MI, Allan DR, Nelmes RJ. 2004 Structural complexity in gallium under high pressure: Relation to alkali elements. *Phys. Rev. Lett.*  
(doi:10.1103/PhysRevLett.93.205502)
88. Gromnitskaya EL, Yagafarov OF, Stalgorova O V., Brazhkin V V., Lyapin AG. 2007 Pressure-driven ‘molecular metal’ to ‘atomic metal’ transition in crystalline Ga. *Phys. Rev. Lett.* (doi:10.1103/PhysRevLett.98.165503)
89. Lyapin AG, Gromnitskaya EL, Yagafarov OF, Stal’gorova O V., Brazhkin V V. 2008

- Elastic properties of crystalline and liquid gallium at high pressures. *J. Exp. Theor. Phys.* **107**, 818–827. (doi:10.1134/S1063776108110125)
90. Soares BF, MacDonald KF, Zheludev NI. 2007 Resetting single nanoparticle structural phase with nanosecond pulses. *Appl. Phys. Lett.* (doi:10.1063/1.2760174)
  91. Gong XG, Chiarotti GL, Parrinello M, Tosatti E. 1991  $\pm$ -gallium: A metallic molecular crystal. *Phys. Rev. B* (doi:10.1103/PhysRevB.43.14277)
  92. Tonner R, Gaston N. 2014 The dimeric nature of bonding in gallium: From small clusters to the  $\alpha$ -gallium phase. *Phys. Chem. Chem. Phys.* (doi:10.1039/c4cp03643c)
  93. Glazov VM, Chizhevskaya SN, Glagoleva NN, Glazov VM, Chizhevskaya SN, Glagoleva NN. 1969 Methods for Investigating the Physicochemical Properties of Molten Semiconductors. In *Liquid Semiconductors*, (doi:10.1007/978-1-4899-6451-9\_2)
  94. Glazov VM, Chizhevskaya SN, Glagoleva NN. 1969 *Liquid Semiconductors*. (doi:10.1007/978-1-4899-6451-9)
  95. Nield VM, McGreevy RL, Tucker MG. 1998 Changes in the short-range order of gallium on melting and supercooling. *J. Phys. Condens. Matter* (doi:10.1088/0953-8984/10/15/006)
  96. Rapeanu SN, Padureanu I. 1995 The structure anomaly of liquid ga. *Phys. Scr.* (doi:10.1088/0031-8949/1995/T57/003)
  97. Yang J, Tse JS, Itaka T. 2011 First-principles study of liquid gallium at ambient and high pressure. *J. Chem. Phys.* **135**, 044507. (doi:10.1063/1.3615936)
  98. Cajahuaranga S, De Koning M, Antonelli A. 2013 Revisiting dynamics near a liquid-liquid phase transition in Si and Ga: The fragile-to-strong transition. *J. Chem. Phys.* **139**, 224504. (doi:10.1063/1.4843415)
  99. Kurita R, Tanaka H. 2007 Control of the liquid-liquid transition in a molecular liquid by spatial confinement. *Phys. Rev. Lett.* (doi:10.1103/PhysRevLett.98.235701)
  100. Debenedetti PG, Stillinger FH. 2001 Supercooled liquids and the glass transition. *Nature*. (doi:10.1038/35065704)

101. Katayama Y, Mizutani T, Utsumi W, Shimomura O, Yamakata M, Funakoshi KI. 2000 A first-order liquid-liquid phase transition in phosphorus. *Nature* (doi:10.1038/35003143)
102. Henry L, Mezouar M, Garbarino G, Sifré D, Weck G, Datchi F. 2020 Liquid–liquid transition and critical point in sulfur. *Nature* (doi:10.1038/s41586-020-2593-1)
103. Nefedov DY, Podorozhkin DY, Charnaya E V., Uskov A V., Haase J, Kumzerov YA, Fokin A V. 2019 Liquid-liquid transition in supercooled gallium alloys under nanoconfinement. *J. Phys. Condens. Matter* **31**, 255101. (doi:10.1088/1361-648X/ab1111)
104. Tien C, Charnaya E V., Wang W, Kumzerov YA, Michel D. 2006 Possible liquid-liquid transition of gallium confined in opal. *Phys. Rev. B - Condens. Matter Mater. Phys.* **74**, 024116. (doi:10.1103/PhysRevB.74.024116)
105. Li R, Sun G, Xu L. 2016 Anomalous properties and the liquid-liquid phase transition in gallium. *J. Chem. Phys.* **145**, 054506. (doi:10.1063/1.4959891)
106. Lu Z-Y, Wang C-Z, Ho K-M. 2000 Structures and dynamical properties of C\_{n}, Si\_{n}, Ge\_{n}, and Sn\_{n} clusters with n up to 13. *Phys. Rev. B*
107. Couchman PR, Jesser WA. 1977 Thermodynamic theory of size dependence of melting temperature in metals. *Nature* (doi:10.1038/269481a0)
108. Berman RP, Curzon AE. 1974 SIZE DEPENDENCE OF THE MELTING POINT OF SMALL PARTICLES OF INDIUM. *Can. J. Phys.* (doi:10.1139/p74-125)
109. Buffat P, Borel JP. 1976 Size effect on the melting temperature of gold particles. *Phys. Rev. A* (doi:10.1103/PhysRevA.13.2287)
110. Lai SL, Guo JY, Petrova V, Ramanath G, Allen LH. 1996 Size-dependent melting properties of small tin particles: Nanocalorimetric measurements. *Phys. Rev. Lett.* (doi:10.1103/PhysRevLett.77.99)
111. Lereah Y, Deutscher G, Cheyssac P, Kofman R. 1990 A direct observation of low-dimensional effects on melting of small lead particles. *EPL* (doi:10.1209/0295-5075/12/8/007)
112. Schmidt M, Kusche R, Von Issendorff B, Haberland H. 1998 Irregular variations in the

- melting point of size-selected atomic clusters. *Nature* (doi:10.1038/30415)
113. Schmidt M, Kusche R, Kronmüller W, Von Issendorff B, Haberland H. 1997 Experimental determination of the melting point and heat capacity for a free cluster of 139 sodium atoms. *Phys. Rev. Lett.* (doi:10.1103/PhysRevLett.79.99)
  114. Shvartsburg AA, Jarrold MF. 2000 Solid clusters above the bulk melting point. *Phys. Rev. Lett.* (doi:10.1103/PhysRevLett.85.2530)
  115. Shvartsburg AA, Jarrold MF. 1999 Tin clusters adopt prolate geometries. *Phys. Rev. A - At. Mol. Opt. Phys.* (doi:10.1103/PhysRevA.60.1235)
  116. Joshi K, Krishnamurty S, Kanhere DG. 2006 ‘Magic melters’ have geometrical origin. *Phys. Rev. Lett.* (doi:10.1103/PhysRevLett.96.135703)
  117. Breaux GA, Benirschke RC, Sugai T, Kinnear BS, Jarrold MF. 2003 Hot and solid gallium clusters: Too small to melt. *Phys. Rev. Lett.* (doi:10.1103/PhysRevLett.91.215508)
  118. Breaux GA, Hillman DA, Neal CM, Benirschke RC, Jarrold MF. 2004 Gallium cluster ‘magic melters’. *J. Am. Chem. Soc.* (doi:10.1021/ja0477423)
  119. Briggs LJ. 1957 Gallium: Thermal Conductivity; Supercooling; Negative Pressure. *J. Chem. Phys.* **26**, 784–786. (doi:10.1063/1.1743405)
  120. Kano M. 1991 Supercooling and Its Thermal Hysteresis of Pure Metal Liquids. *Netsu Shori(Journal Japan Soc. Heat ...* **18**, 64–70.
  121. Reinitzer F. 1888 Beiträge zur Kenntniss des Cholesterins. *Monatshefte für Chemie* (doi:10.1007/BF01516710)
  122. Goodby JW. 2011 The nanoscale engineering of nematic liquid crystals for displays. *Liq. Cryst.* (doi:10.1080/02678292.2011.614700)
  123. Yunusa M, Amador GJ, Drotlef DM, Sitti M. 2018 Wrinkling Instability and Adhesion of a Highly Bendable Gallium Oxide Nanofilm Encapsulating a Liquid-Gallium Droplet. *Nano Lett.* **18**, 2498–2504. (doi:10.1021/acs.nanolett.8b00164)
  124. Huang J, Juskiewicz M, de Jeu WH, Cerda E, Emrick T, Menon N, Russell TP. 2007

- Capillary Wrinkling of Floating Thin Polymer Films. *Science* (80-. ). **317**, 650–653. (doi:10.1126/science.1144616)
125. Taffetani M, Vella D. 2017 Regimes of wrinkling in pressurized elastic shells. *Philos. Trans. R. Soc. A Math. Phys. Eng. Sci.* **375**, 20160330. (doi:10.1098/rsta.2016.0330)
  126. Ciarletta P, Vella D. 2017 Patterning through instabilities in complex media: theory and applications. *Philos. Trans. R. Soc. A Math. Phys. Eng. Sci.* **375**.
  127. Grason GM, Davidovitch B. 2013 Universal collapse of stress and wrinkle-to-scar transition in spherically confined crystalline sheets. *Proc. Natl. Acad. Sci.* **110**, 12893–12898. (doi:10.1073/pnas.1301695110)
  128. Bella P, Kohn R V. 2017 Wrinkling of a thin circular sheet bonded to a spherical substrate. *Philos. Trans. R. Soc. A Math. Phys. Eng. Sci.* **375**.
  129. Holmes DP, Crosby AJ. 2010 Draping Films: A Wrinkle to Fold Transition. *Phys. Rev. Lett.* **105**, 38303.
  130. Lacour SP, Wagner S, Huang Z, Suo Z. 2003 Stretchable gold conductors on elastomeric substrates. *Appl. Phys. Lett.* **82**, 2404–2406. (doi:10.1063/1.1565683)
  131. Jiang H, Khang D-Y, Song J, Sun Y, Huang Y, Rogers JA. 2007 Finite deformation mechanics in buckled thin films on compliant supports. *Proc. Natl. Acad. Sci.* **104**, 15607–15612. (doi:10.1073/pnas.0702927104)
  132. Glassmaker NJ, Jagota A, Hui C-Y, Noderer WL, Chaudhury MK. 2007 Biologically inspired crack trapping for enhanced adhesion. *Proc. Natl. Acad. Sci.* **104**, 10786–10791. (doi:10.1073/pnas.0703762104)
  133. Sharon E, Aharoni H. 2016 Chiral bundles: Frustrated shapes. *Nat. Mater.* **15**, 707–709. (doi:10.1038/nmat4678)
  134. Meng G, Paulose J, Nelson DR, Manoharan VN. 2014 Elastic Instability of a Crystal Growing on a Curved Surface. *Science* (80-. ). **343**, 634–637. (doi:10.1126/science.1244827)
  135. Regan MJ, Tostmann H, Pershan PS, Magnussen OM, DiMasi E, Ocko BM, Deutsch M.

- 1997 X-ray study of the oxidation of liquid-gallium surfaces. *Phys. Rev. B* **55**, 10786–10790. (doi:10.1103/PhysRevB.55.10786)
136. Khan MR, Trlica C, So J, Valeri M, Dickey MD. 2014 Influence of water on the interfacial behavior of gallium liquid metal alloys. *ACS Appl. Mater. Interfaces* **6**, 22467–73. (doi:10.1021/am506496u)
137. Owuor PS, Hiremath S, Chipara AC, Vajtai R, Lou J, Mahapatra DR, Tiwary CS, Ajayan PM. 2017 Nature Inspired Strategy to Enhance Mechanical Properties via Liquid Reinforcement. *Adv. Mater. Interfaces* , 1700240. (doi:10.1002/admi.201700240)
138. Bartlett MD, Kazem N, Powell-Palm MJ, Huang X, Sun W, Malen JA, Majidi C. 2017 High thermal conductivity in soft elastomers with elongated liquid metal inclusions. *Proc. Natl. Acad. Sci.* **114**, 2143–2148. (doi:10.1073/pnas.1616377114)
139. Lu Y, Hu Q, Lin Y, Pacardo DB, Wang C, Sun W, Ligler FS, Dickey MD, Gu Z. 2015 Transformable liquid-metal nanomedicine. *Nat. Commun.* **6**, 10066. (doi:10.1038/ncomms10066)
140. Chabala JM. 1992 Oxide-growth kinetics and fractal-like patterning across liquid gallium surfaces. *Phys. Rev. B* **46**, 11346–11357. (doi:10.1103/PhysRevB.46.11346)
141. Carey BJ *et al.* 2017 Wafer-scale two-dimensional semiconductors from printed oxide skin of liquid metals. *Nat. Commun.* **8**, 14482. (doi:10.1038/ncomms14482)
142. Hirsch A, Michaud HO, Gerratt AP, de Mulatier S, Lacour SP. 2016 Biphasic Metal Films: Intrinsically Stretchable Biphasic (Solid-Liquid) Thin Metal Films (*Adv. Mater.* 22/2016). *Adv. Mater.* **28**, 4506–4506. (doi:10.1002/adma.201670153)
143. Park YL, Chen BR, Wood RJ. 2012 Design and fabrication of soft artificial skin using embedded microchannels and liquid conductors. *IEEE Sens. J.* **12**, 2711–2718. (doi:10.1109/JSEN.2012.2200790)
144. Zavabeti A *et al.* 2017 A liquid metal reaction environment for the room-temperature synthesis of atomically thin metal oxides. *Science (80-. ).* **358**, 332–335. (doi:10.1126/science.aao4249)

145. Kramer RK, Boley JW, Stone HA, Weaver JC, Wood RJ. 2014 Effect of microtextured surface topography on the wetting behavior of eutectic gallium-indium alloys. *Langmuir* **30**, 533–539. (doi:10.1021/la404356r)
146. Doudrick K, Liu S, Mutunga EM, Klein KL, Damle V, Varanasi KK, Rykaczewski K. 2014 Different shades of oxide: From nanoscale wetting mechanisms to contact printing of gallium-based liquid metals. *Langmuir* **30**, 6867–6877. (doi:10.1021/la5012023)
147. Flory AL, Brass DA, Shull KR. 2007 Deformation and adhesive contact of elastomeric membranes. *J. Polym. Sci. Part B Polym. Phys.* **45**, 3361–3374. (doi:10.1002/polb.21322)
148. Long R, Shull KR, Hui CY. 2010 Large deformation adhesive contact mechanics of circular membranes with a flat rigid substrate. *J. Mech. Phys. Solids* **58**, 1225–1242. (doi:10.1016/j.jmps.2010.06.007)
149. Laprade EJ, Long R, Pham JT, Lawrence J, Emrick T, Crosby AJ, Hui CY, Shull KR. 2013 Large deformation and adhesive contact studies of axisymmetric membranes. *Langmuir* **29**, 1407–1419. (doi:10.1021/la303810d)
150. Seung HS, Nelson DR. 1988 Defects in flexible membranes with crystalline order. *Phys. Rev. A* **38**, 1005–1018. (doi:10.1103/PhysRevA.38.1005)
151. Autumn K *et al.* 2002 Evidence for van der Waals adhesion in gecko setae. *Proc. Natl. Acad. Sci. U. S. A.* (doi:10.1073/pnas.192252799)
152. Autumn K, Liang YA, Hsieh ST, Zesch W, Chan WP, Kenny TW, Fearing R, Full RJ. 2000 Adhesive force of a single gecko foot-hair. *Nature* (doi:10.1038/35015073)
153. Butt HJ, Roisman I V., Brinkmann M, Papadopoulos P, Vollmer D, Semprebon C. 2014 Characterization of super liquid-repellent surfaces. *Curr. Opin. Colloid Interface Sci.* **19**, 343–354. (doi:10.1016/j.cocis.2014.04.009)
154. Dickey MD, Chiechi RC, Larsen RJ, Weiss EA, Weitz DA, Whitesides GM. 2008 Eutectic gallium-indium (EGaIn): A liquid metal alloy for the formation of stable structures in microchannels at room temperature. *Adv. Funct. Mater.* **18**, 1097–1104. (doi:10.1002/adfm.200701216)

155. Hure J, Roman B, Bico J. 2011 Wrapping an Adhesive Sphere with an Elastic Sheet. *Phys. Rev. Lett.* **106**. (doi:10.1103/PhysRevLett.106.174301)
156. <http://www.tamura-ss.co.jp/en/products/gao/index.html> (accessed: 2017-06-16). In press. No Title.
157. Chung JY, Chaudhury MK. 2005 Roles of discontinuities in bio-inspired adhesive pads. *J. R. Soc. Interface* **2**, 55–61. (doi:10.1098/rsif.2004.0020)
158. Danov KD, Stanimirova RD, Kralchevsky PA, Marinova KG, Stoyanov SD, Blijdenstein TBJ, Cox AR, Pelan EG. 2016 Adhesion of bubbles and drops to solid surfaces, and anisotropic surface tensions studied by capillary meniscus dynamometry. *Adv. Colloid Interface Sci.* **233**, 223–239. (doi:10.1016/j.cis.2015.06.003)
159. Koenig SP, Boddeti NG, Dunn ML, Bunch JS. 2011 Ultrastrong adhesion of graphene membranes. *Nat. Nanotechnol.* **6**, 543–546. (doi:10.1038/nnano.2011.123)
160. Bunch JS, Dunn ML. 2012 Adhesion mechanics of graphene membranes. *Solid State Commun.* **152**, 1359–1364. (doi:10.1016/j.ssc.2012.04.029)
161. Li B, Cao Y-P, Feng X-Q, Gao H. 2012 Mechanics of morphological instabilities and surface wrinkling in soft materials: a review. *Soft Matter* **8**, 5728. (doi:10.1039/c2sm00011c)
162. Orava J, Greer AL, Gholipour B, Hewak DW, Smith CE. 2012 Characterization of supercooled liquid Ge<sub>2</sub>Sb<sub>2</sub>Te<sub>5</sub> and its crystallization by ultrafast-heating calorimetry. *Nat. Mater.* **11**, 279–283. (doi:10.1038/nmat3275)
163. Loke D, Lee TH, Wang WJ, Shi LP, Zhao R, Yeo YC, Chong TC, Elliott SR. 2012 Breaking the speed limits of phase-change memory. *Science* (80-. ). (doi:10.1126/science.1221561)
164. Sleutel M, Van Driessche AES. 2014 Role of clusters in nonclassical nucleation and growth of protein crystals. *Proc. Natl. Acad. Sci.* **111**, E546–E553. (doi:10.1073/pnas.1309320111)
165. Smeets PJM, Finney AR, Habraken WJEM, Nudelman F, Friedrich H, Laven J, De Yoreo

- JJ, Rodger PM, Sommerdijk NAJM. 2017 A classical view on nonclassical nucleation. *Proc. Natl. Acad. Sci.* **114**, E7882–E7890. (doi:10.1073/pnas.1700342114)
166. Olafson KN, Nguyen TQ, Rimer JD, Vekilov PG. 2017 Antimalarials inhibit hemozoin crystallization by unique drug–surface site interactions. *Proc. Natl. Acad. Sci.* **114**, 7531–7536. (doi:10.1073/pnas.1700125114)
167. Li T, Donadio D, Ghiringhelli LM, Galli G. 2009 Surface-induced crystallization in supercooled tetrahedral liquids. *Nat. Mater.* **8**, 726–730. (doi:10.1038/nmat2508)
168. Bi Y, Cao B, Li T. 2017 Enhanced heterogeneous ice nucleation by special surface geometry. *Nat. Commun.* **8**, 1–7. (doi:10.1038/ncomms15372)
169. Holden MA, Whale TF, Tarn MD, O’Sullivan D, Walshaw RD, Murray BJ, Meldrum FC, Christenson HK. 2019 High-speed imaging of ice nucleation in water proves the existence of active sites. *Sci. Adv.* **5**, eaav4316. (doi:10.1126/sciadv.aav4316)
170. Kiselev A, Bachmann F, Pedevilla P, Cox SJ, Michaelides A, Gerthsen D, Leisner T. 2016 Active sites in heterogeneous ice nucleation—the example of K-rich feldspars. *Science* (80-. ). (doi:10.1126/science.aai8034)
171. Simpson RE, Fons P, Kolobov A V., Fukaya T, Krbal M, Yagi T, Tominaga J. 2011 Interfacial phase-change memory. *Nat. Nanotechnol.* **6**, 501–505. (doi:10.1038/nnano.2011.96)
172. Salinga M, Carria E, Kaldenbach A, Bornhöfft M, Benke J, Mayer J, Wuttig M. 2013 Measurement of crystal growth velocity in a melt-quenched phase-change material. *Nat. Commun.* **4**. (doi:10.1038/ncomms3371)
173. Li X Bin, Chen NK, Wang XP, Sun HB. 2018 Phase-Change Superlattice Materials toward Low Power Consumption and High Density Data Storage: Microscopic Picture, Working Principles, and Optimization. *Adv. Funct. Mater.* **28**, 1–21. (doi:10.1002/adfm.201803380)
174. Sebastian A, Le Gallo M, Krebs D. 2014 Crystal growth within a phase change memory cell. *Nat. Commun.* **5**, 4314. (doi:10.1038/ncomms5314)

175. Simpson RE, Krbal M, Fons P, Kolobov A V., Tominaga J, Uruga T, Tanida H. 2010 Toward the ultimate limit of phase change in Ge<sub>2</sub>Sb<sub>2</sub>Te<sub>5</sub>. *Nano Lett.* **10**, 414–419. (doi:10.1021/nl902777z)
176. Orava J, Greer AL, Gholipour B, Hewak DW, Smith CE. 2012 Ultra-fast calorimetry study of Ge<sub>2</sub>Sb<sub>2</sub>Te<sub>5</sub> crystallization between dielectric layers. *Appl. Phys. Lett.* **101**. (doi:10.1063/1.4748881)
177. Greer AL. 2006 Supercool order. *Nat. Mater.* (doi:10.1038/nmat1557)
178. Oh SH, Kauffmann Y, Scheu C, Kaplan WD, Rühle M. 2005 Ordered liquid aluminum at the interface with sapphire. *Science (80- )*. (doi:10.1126/science.1118611)
179. Panciera F, Tersoff J, Gamalski AD, Reuter MC, Zakharov D, Stach EA, Hofmann S, Ross FM. 2019 Surface Crystallization of Liquid Au–Si and Its Impact on Catalysis. *Adv. Mater.* (doi:10.1002/adma.201806544)
180. Arai S, Tanaka H. 2017 Surface-assisted single-crystal formation of charged colloids. *Nat. Phys.* **13**, 503–509. (doi:10.1038/nphys4034)
181. Shpyrko OG, Streitl R, Balagurusamy VSK, Grigoriev AY, Deutsch M, Ocko BM, Meron M, Lin B, Pershan PS. 2006 Surface crystallization in a liquid AuSi alloy. *Science (80- )*. (doi:10.1126/science.1128314)
182. Feng X *et al.* 2019 Single crystal texture by directed molecular self-assembly along dual axes. *Nat. Mater.* (doi:10.1038/s41563-019-0389-1)
183. Hulsman WJ, Peters JF, Zwanenburg MJ, De Vries SA, Derry TE, Abernathy D, Van der Veen JF. 1997 Layering of a liquid metal in contact with a hard wall. *Nature* (doi:10.1038/37069)
184. Briggs LJ. 1957 Gallium: Thermal conductivity; supercooling; negative pressure. *J. Chem. Phys.* **26**, 784–786. (doi:10.1063/1.1743405)
185. Campanini D, Diao Z, Rydh A. 2018 Raising the superconducting T<sub>c</sub> of gallium: In situ characterization of the transformation of  $\alpha$ -Ga into  $\beta$ -Ga. *Phys. Rev. B* **97**, 2–6. (doi:10.1103/PhysRevB.97.184517)

186. Cooper CB, Joshipura ID, Parekh DP, Norkett J, Mailen R, Miller VM, Genzer J, Dickey MD. 2019 Toughening stretchable fibers via serial fracturing of a metallic core. *Sci. Adv.* (doi:10.1126/sciadv.aat4600)
187. Brito D, Elbert D, Olson P. 2002 Experimental crystallization of gallium: Ultrasonic measurements of elastic anisotropy and implications for the inner core. *Phys. Earth Planet. Inter.* **129**, 325–346. (doi:10.1016/S0031-9201(01)00298-9)
188. Miyamura A, Susa M. 2002 Relative measurements of thermal conductivity of liquid gallium by the transient hot-wire method. *High Temp. - High Press.* (doi:10.1068/htjr085)
189. Fukuyama H, Yoshimura T, Yasuda H, Ohta H. 2006 Thermal conductivity measurements of liquid mercury and gallium by a transient hot-wire method in a static magnetic field. *Int. J. Thermophys.* (doi:10.1007/s10765-006-0089-3)
190. Van Der Walt S, Schönberger JL, Nunez-Iglesias J, Boulogne F, Warner JD, Yager N, Gouillart E, Yu T. 2014 Scikit-image: Image processing in python. *PeerJ* (doi:10.7717/peerj.453)
191. Vincent L, Vincent L, Soille P. 1991 Watersheds in Digital Spaces: An Efficient Algorithm Based on Immersion Simulations. *IEEE Trans. Pattern Anal. Mach. Intell.* (doi:10.1109/34.87344)
192. Málek J. 1995 The applicability of Johnson-Mehl-Avrami model in the thermal analysis of the crystallization kinetics of glasses. *Thermochim. Acta.* (doi:10.1016/0040-6031(95)02466-2)
193. De Ruiter J, Soto D, Varanasi KK. 2018 Self-peeling of impacting droplets. *Nat. Phys.* **14**, 35–39. (doi:10.1038/NPHYS4252)
194. Kovalev AE, Varenberg M, Gorb SN. 2012 Wet versus dry adhesion of biomimetic mushroom-shaped microstructures. *Soft Matter* (doi:10.1039/c2sm25431j)
195. Regan MJ, Kawamoto EH, Lee S, Pershan PS, Maskil N, Deutsch M, Magnussen OM, Ocko BM, Berman LE. 1995 Surface layering in liquid gallium: An x-ray reflectivity study. *Phys. Rev. Lett.* (doi:10.1103/PhysRevLett.75.2498)

196. Walko D, Robinson I, Grütter C, Bilgram J. 1998 Surface Structure of a-Ga (010). *Phys. Rev. Lett.*
197. Losurdo M, Suvorova A, Rubanov S, Hingerl K, Brown AS. 2016 Thermally stable coexistence of liquid and solid phases in gallium nanoparticles. *Nat. Mater.* **15**, 995–1002. (doi:10.1038/nmat4705)
198. Yunusa M, Adaka A, Aghakhani A, Shahsavan H, Guo Y, Alapan Y, Jáklí A, Sitti M. 2021 Liquid Crystal Structure of Supercooled Liquid Gallium and Eutectic Gallium–Indium. *Adv. Mater.* **33**. (doi:10.1002/adma.202104807)
199. Fischer D, Andriyevsky B, Schön JC. 2019 Systematics of the allotrope formation in elemental gallium films. *Mater. Res. Express* (doi:10.1088/2053-1591/ab42f6)
200. Holland-Moritz D, Schenk T, Simonet V, Bellissent R. 2006 Short-range order in undercooled and stable melts forming quasicrystals and approximants and its influence on nucleation. In *Philosophical Magazine*, pp. 255–262. (doi:10.1080/14786430500253992)
201. Tsay SF, Wang S. 1994 Anomalies in the liquid structure of Ga metal. *Phys. Rev. B* **50**, 108. (doi:10.1103/PhysRevB.50.108)
202. Tsai KH, Wu TM, Tsay SF. 2010 Revisiting anomalous structures in liquid Ga. *J. Chem. Phys.* **132**, 034502. (doi:10.1063/1.3294565)
203. Chen LY, Tang PH, Wu TM. 2016 Analysis of local bond-orientational order for liquid gallium at ambient pressure: Two types of cluster structures. *J. Chem. Phys.* **145**, 024506. (doi:10.1063/1.4955305)
204. Jara DAC, Fontana Michelon M, Antonelli A, De Koning M. 2009 Theoretical evidence for a first-order liquid-liquid phase transition in gallium. *J. Chem. Phys.* (doi:10.1063/1.3154424)
205. Anderson TJ, Ansara I. 1991 The Ga-In (Gallium-Indium) System. *J. Phase Equilibria* **12**, 64–72. (doi:10.1007/BF02663677)
206. Denny JP, Hamilton JH, Lewis JR. 1952 Constitution of the System Gallium-Indium. *JOM* **4**, 39–42. (doi:10.1007/bf03397646)

207. Dierking I. 2003 *Textures of Liquid Crystals*. (doi:10.1002/3527602054)
208. Pratibha R, Madhusudana N V., Sadashiva BK. 2000 An orientational transition of bent-core molecules in an anisotropic matrix. *Science* (80- ). (doi:10.1126/science.288.5474.2184)
209. Jákli A, Lavrentovich OD, Selinger J V. 2018 Physics of liquid crystals of bent-shaped molecules. *Rev. Mod. Phys.* **90**, 045004. (doi:10.1103/RevModPhys.90.045004)
210. Regan M, Tostmann H, Pershan P, Magnussen O, DiMasi E, Ocko B. 1997 X-ray study of the oxidation of liquid-gallium surfaces. *Phys. Rev. B - Condens. Matter Mater. Phys.* (doi:10.1103/PhysRevB.55.10786)
211. Stepanov SI, Nikolaev VI, Bougrov VE, Romanov AE. 2016 Gallium oxide: Properties and applications - A review. *Rev. Adv. Mater. Sci.* , 63–86.
212. 2004 *Soft Matter Physics: An Introduction*. (doi:10.1007/b97416)
213. Rosenblatt CS, Pindak R, Clark NA, Meyer RB. 1977 PARABOLIC FOCAL CONIC: A NEW SMECTIC A DEFECT. *J Phys* (doi:10.1051/jphys:019770038090110500)
214. Chen D *et al.* 2012 Structure of the B4 liquid crystal phase near a glass surface. *ChemPhysChem* (doi:10.1002/cphc.201100589)
215. Yoon DK, Yi Y, Shen Y, Korblova ED, Walba DM, Smalyukh II, Clark NA. 2011 Orientation of a helical nanofilament (B4) liquid-crystal phase: Topographic control of confinement, shear flow, and temperature gradients. *Adv. Mater.* (doi:10.1002/adma.201004482)
216. Jákli A, Saupe A. 1997 Uniform bookshelf alignment of chiral smectic C films with guided backflow. *J. Appl. Phys.* (doi:10.1063/1.366120)
217. Steenbergen KG, Gaston N. 2016 A Two-Dimensional Liquid Structure Explains the Elevated Melting Temperatures of Gallium Nanoclusters. *Nano Lett.* **16**, 21–26. (doi:10.1021/acs.nanolett.5b02158)
218. Núñez S, López JM, Aguado A. 2012 Neutral and charged gallium clusters: Structures, physical properties and implications for the melting features. *Nanoscale*

(doi:10.1039/c2nr31222k)

219. Aguilar Gutierrez OF, Rey AD. 2014 Structure characterisation method for ideal and non-ideal twisted plywoods. *Soft Matter* (doi:10.1039/c4sm01803f)
220. Bouligand Y. 1972 Twisted fibrous arrangements in biological materials and cholesteric mesophases. *Tissue Cell* (doi:10.1016/S0040-8166(72)80042-9)
221. Bouligand Y. 1977 CHOLESTERIC ORDER IN BIPOLYMERS. In *American Chemical Society, Polymer Preprints, Division of Polymer Chemistry*, (doi:10.1021/bk-1978-0074.ch015)
222. Livolant F, Bouligand Y. 1989 Freeze-Fractures in Cholesteric Mesophases of Polymers. *Mol. Cryst. Liq. Cryst. Inc. Nonlinear Opt.* (doi:10.1080/00268948908037140)
223. In press. Codes for ‘Thermal Effects on the Crystallization Kinetics, and Interfacial Adhesion of Single-Crystal Phase-Change Gallium’. See <https://github.com/Alienor134/crystallization>.

# Appendix A

## Nanofilm Wrinkling Model

We used a previously reported method [71] for solving the Lamé problem for a thin sheet under axisymmetric loading. The details are given in the Supplementary Information of ref [71], but are presented here for convenience. This method solves the Föppl-von Kármán equations for the simple geometry shown in Figure A.1a.

In equilibrium, the stress on an infinitesimal element is zero for the two directions (radial  $r$  and azimuthal  $\theta$ ) in the plane of the sheet so that:

$$\nabla \cdot \boldsymbol{\sigma} = 0 \quad (\text{A.1})$$

where  $\boldsymbol{\sigma}$  is the in-plane stress tensor and  $\nabla$  is the gradient operator for the radial  $r$  and azimuthal  $\theta$  directions. In the normal  $z$  direction, the internal bending stress balances the applied force  $F_{pre}$  such that:

$$\frac{Et^3}{12(1-\nu^2)} \text{Tr}(\boldsymbol{\kappa}) + \boldsymbol{\sigma} \cdot \boldsymbol{\kappa} = F_{pre} \quad (\text{A.2})$$

where  $E$  is the Young's modulus,  $t$  is the thickness,  $\nu$  is the Poisson's ratio,  $\boldsymbol{\kappa}$  is the curvature tensor, and  $\text{Tr}(\boldsymbol{\kappa})$  is the mean curvature. These are the Föppl-von Kármán equations.

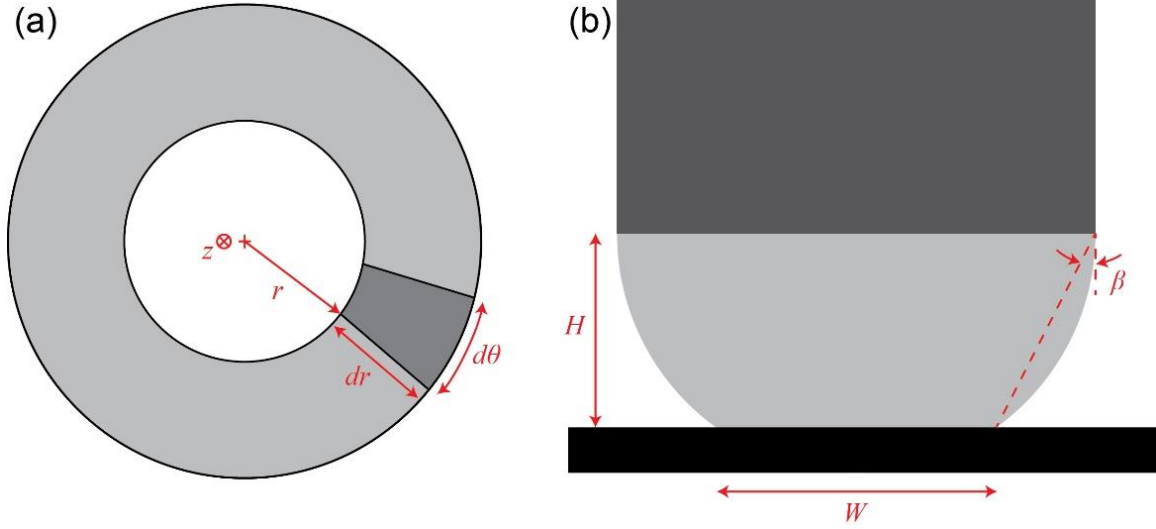


**Figure A.1.** Gallium droplet geometry. (a) In-plane geometry for the Lamé problem. (b) Geometry for the gallium droplet (light gray) pinned to post (top rectangle) and forced into contact with glass substrate (bottom rectangle).

Following a polar coordinate system centered on the thin sheet, the in-plane displacement is  $\mathbf{u}(r, \theta) = u_r(r, \theta)\hat{\mathbf{r}} + u_\theta(r, \theta)\hat{\boldsymbol{\theta}}$  and the normal displacement is  $\zeta(r, \theta)$ . The strain is then given by:

$$\epsilon_{rr} = \partial_r u_r + \frac{1}{2}(\partial_r \zeta)^2 \quad (\text{A.3})$$

$$\epsilon_{\theta\theta} = \frac{1}{r}\partial_\theta u_\theta + \frac{1}{r}u_r + \frac{1}{2r^2}(\partial_\theta \zeta)^2 \quad (\text{A.4})$$

$$\epsilon_{r\theta} = \epsilon_{\theta r} = \frac{1}{2}\left(\frac{1}{r}\partial_\theta u_r + \partial_r u_\theta + \frac{1}{r}\partial_r \zeta \partial_\theta \zeta\right) \quad (\text{A.5})$$

For our sheet, we assumed the relationship between stress and strain was linear, following the Hooke's law; therefore, the stresses are expressed as:

$$\sigma_{rr} = \frac{Et}{1-\nu^2}(\epsilon_{rr} + \nu\epsilon_{\theta\theta}) \quad (\text{A.6})$$

$$\sigma_{\theta\theta} = \frac{Et}{1-\nu^2}(\epsilon_{\theta\theta} + \nu\epsilon_{rr}) \quad (\text{A.7})$$

$$\sigma_{r\theta} = \frac{Et}{1-\nu^2}\epsilon_{r\theta} \quad (\text{A.8})$$

Substituting into the Föppl-von Kármán equations, we obtained the following respective expressions for the force balance in  $\hat{r}$ ,  $\hat{\theta}$ , and normal  $z$  directions:

$$\partial_r \sigma_{rr} + \frac{1}{r} (\partial_\theta \sigma_{r\theta} + \sigma_{rr} - \sigma_{\theta\theta}) = 0 \quad (\text{A.9})$$

$$\partial_r \sigma_{r\theta} + \frac{1}{r} (\partial_\theta \sigma_{\theta\theta} + 2\sigma_{r\theta}) = 0 \quad (\text{A.10})$$

$$\frac{Et^3}{12(1-\nu^2)} \Delta^2 \zeta - \sigma_{rr} \partial_r^2 \zeta - \frac{2}{r} \sigma_{r\theta} \left( \partial_r - \frac{1}{r} \right) \partial_\theta \zeta - \frac{1}{r^2} \sigma_{\theta\theta} (\partial_\theta^2 \zeta + r \partial_r \zeta) = F_{pre} \quad (\text{A.11})$$

where the Laplacian  $\Delta = \partial_r^2 + \frac{1}{r} \partial_r + \frac{1}{r^2} \partial_\theta^2$ .

Since our investigation is concerned with an axisymmetric thin sheet, the azimuthal displacement  $u_\theta$  and all derivatives with respect to the azimuthal  $\theta$  direction vanished. The radial  $r$  and normal  $z$  force balances simplify to:

$$\left( \partial_r + \frac{1}{r} \right) \sigma_{rr} = \frac{1}{r} \sigma_{\theta\theta} \quad (\text{A.12})$$

$$\frac{Et^3}{12(1-\nu^2)} \Delta^2 \zeta_0 - \sigma_{rr} \zeta_0'' - \frac{1}{r} \sigma_{\theta\theta} \zeta_0' = P \quad (\text{A.13})$$

respectively, where  $\zeta_0(r)$  is the axisymmetric normal displacement,  $P = (4F_{pre})/(\pi W^2)$  is the pressure exerted normal to the thin sheet, and primes denote derivatives with respect to the radial  $r$  dimension.

Simplifying the strain tensor results in:

$$u_{rr} = u_r' + \frac{1}{2} \zeta_0'^2 \quad (\text{A.14})$$

$$u_{\theta\theta} = \frac{1}{r} u_r \quad (\text{A.15})$$

Using the stress-strain relations, we can combine the strain tensor into:

$$\left( \partial_r + \frac{1}{r} \right) \sigma_{\theta\theta} = \frac{1}{r} \sigma_{rr} - \frac{Et}{2r} \zeta_0'^2 \quad (\text{A.16})$$

By combining the two expressions for the force balances in the radial  $r$  and normal  $z$  directions, we can eliminate  $\sigma_{\theta\theta}$ , and integrate once with the boundary condition  $\zeta_0'(0) = 0$  to get the following expression for the slope in terms of the radial stress:

$$\zeta'_0(r) = -\frac{Pr}{2\sigma_{rr}(r)} \quad (\text{A.17})$$

We can then reduce our system of three equations to a set of two coupled first-order ODEs for  $\sigma_{rr}$  and  $\sigma_{\theta\theta}$ , so that:

$$\partial_r \sigma_{rr} = \frac{1}{r} (-\sigma_{rr} + \sigma_{\theta\theta}) \quad (\text{A.18})$$

$$\partial_r \sigma_{\theta\theta} = \frac{1}{r} (\sigma_{rr} - \sigma_{\theta\theta}) - \frac{EtP^2r}{8} \frac{1}{\sigma_{rr}^2} \quad (\text{A.19})$$

We can define the following dimensionless variables  $\tilde{r} = r/W$  and  $\tilde{\sigma} = \sigma/(PH \cos \beta)$ , where  $W$  is the width of the contact of the gallium drop on the substrate,  $H$  is the height between the substrate and the post where the gallium droplet is attached.  $\beta$  is the angle between the points of contact between the gallium drop and the post and substrate, and  $P$  is the applied pressure at the contact interface as depicted in Figure A.1b. The length scale  $W$  is the natural length scale since it represents the width of the region of the thin, elastic sheet of interest.

The scale for force per unit length  $PH \cos \beta$  represents the force pulling on the edge of the elastic sheet, and is an adaptation of the force scale from ref [71] to the case of a gallium drop forced into contact with a flat substrate.

With these dimensionless variables, we can non-dimensionalize our governing ODEs as such:

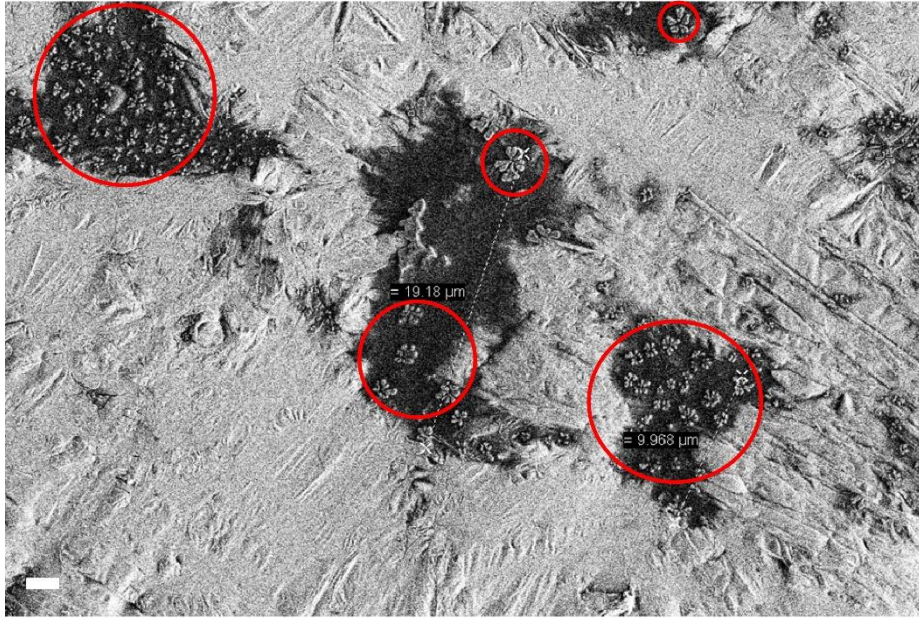
$$\partial_{\tilde{r}} \tilde{\sigma}_{rr} = \frac{1}{\tilde{r}} (-\tilde{\sigma}_{rr} + \tilde{\sigma}_{\theta\theta}) \quad (\text{A.20})$$

$$\partial_{\tilde{r}} \tilde{\sigma}_{\theta\theta} = \frac{1}{\tilde{r}} (\tilde{\sigma}_{rr} - \tilde{\sigma}_{\theta\theta}) - \frac{Et(PW)^2}{8(PH \cos \beta)^3} \tilde{r} \frac{1}{\tilde{\sigma}_{rr}^2} \quad (\text{A.21})$$

To solve for the width  $L$  where radial wrinkles will begin to form, we followed the method for solving the governing ODEs in two zones, an inner disk where  $r < L$  and the hoop stress is tensile  $\sigma_{\theta\theta} > 0$ , and an outer annulus  $L < r < W$  where the hoop stress is zero  $\sigma_{\theta\theta} = 0$ . Continuing to follow the methodology from King *et al.* [71], we used matching between the two zones and minimization of the dominant elastic energy to solve for  $L$ . The details of the analysis are provided in the Supplementary Information of King *et al* [71]. The resulting solution is:

$$\frac{L}{W} = \left(\frac{\alpha}{\alpha^*}\right)^{-1/5} \quad (\text{A.22})$$

(a)



(b)

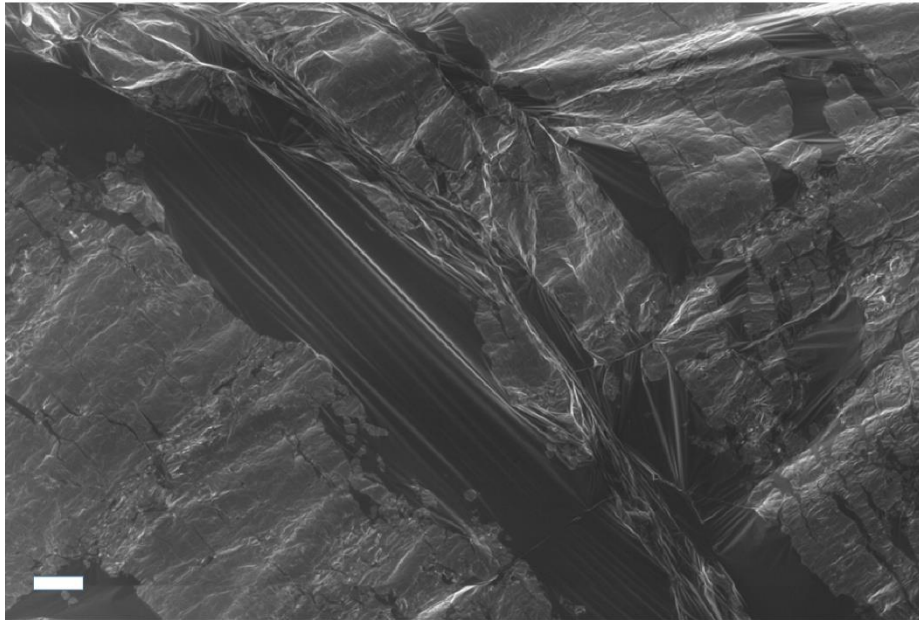


**Figure A.2:** SEM images of the Ga droplet surface. (a) Fractal structures of  $\text{Ga}_2\text{O}_3$  grown on a liquid Ga surface. The surface is exposed to ambient atmosphere before transferring into the SEM chamber after rupturing the native oxide skin and liquid metal was revealed (scale bar:  $2 \mu\text{m}$ ). Red

circles show the fractal structure as reported before in the literature [140]. (b) A ruptured Ga droplet surface depicting discontinuity and reconstruction of its oxide layer after deformation of the native oxide skin. The fresh oxide layer was formed again within the crack region promptly (scale bar: 10  $\mu\text{m}$ ).

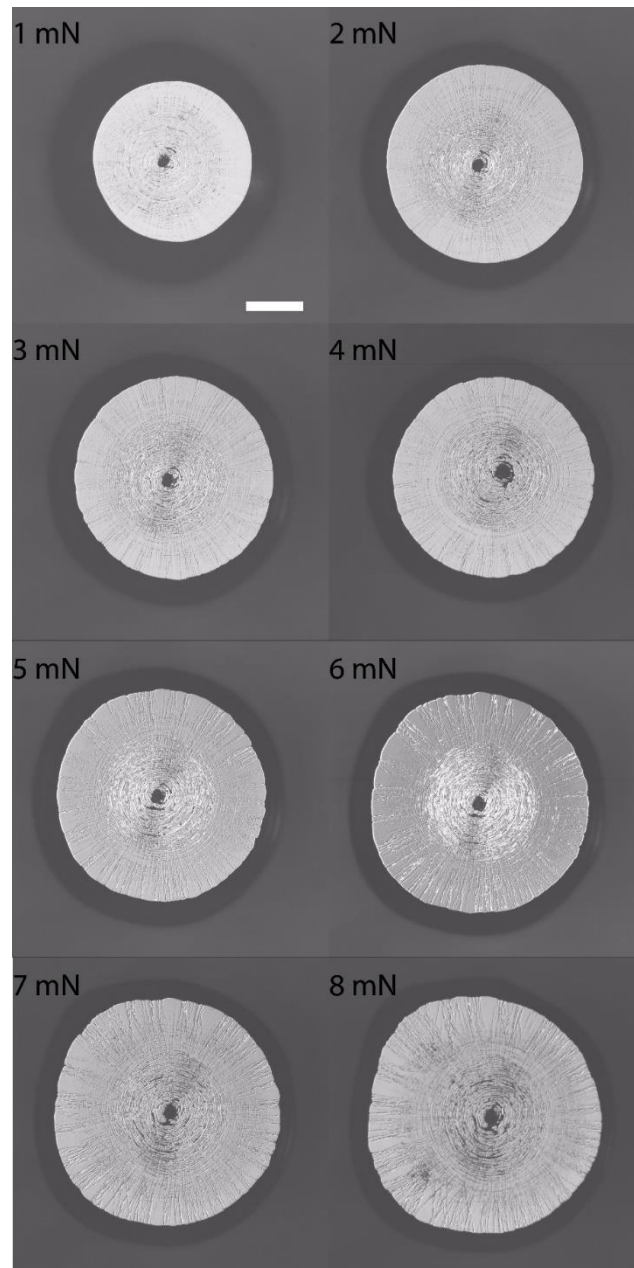


**Figure A.3:** Contact interface images at different preloads on a glass substrate. Inverted microscope images of the wrinkled interfaces of the  $\text{Ga}_2\text{O}_3$  skin and glass upon application of different preloads from 1 to 8 mN. (Scale bar: 0.4 mm).

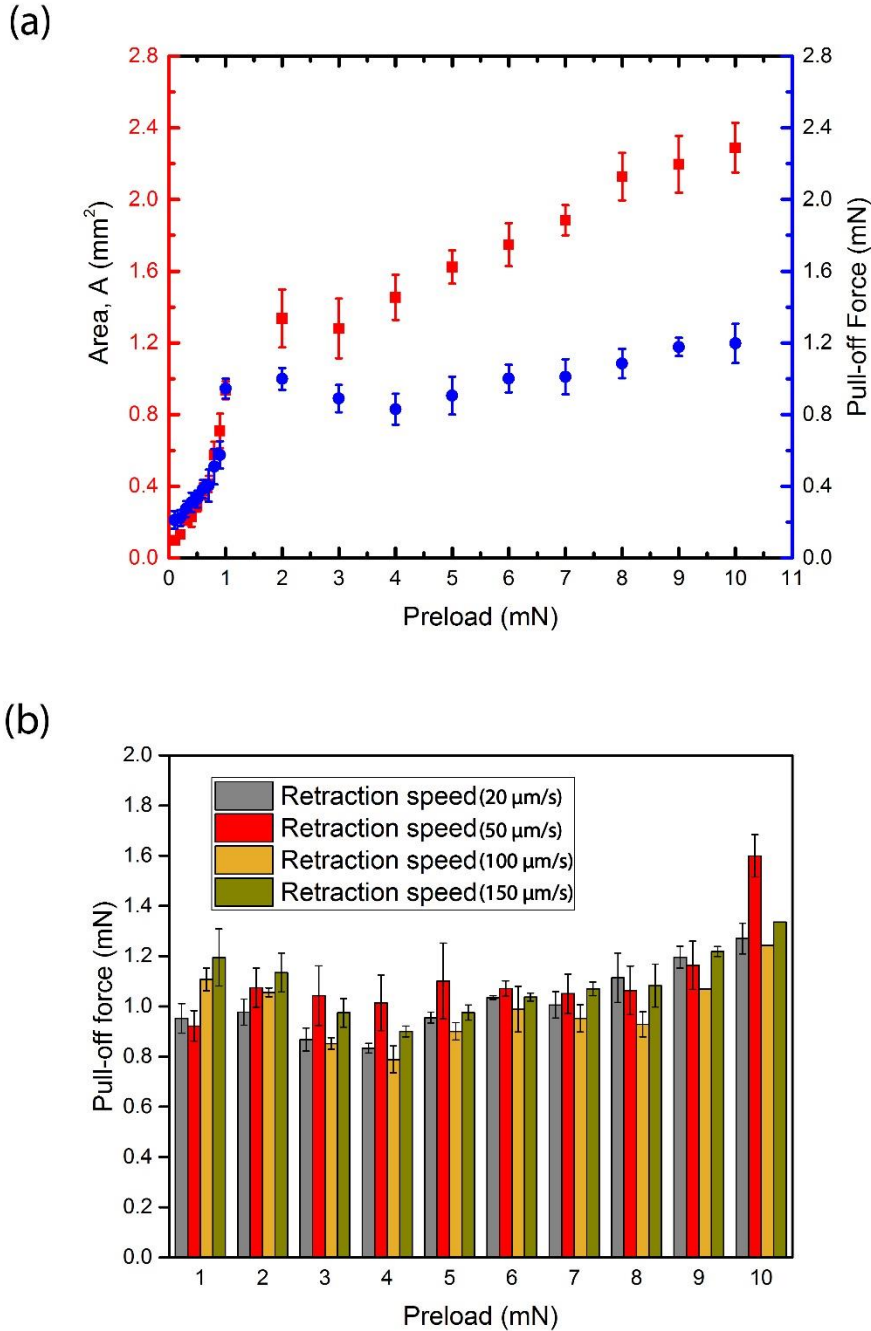


**Figure A.4:** Characterization of contact area, pull-off force and retraction speed. (a) The effective contact area and pull-off force initially increased with preload. At higher preloads the pull-off force is saturated while the contact area continue to increase. The slight increase in the force is attributed to the formation of new oxide as the droplet is further squeezed and ruptured. A commercially available software (ImageJ) was used to analyze the contact area corresponding to maximum pull-off force. (b) Rate-independent adhesion of liquid-Ga is characterized by varying the retraction speed during each set of experiment. Four different speeds (20, 50, 100, and 150  $\mu\text{m/s}$ ), starting from low to high, were characterized.

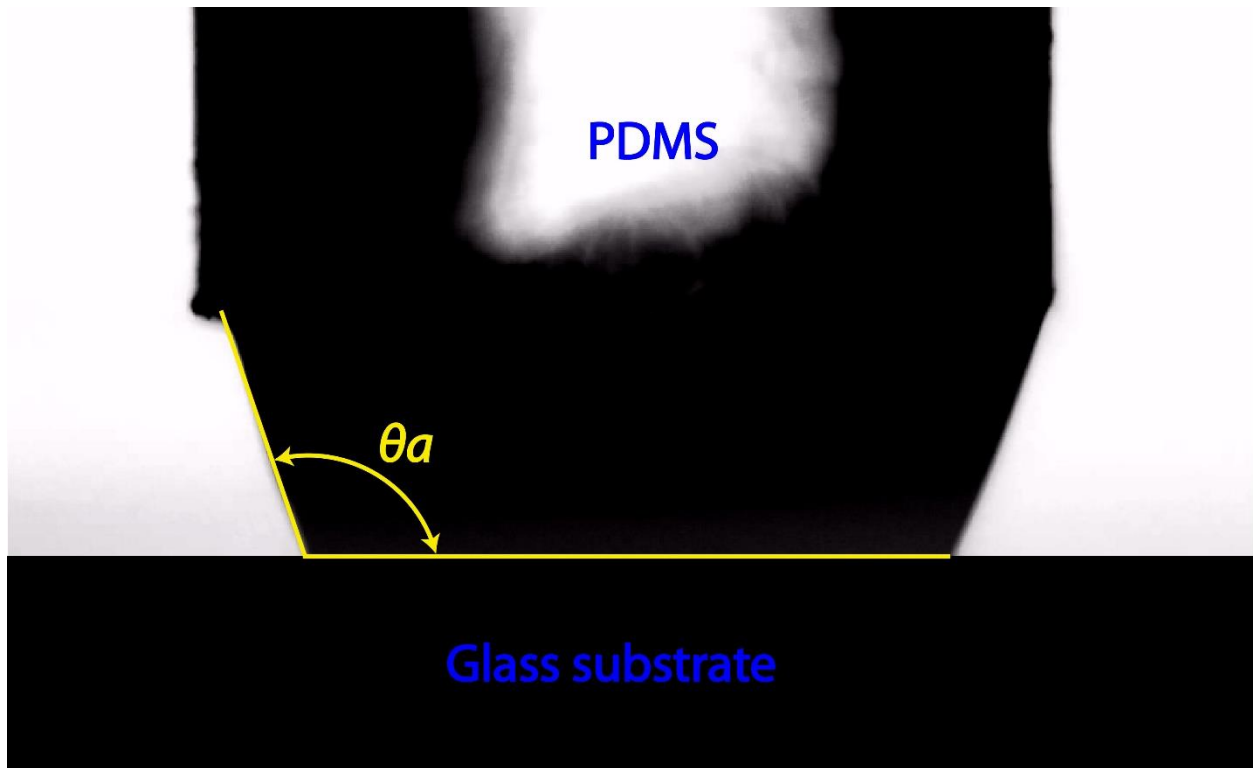


**Figure A.5:** Side-view optical microscope image snapshot of the Ga droplet during retraction from the glass substrate. Apparent contact angle of the Ga droplet on glass,  $\theta_a$ , at maximum pull-off force was measured. Note that the average value of the angle was used for the calculation of the interfacial adhesion energy.

## Appendix B

**Table B.1:** Summary of thermal properties of all substrates used in the experiments.

Substrate	$K$ $\text{Wm}^{-1}\text{K}^{-1}$	$\rho$ $(\text{g}/\text{cm}^3)$	$c_p$ $\text{JKg}^{-1}\text{K}^{-1}$	$e_s$ $\text{Ws}^{1/2}\text{m}^{-2}\text{K}^{-1}$	$\alpha_{diff}$ $(\text{m}^2\text{s}^{-1})$	$L$ $(\text{mm})$	$\tau_d$ $(\text{s})$
Glass	0.937	2.44	880	$1.42 \cdot 10^3$	$4.36 \cdot 10^{-7}$	1	2.3
Zinc selenide	18	5.27	339	$5.67 \cdot 10^3$	$1.01 \cdot 10^{-5}$	5	2.48
Sapphire	27	3.89	763	$9.06 \cdot 10^3$	$8.89 \cdot 10^{-6}$	5	2.81
Silicon	163	2.33	703	$1.63 \cdot 10^4$	$9.95 \cdot 10^{-5}$	5	0.25
Copper	285	8.96	385	$3.64 \cdot 10^4$	$1.12 \cdot 10^{-4}$	6.4	0.36

**Table B.2:** Summary of thermal properties of the liquid Ga.

	$K$ $\text{Wm}^{-1}\text{K}^{-1}$	$\rho$ $(\text{g}/\text{cm}^3)$	$c_p$ $\text{JKg}^{-1}\text{K}^{-1}$	$e_s$ $\text{Ws}^{1/2}\text{m}^{-2}\text{K}^{-1}$	$\alpha_{diff}$ $(\text{m}^2\text{s}^{-1})$	$L$ $(\text{mm})$	$\tau_d$ $(\text{s})$
Gallium liquid	28.2	6.09	409	$8.38 \cdot 10^3$	$1.16 \cdot 10^{-5}$	0.3	0.008

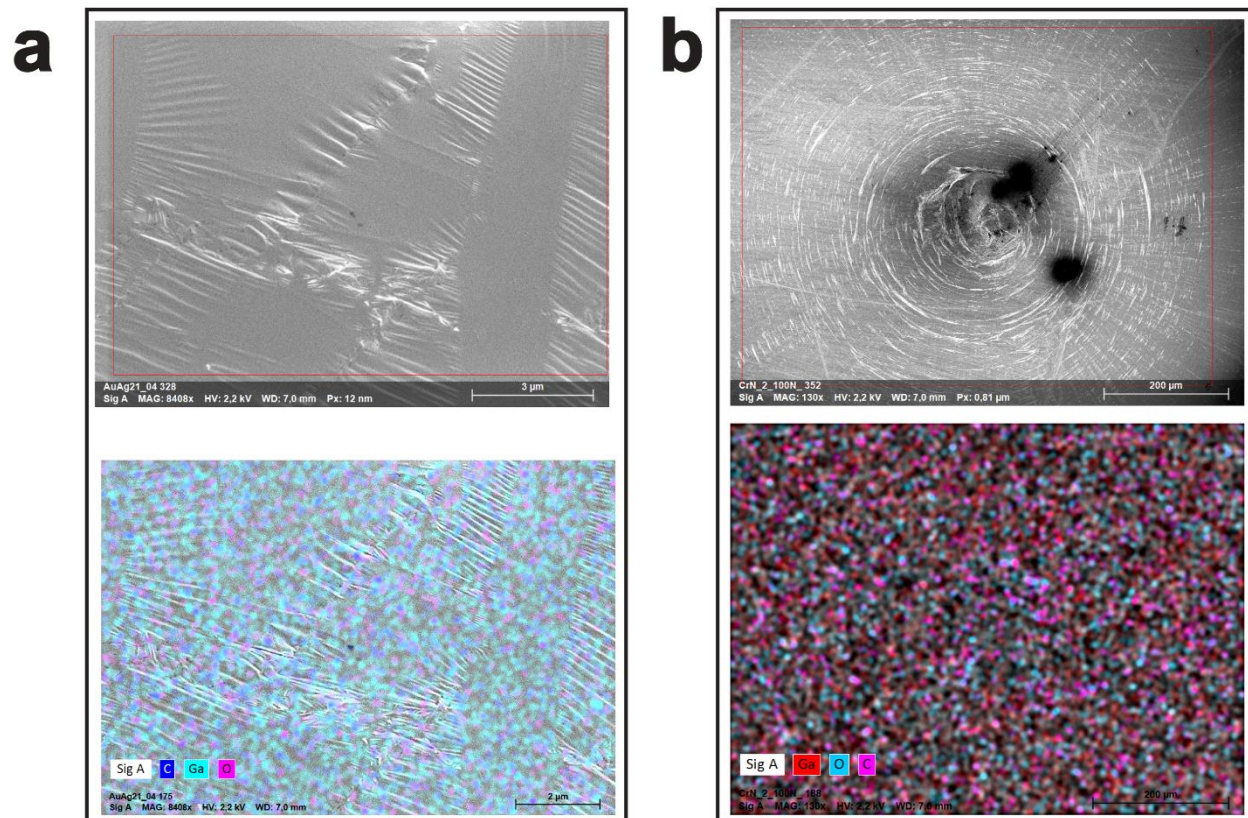


**Figure B.1:** Energy dispersive x-ray (EDX) spectroscopy analysis. On the seeding crystal and detached droplet from glass surface after crystallization, EDX spectroscopy analysis was conducted to verify the elemental composition of Ga.

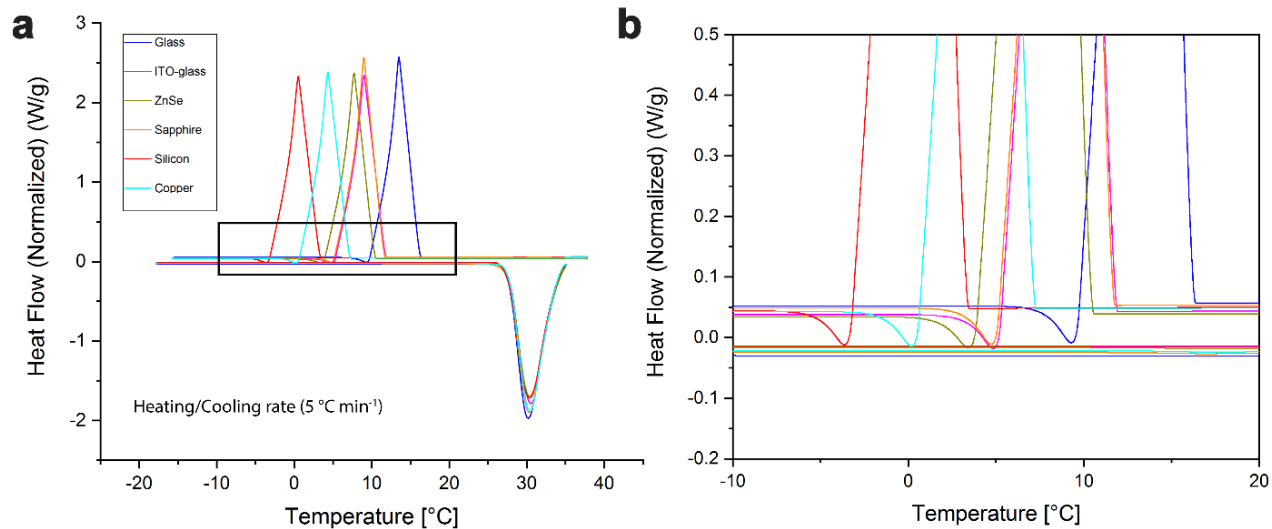


**Figure B.2:** Differential scanning calorimetry (DSC) measurement of heating and cooling curves of Ga droplets crystallized on different substrates. (a) The pristine crystallized droplets on different substrates with first heating cycle from the solid state, and then cooling down to -20 °C at the same rate. (b) Enlarged black box in (a) showing the crystallization curves of the melted droplets after heating the droplets from the solids to liquid state at a rate of 5 °C min<sup>-1</sup>.

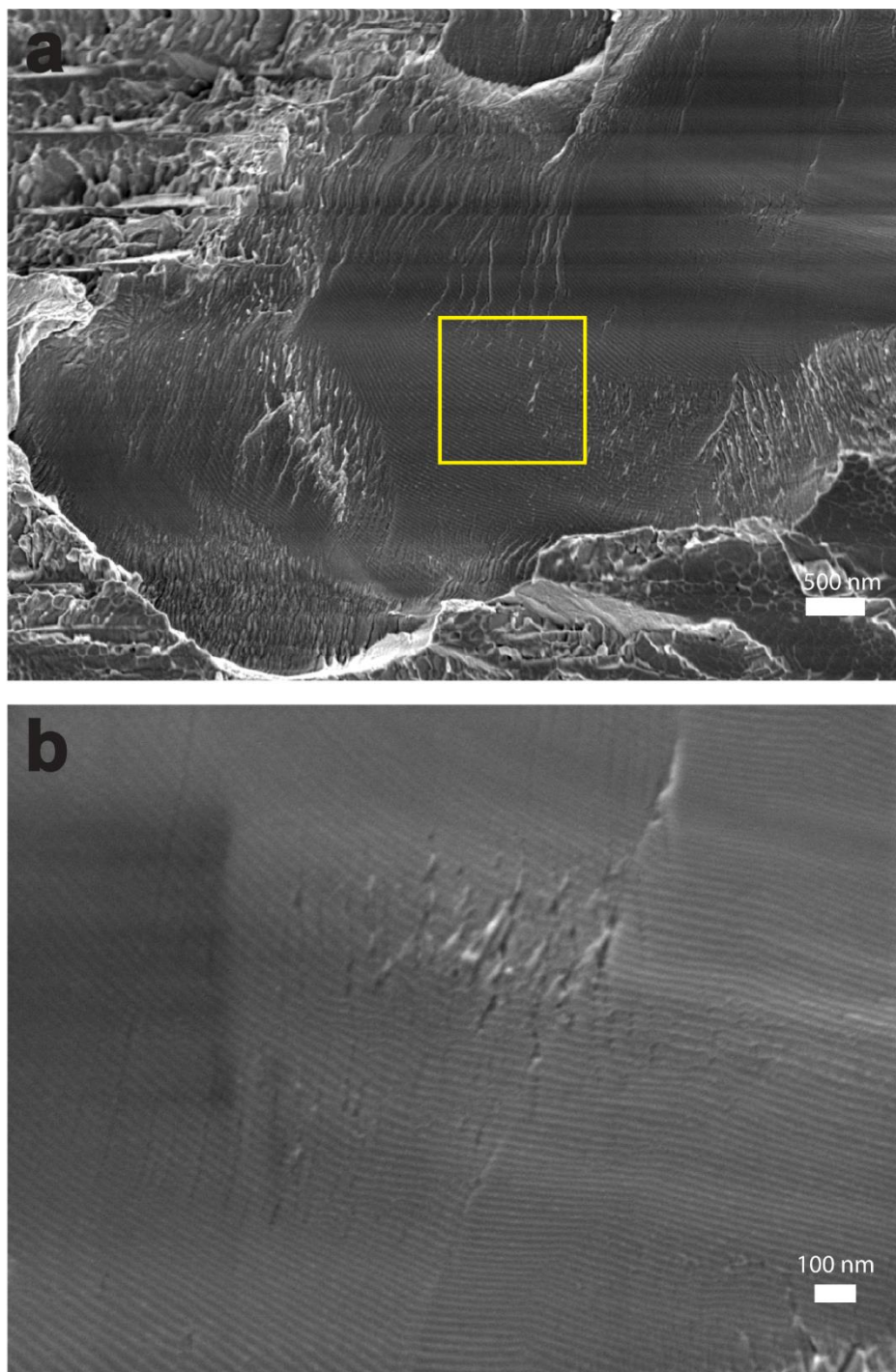


**Figure B.3:** Structural investigation of crystallized Ga. A droplet of Ga was quenched on a silicon substrate and was freeze-fractured for SEM observation. a) Brittle-like fracture surface of the droplet showing both glassy and ordered layers of Ga. b) The magnified image of the yellow square region with structural order.

## Appendix C

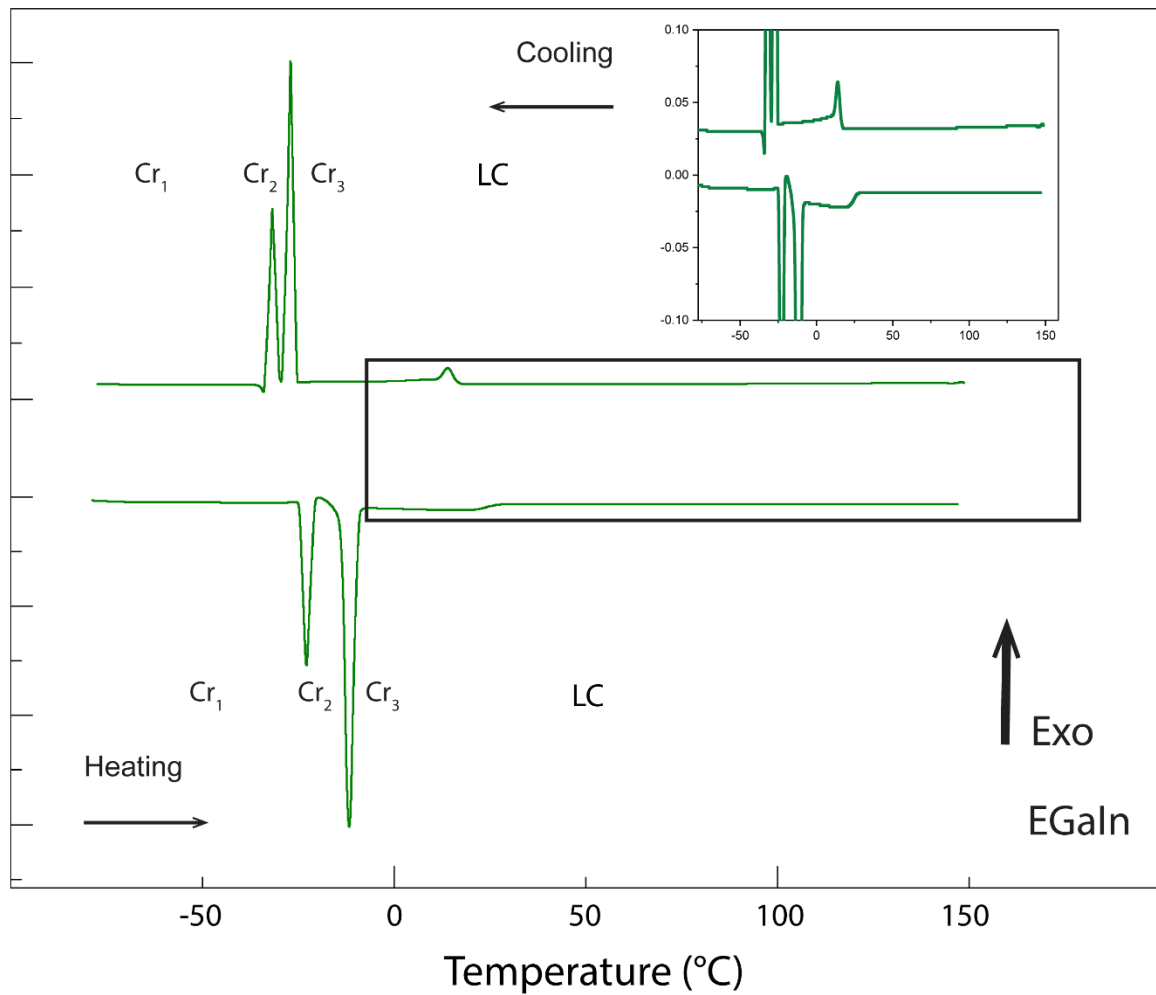


**Figure C.1:** Polymorph structure of Ga. Differential scanning calorimetry of EGaIn measured through heating/cooling at 2°C/min. The possible polymorphs of different Ga phases when alloyed can be resolved as labelled Cr<sub>1</sub>, Cr<sub>2</sub>, and Cr<sub>3</sub>.

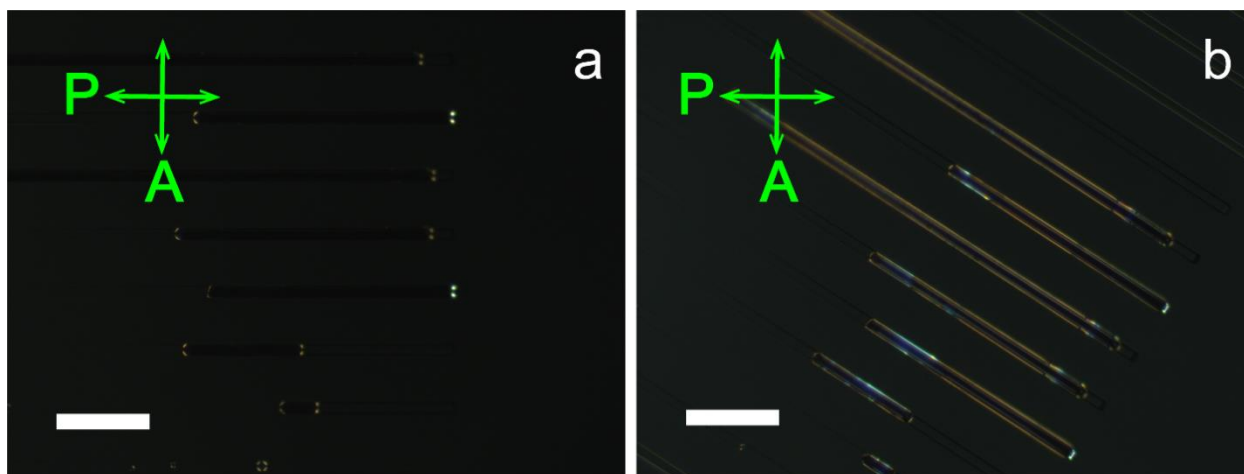


**Figure C.2:** Planar orientation of EGaIn in microchannel confinement. Images taken 10 minutes after filling the channel at 22 °C. The direction of the microchannel is aligned with one of the polarizers (a) and rotated 45° with respect to the polarizers in transmission light microscope (b). The microchannel dimensions are 15  $\mu\text{m}$  width and 17  $\mu\text{m}$  depth with 55  $\mu\text{m}$  spacing. Scale bars: 100  $\mu\text{m}$ .

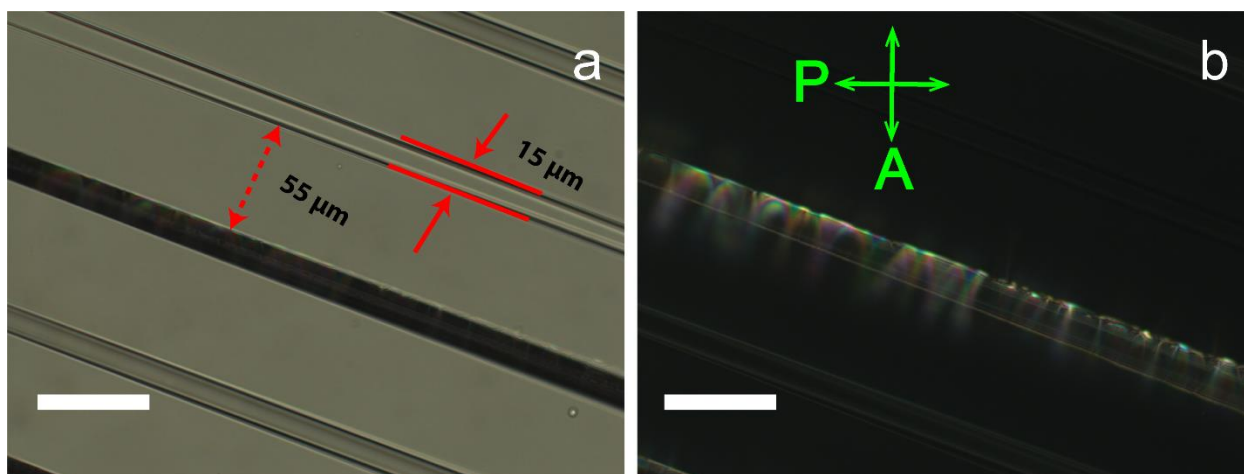


**Figure C.3:** Microchannel confinement after 2 hours at 22 °C. Without analyzer (a) and crossed-polarized transmission image (b). Scale bars are 50  $\mu\text{m}$ . Note the appearance parabolic focal conic domains resembling to smectic phase. The height of the microchannel is 17  $\mu\text{m}$ . The empty microchannel are always dark.

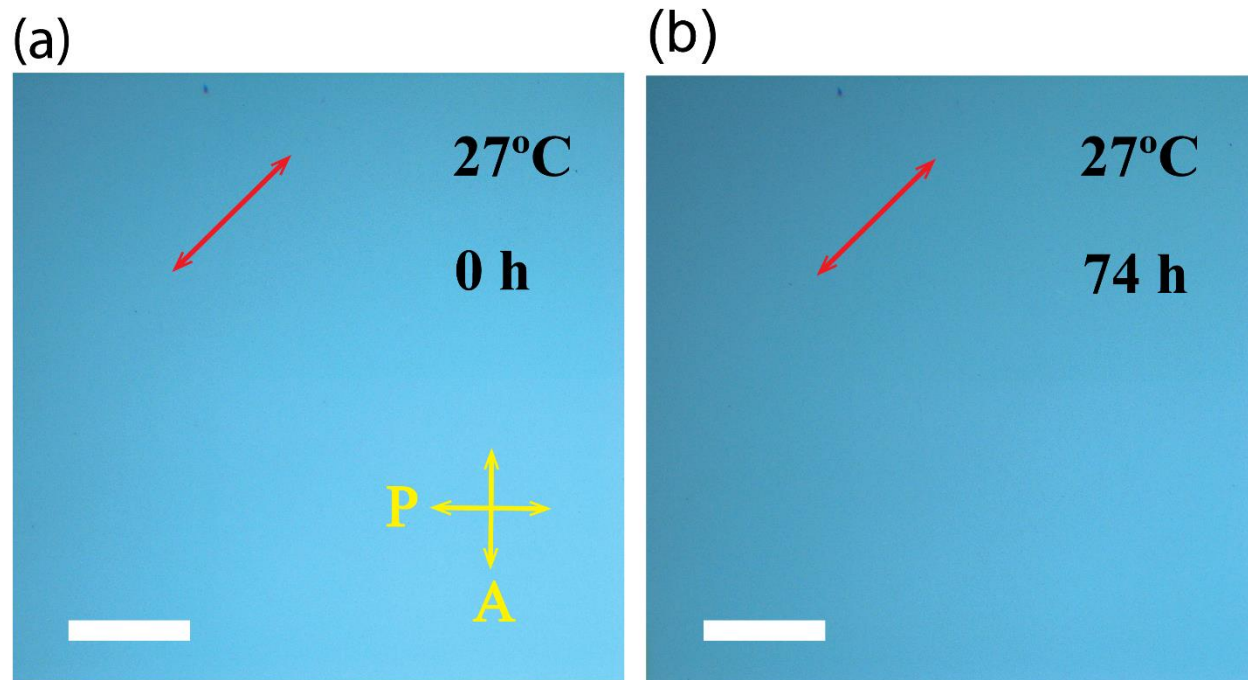


**Figure C.4:** Room temperature stability observation of liquid Ga planar cell over 74 hours (7 h). The red double-head arrow indicates the rubbing direction under R-POM.